2022

Novel Modes of Synchronization and Extreme Events in Coupled Chemical Oscillators

David Allen Mersing
West Virginia University, damersing@mix.wvu.edu

Recommended Citation

Mersing, David Allen, "Novel Modes of Synchronization and Extreme Events in Coupled Chemical Oscillators" (2022). *Graduate Theses, Dissertations, and Problem Reports*. 11324.
https://researchrepository.wvu.edu/etd/11324

Novel Modes of Synchronization and Extreme Events in Coupled Chemical Oscillators

David Mersing

Dissertation submitted
to the Eberly College of Arts and Sciences at
West Virginia University

in partial fullfillment of the requirments for the degree of
Doctor of Philosophy in
Chemistry

Kenneth Showalter, Ph.D., Chair
Mark Tinsley, Ph.D.
Terry Gullion, Ph.D.
Justin Legleiter, Ph.D.
Kevin Daly, Ph.D.

C. Eugene Bennett Department of Chemistry
Morgantown, West Virginia

March 2022

Keywords: BZ reaction, Synchronization, Phase Response Curves, Extreme Events, Star Networks

Abstract

Novel Modes of Synchronization and Extreme Events in Coupled Chemical Oscillators

David Mersing

We experimentally and computationally investigate dynamical behaviors in coupled chemical oscillators. These networks of chemical oscillators are created using catalytic $\mathrm{Ru(bpy)_3^{2+}}$ loaded cation exchange beads submerged in catalyst-free Belousov-Zhabotinsky (BZ) solutions. Various network structures are created by utilizing the photosensitive nature of the $\mathrm{Ru(bpy)_3^{2+}}$ catalyst. The response of the oscillators due to light stimuli can be characterized by constructing a phase response curve (PRC). The PRC quantifies the excitatory and inhibitory responses of BZ oscillators due to applied light perturbations as a function of the oscillators' phase. Different initial concentrations of reactants in the BZ reaction solutions can vary the degree in the excitatory and inhibitory regions of the PRC.

We explore synchronization in star networks in both excitatory and inhibitory systems. We describe experiments, simulations, and analytical theory that provides a detailed characterization of novel modes of synchronization in chemical oscillator networks. Synchronization of peripheral oscillators coupled through a hub oscillator is exhibited at coupling strengths leading to novel synchronization of the hub with the peripheral oscillators. The heterogenous peripheral oscillators have different phase velocities that give rise to divergence; however, the perturbation from the hub acts to realign the phases by delaying the faster oscillators more than the slower oscillators. A theoretical analysis provides insights into the mechanism of the synchronization.

Computational studies into extreme events are investigated using a modified four-variable Oregonator model, which describes the BZ system. Extreme events are ubiquitous throughout biological, natural, social, and financial systems. Examples of such events are epileptic seizures, earthquakes, riots, and stock market crashes. These events are considered rare excursions from the normal dynamics of a system, which are considered aperiodic in occurrence. The consequences that these events have on the system makes the development of models and experimental methods to study these events important. We will describe the appearance of extreme events in the Oregonator system using instantaneous and time-delayed coupling. We will also discuss a proposed mechanism for the sudden appearance of extreme events in both instantaneous and time-delayed coupling.

Dedication

This effort is dedicated to the memories of my maternal grandmother Nanny Helmick and my adopted grandmother Hazel Hauger. As well as my wife Lori and my children Drake, Patrick, and Kaley. Your support and belief in me never wavered as you defended me from those who sought to tear me down. I will always be grateful to all of you and you will always have a place in my heart.

Acknowledgments

I would first like to acknowledge my research adviser Dr. Ken Showalter. I want to thank you for all the support and guidance through this journey. Your patience, expertise, and valuable insights made the successful conclusion of this program possible. You continued to go above and beyond your duties to teach, support and guide me and I will always be grateful to you. Next, I would like to thank Dr. Mark Tinsley for his efforts and guidance throughout my studies. You made me a better researcher by teaching me not to just accept results, but to question them to make sure they are correct. I would also like to thank the rest of my committee Dr. Terry Gullion, Dr. Justin Legleiter, and Dr. Kevin Daly for taking the time to be part of my graduate program. Thank you for reviewing my written works and attending my required talks. I appreciate all the feedback and insights you provided.

I would also like to thank my fellow students and friends that took this journey with me Dr. Syed Jazli Syed Jamaluddin, Shannyn Tyler, Md Boshir Ahmed, and Kudakwashe Shumba. I appreciate all the help from all of you during my time at WVU. I want to also give a special thank you to Benjamas Poonbonjaroenchai from Kasetsart Univeristy. The help and support during your time at WVU made the novel synchronization project possible. You pushed me to work at a high level and filled in for me during my surgery and kept me on track. To Brianna Hickman who proofread several chapters for me and provided valuable feedback. Your time and efforts are appreciated. I also want to acknowledge the ladies the WVU TRiO program Cindy Drum, Vivian Cespedes, and Vanessa Stevens. I would not have try to make this journey without your support and encouragement.

Finally, I want to thank my family for allowing me the time to attend college and earn my degrees. Thank you for your patience and support during tough times. I could not hope for better people to make this journey with me. Thank you all for everything you have done.

Contents

List of Figures

List of Figures

List of Tables

List of Tables

Chapter 1

Introduction

1.1 Nonlinear Dynamics

Nonlinear systems are ubiquitous in nature and are of great importance to the understanding of our world. These systems are so common that Stanislaw Ulam said "Using a term like nonlinear science is like referring to the bulk of zoology as the study of non-elephant animals [1]." Unfortunately, nonlinear systems are often difficult or impossible to solve analytically. To simplify these systems they are often described and modeled as linear systems. Linearity is built on the idea that a system with well-defined conditions will follow a predictable course, and any slight change in those conditions will cause minimal change in the dynamics of the system [2–5]. Linear thinking also allows us to assume that multiple changes to a system are simply the superposition of all the effects taken individually. This assertion of unlimited predictability and the simplification of complex dynamical systems ultimately makes linear models highly attractive. While linear models are useful for understanding small changes and making predictions, they can be incomplete and misleading. The complete nonlinear systems can show complex and unpredictable behavior, which can be dramatically different from their linear counterparts. This complexity can be observed in many forms such as an abrupt transition in behavior due to bifurcations [6–8], multistability [9–11], and pattern formations [12–14]. Some nonlinear systems can also become completely unpredictable, which has become known as deterministic chaos [6, 15, 16]. The widespread availability of computers to study nonlinear models allows us to investigate phenomena when linear models break down. While this chapter is not meant to give an in-depth explanation of nonlinear dynamics, we will discuss a few important concepts to help in understanding the work presented later in this thesis.

Nonlinear systems can be described as any system that is not linear. Therefore, we will define what is a linear system and some of the dynamics that are observed. Mathematically, a linear system can be expressed as $f(x) = mx$, where $f(x)$, is the output, x is the input, and m is a scalar or proportionality constant [4, 6, 17]. Any change or addition to the system will cause a proportional response by the system. This approach is commonly used in analytically chemistry to determine the concentration of an analyte by using a variety of experimental methods. Unfortunately, as useful as these techniques are, they only work when there is a linear response in the system. As an example, the Beer-Lambert law, $A = \epsilon BC$, breaks down at higher concentrations as the calibration curve loses linearity [18, 19]. Therefore, any technique using this relationship can only use concentrations that fall in the linear regime of the curve.

In nonlinear systems changes are no longer proportional, and the equations describing them may contain terms such as x^2 or trignometric functions like sine or cosine as examples [6]. We can demonstrate differences between linear and nonlinear descriptions of a system by using the motion of a pendulum as an example. Dutch physicist Christian Huygens invented the pendulum clock in 1657 and published a book in 1673 *Oscillatorium* on clock designs, which also contained an in-depth analysis of pendulum motion. Huygens described a simple pendulum as a point mass, m, hanging from an arm with a negligible mass of length, L, which is fixed at a point, P, Fig. 1.1. The differential equation governing the motion of the pendulum was written by Huygens as

$$\frac{d^2\theta}{dt^2} + \frac{g}{L} sin\theta = 0, \tag{1.1}$$

where θ is the angular displacement, g is gravitational force, and L is the length of the arm. This nonlinear equation can describe the motion of the pendulum at any given value of θ; however, this equation can become cumbersome to solve analytically. To turn this into a linear system, we assume a small angular displacement such that the angular displacement is directly proportional

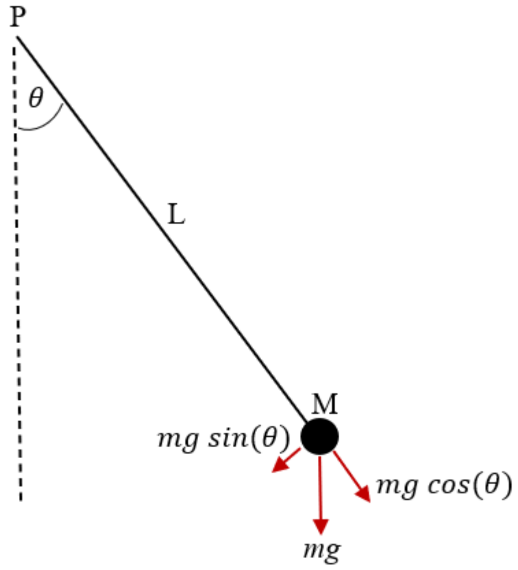

Figure 1.1. A pendulum is described as a small mass, m, attached to an arm of negligible mass with a length, L, which is fixed to a point P. The restoring force acting on the mass is gravity g. The angular displacement θ represents how far the mass is from equilibrium, shown by the dashed line. Figure reproduced from Nonlinear Dynamics and Chaos [6]

.

to its angular acceleration $sin(\theta) \approx \theta$; Eq. (1.1) then simplifies to

$$\frac{d^2\theta}{dt^2} + \frac{g}{L}\theta = 0. \tag{1.2}$$

Taking the simple harmonic solution

$$\theta(t) = \theta_0 cos(\omega t), \tag{1.3}$$

where θ_0 is the initial displacement and $\omega = \sqrt{gL}$, we can now readily solve for the period of a single oscillation using

$$T = 2\pi\sqrt{L/g}. \tag{1.4}$$

While linearization is useful, it may only be valid when making certain assumptions about the system, as we have demonstrated. We also lose information about our system, as we can not use Eq. (1.4) when the angular displacement is large. One of the most well-know examples of using a nonlinear treatments over a linear one came in the late 1800s by Henri Poincaré [20, 21]. The three-body problem proposed by Newton was essentially impossible to solve using explicit methods without placing restrictions on the problem. Poincaré was able to show that there are an infinite number of periodic solutions to this problem [20, 21]. This discovery changed how we view planetary orbits and predicting their paths through space.

1.2 Stability and Bifurcations

Poincaré's work was revolutionary at the time because he was interested in not just how to calculate where a body may be at a given time, but whether or not the solutions are stable. However, as we mentioned before, nonlinear equations are often impossible to solve analytically. Even when it is possible to solve the equation exactly, the solution can be difficult to interpret. Poincaré developed a geometric way of analysis to simplify the question of stability using first-order equations [6, 20]. When using first-order equations, we can determine stability by looking at the solutions as a vector field along a line. As an example of this is that we can exactly solve the nonlinear equation

$$\frac{dx}{dt} = sin(x). \tag{1.5}$$

First, we separate our variables such that

$$dt = \frac{dx}{sin(x)}. \tag{1.6}$$

When we integrate Eq. (1.6), our solution is

$$t = -ln|csc(x) + cot(x)| + C. \tag{1.7}$$

To arrive at an exact solution, we will evaluate the constant C such that $x = x_o$ at $t = 0$, giving C equal to $ln|csc(x) + cot(x)|$. Substituting this value into Eq. (1.7) will give the solution

$$t = ln\left|\frac{csc(x_o) + cot(x_o)}{csc(x) + cot(x)}\right|. \tag{1.8}$$

This treatment gave us an exact mathematical solution, and we know that the fixed points are at nπ, where n is $\mathbb{Z} \in (-\infty, \infty)$. However, the dynamics of the system at any given point or time are not transparent. When we consider the initial condition of $x_o = \frac{\pi}{4}$ at $t = 0$, it is not clear how the system will move as $t \to \infty$. Poincaré's geometric approach in analyzing such problems provides a clear answer, and it has continued to be used in the modern day field of dynamics. Again, we consider Eq. (1.5) and plot the solution to this equation from -3π to 3π, Fig. 1.2. Now we can go back and analyze our question of what happens when $x_o = \frac{\pi}{4}$ at $t = 0$ as $t \to \infty$. Here, x represents the position in the trajectory of a vector field moving along a real line, and t is equal to time. Then $\frac{dx}{dt}$ is the velocity of the particle as it moves along the line. It is easy to see that at $\frac{\pi}{4}$ the velocity of the particle is increasing as it approaches its maximum at $\frac{\pi}{2}$. Then the velocity of the particle begins to decrease as it approaches a fixed point at π until it reaches zero at the fixed point. When the velocity of the particle is zero, there is no flow in the system and the particle is stationary. This observation leads us to the conclusion that as $t \to \infty$ when $\frac{dx}{dt} > 0$ then the flow is to the right. When $\frac{dx}{dt} < 0$ the flow is to the left. When we place arrows pointing to the direction of the flow, as in Fig. 1.2, we can see that the solid black dots represent stable fixed points, while the white dots are unstable points. The idea of using a first order approximation is an important tool when doing stability analysis on complex

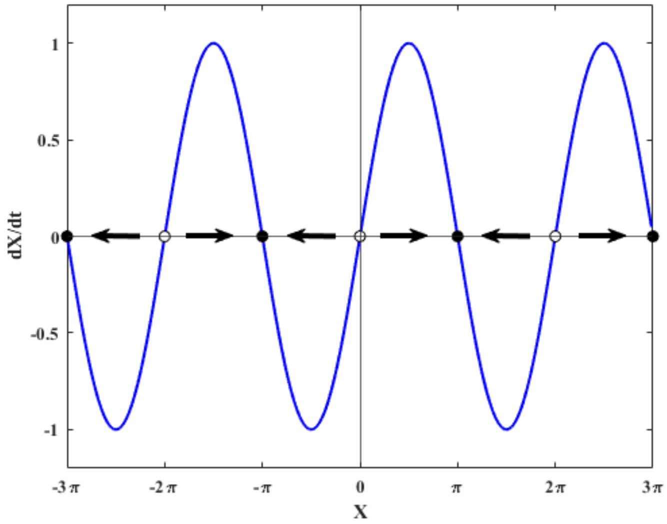

Figure 1.2. Visualization of the equation sin(x) from -3π to 3π. The solid black dots represent the stable fixed points of the system and the white circles represent unstable fixed points in the system. Black arrows show the flow of the system from unstable points to stable points.

systems or systems with higher dimensionality.

In his first paper in mathematics, Henri Poincaré coined the term bifurcation [20]. A bifurcation occurs when a small change in a single parameter value causes a sudden change in the observed behavior. A classic example is a saddle-node bifurcation where two fixed points move toward one another until they merge and then disappear [6]. This behavior can be demonstrated using the equation

$$\frac{dx}{dt} = b + x^2, \tag{1.9}$$

where b is the bifurcation parameter. It is trivial to find the fixed points for any value of b ≤ 0, and we can use the geometric approach to determine their stability. By varying the parameter b, we can observe the fixed points moving closer to each other until they merge and annihilate. When we let b = -5, we find two fixed points exist, one stable and the other unstable, Fig. 1.3(a). When we increase the value such that b = -2, we can see that the fixed points moved closer to each other but the stability of the fixed points did not change, Fig. 1.3(b). However, when we let b = 0, a change in the number of fixed points occurs, which is the bifurcation point. There is now only one fixed point, which has the property of being stable in one direction and unstable in the other direction, Fig. 1.3(c). Finally, when we set b to any value greater than zero, such as b = 2, there are no fixed points in the system, Fig. 1.3(d).

The ideas illustrated by Eqs. (1.5) and (1.9) are still used today but are not a complete explanation of Poincaré's work. Dynamical systems described by a single first-order equation are dominated by fixed points [6, 20, 21]. Any initial condition will lead to the trajectory remaining constant, converging monotonically to a stable fixed point, or diverging to $\pm\infty$. This observation leads us to conclude that oscillations cannot occur in first-order systems, since trajectories will monotonically approach zero at the fixed point. This idea may seem counter intuitive, as oscillatory behavior is very common in nonlinear dynamics. We know our pendulum example from earlier oscillates about an axis and seems to contradict the previous statement. However, the motion of the pendulum can not be described by only its position. To uniquely describe the state of the pendulum at a given time, we need the position and the velocity. More specifically, the sign of the velocity is needed to indicate the direction in which the pendulum is moving. Removing the nonlinear aspects of Eq. (1.1) allowed us to calculate the period of an oscillation by removing the nonlinear aspects. However, simple harmonic motion is a two dimensional system, position and velocity, and it is not constrained by our earlier statement and it can produce oscillations.

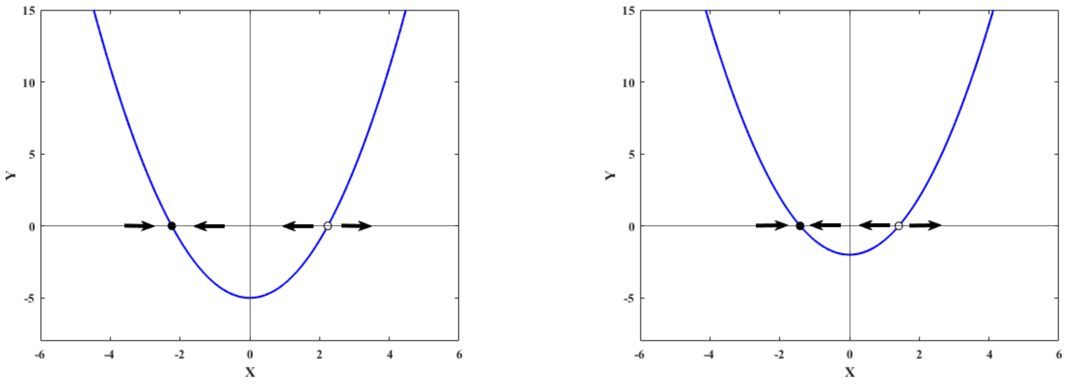

(a) parameter b = -5

(b) parameter b = -2

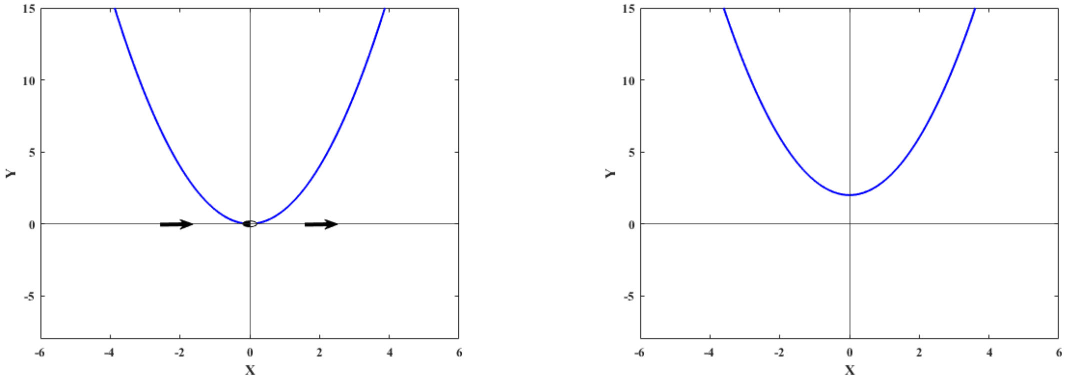

(c) parameter b = 0

(d) parameter b = 2

Figure 1.3. Graphical representation of the equation $\frac{dx}{dt} = b + x^2$ for four different values of the parameter b. (a) Parameter b = -5 showing two fixed points of different stability. (b) Parameter b = -2 showing two fixed points that have shifted closer while maintaining the same stability. (c) A change in the system when b = 0, where the fixed points have merged into a single point with the property of being both stable and unstable. (d) When b > 0, all fixed points disappear from the system.

1.3 Oscillatory Behavior

Oscillatory behavior can be observed in many areas of study: certain chemical reactions [22–24], the beating of the heart [25–27], the firing of neurons in the brain [28–30], populations of animals [31–33], the eruption of geysers [34–36], and the orbit of the planets [6, 20, 21] are just a few examples. There are several types of oscillatory behavior, such as damped, undamped, and driven oscillations. We will focus on a special type of oscillations known as limit cycle oscillations. Limit cycle oscillations model systems that possess self-sustained oscillations in the absence of periodic forcing [6]. This type of oscillation is found in the human heart [25–27], pacemaker neuronal firing, chemical oscillators [22–24], electrical circuits [37], self-excited vibrations on airplane wings [38], and the Sel'kov model of glycolysis [39]. This type of oscillation produces an isolated closed orbit that acts as an attractor in the system. Any neighboring trajectories in the vicinity of the limit cycle are either attracted to or repelled from the limit cycle [6]. In contrast, damped, undamped, and driven oscillations have closed trajectories but are not isolated. By slightly perturbing or changing a parameter of the system, a non-limit cycle oscillation will move along the new orbit and not return to the previous orbit. As an example, in a system defined as $\overrightarrow{F} = k\overrightarrow{x}$ that produces closed orbits, any change to the system in the form of increasing or decreasing the parameter, k, we see the oscillator move to the newly created closed trajectory, Fig. 1.4. Limit cycle oscillations are strictly a nonlinear behavior and are not observed in linear systems. This makes it necessary to solve the nonlinear equations to model these scientifically important behaviors.

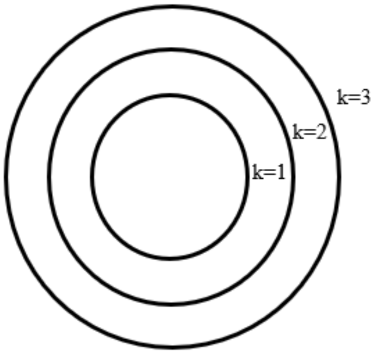

Figure 1.4. Closed orbits of a linear system, which produces oscillations. As the parameter, k, changes, the oscillator will move to the new trajectory without returning to the previous one.

To determine the stability of the limit cycle, we examine how an initial trajectory proceeds in the vicinity of the limit cycle or the response to a small perturbation of a trajectory on the limit cycle, Fig. 1.4. For a stable limit cycle, as time → ∞, any trajectory in the vicinity of the limit cycle will be attracted to it. For a trajectory on the limit cycle receiving a small

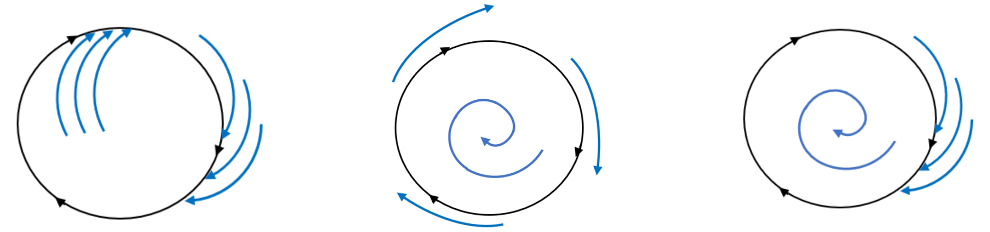

(a) Stable Limit Cycle (b) Unstable Limit Cycle (c) Semi-Stable Limit Cycle

Figure 1.5. A hypothetical limit cycle demonstrating the different types of stability. The limit cycle is an isolated closed orbit that can either attract or repel nearby trajectories. (a) A stable limit cycle will attract all nearby trajectories it the limit. A trajectory perturbed from the limit cycle will return to the limit without forcing. (b) An unstable limit cycle will repel all nearby trajectories from the limit cycle. A trajectory perturbed from the unstable limit cycle will not return to the limit cycle. (c) In a half-stable limit cycle, the limit cycle will attract in one direction and repel in the other direction. Perturbations to trajectories pushing it in the stable direction will cause the trajectory to return to the limit cycle. If the perturbation is in the unstable direction, the trajectory will not return to the limit cycle. The stable and unstable direction depends on the system.

perturbation in any direction away from the limit cycle, the trajectory will return to the limit cycle, Fig. 1.4(a). These stable limit cycles are observed in models of the Belousov-Zhabotinsky [40] reaction as well as the FitzHugh-Nagumo neuronal model [41]. In the case of the unstable limit cycle, as time → ∞, trajectories outside the limit cycle will be repelled away to infinity. The trajectories inside the limit cycle will be converge to a fixed point inside the limit cycle, Fig 1.4(b). A small perturbation on a trajectory exactly on the limit cycle will cause the trajectory to move either in the direction of infinity or converge to the fixed point. Half-stable limit cycles are a combination of the former two behaviors. On one side of the limit cycle trajectories will converge to the limit cycle, while the other side will repel them, Fig. 1.4(c). In our example, trajectories outside the limit will converge to it and trajectories inside will converge to the fixed point. The directions of the stable and unstable behaviors will depend on the system.

1.4 Subcritical Hopf Bifurcation

There are many types of bifurcations that describe the behavior of nonlinear oscillatory models. Since the bulk of this work focuses on behaviors using models of the Belousov-Zhabotinsky reaction, we will focus only on describing the subcritical Hopf bifurcation [40, 42–44]. To do this, let us consider the following two-dimensional system

$$\frac{dr}{dt} = \mu r + r^3 - r^5, \tag{1.10}$$

$$\frac{\theta}{dt} = \omega + br^2, \tag{1.11}$$

where μ represents the stability of the fixed point, ω is the frequency of small oscillations, and b determines the frequency dependence of larger amplitude oscillations. Upon examining Eq. (1.10), we can see that it contains a destabilizing cubic term r^3, which drives trajectories away from the origin. When $\mu < 0$, there are two stable attractors in the system. The first one is a stable fixed point at the origin and a stable limit cycle, and between them is an unstable limit cycle, Fig. 1.6(a). As μ approaches zero, the unstable limit cycle shrinks and moves closer to the stable fixed point at the origin. The subcritical Hopf bifurcation occurs when $\mu = 0$ and the amplitude of the unstable limit cycle becomes zero. This changes the stability of the fixed point, making it unstable, Fig. 1.6(b). Now any trajectories inside the limit cycle will be attracted to the limit cycle, becoming large amplitude oscillations. This type of bifurcation is significant as it allows for the existence of mixed-mode oscillations, producing both small and large amplitude oscillations. Mixed-mode oscillations have been reported in numerous systems including the Oregonator [44–48] and FitzHugh-Nagumo models [49–51].

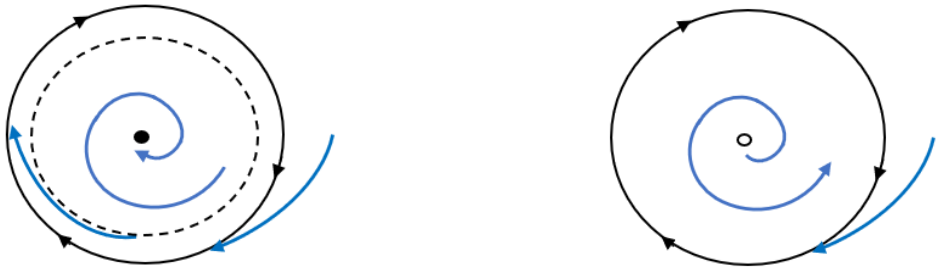

(a) $\mu < 0$

(b) $\mu > 0$

Figure 1.6. A representation of a subcritical Hopf bifurcation. (a) When μ is < 0, the system contains a stable fixed point and limit cycle with an unstable limit cycle between them. (b) As μ approaches zero, the unstable limit cycle approaches the stable fixed point. At $\mu = 0$, the unstable limit cycle merges with the fixed point making it unstable.

1.5 Lorenz Equations

With computers becoming more widely available in the late 1950's it became possible to study more complex nonlinear systems. In 1963 Ed Lorenz was interested in the prediction of weather patterns, which was notoriously difficult to do [52]. He derived a simplified 3-variable model for describing convection rolls in the atmosphere, Eqs. (1.12)-(1.14).

$$\frac{dx}{dt} = \sigma(y - x) \tag{1.12}$$

$$\frac{dy}{dt} = rx - y - xz \tag{1.13}$$

$$\frac{dz}{dt} = xy - bz \tag{1.14}$$

Here, σ, r, b are positive parameters. Lorenz observed that over a wide range of parameters the dynamics of the system would not settle to a limit cycle or a fixed point. The solutions to the equations would oscillate, but never repeat the exact same trajectory, yet seemed to be bounded to a defined region. When Lornez would plot the trajectories in 3 dimensions, he observed that the trajectories would settle into a complex set, which would become known as a strange attractor. Two examples of this strange attractor in the Lorenz system are shown in Fig. 1.7. We can see that a slight change in the initial conditions of the system produces completely

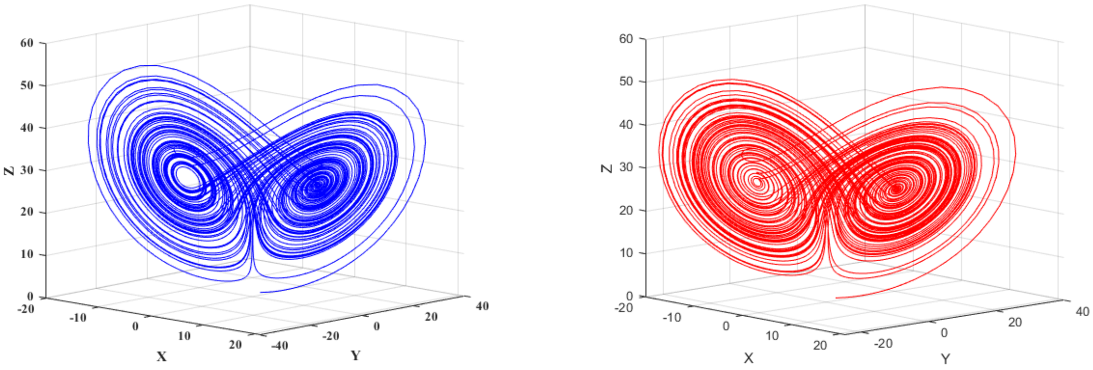

(a) $\sigma = 1.00$ $r = 1.00$ $b = 1.05$ (b) $\sigma = 1.05$ $r = 1.05$ $b = 1.00$

Figure 1.7. Strange attractor first reported by Lornez in his 3 variable model of convection rolls. A trajectory on this attractor will not repeat a periodic orbit but is confined to the set that makes up the attractor. Small changes in the initial conditions will send trajectories on different unpredictable paths. Slight changes to the initial conditions sends trajectory (b) in to a completely different orbit.

different trajectories. Fig. 1.7(a) and Fig. 1.7(b) show behavior that is the hallmark of what has become known as deterministic chaos [6, 15, 53]. This sensitivity to initial conditions and slight perturbations means there are an infinite number of trajectories that can be produced. While predicting exact outcomes in chaotic systems may be impossible, it can provide a useful understanding of how the dynamics of a system evolve. There are many notable examples of chaotic systems, such as turbulent fluid flow [54], irregular heartbeats [55], population dynamics [56, 57], and chemical reactions [15, 53]. The Belousov-Zhabotinsky is one such chemical reaction were chaos has been observed [15, 53], which will be discussed in Chapter 4.

1.6 Synchronization

Up to this point, we have only discussed behaviors and properties of single oscillators. Many natural systems consist of networks of oscillators that interact with one another [58–63]. When oscillators are coupled to create a network, even more complex and interesting dynamics can emerge. Dutch physicist Christian Huygens, inventor of the pendulum clock, is also credited for first reporting on synchronization in 1665 [64]. He observed that the pendulums of two individual clocks resting on the same support would synchronize, swinging in opposite directions. He could then disturb the motion of one of the pendulums and observe as it would eventually synchronize with the other pendulum. The observation that he reported is now known as entrainment or coupling. The phenomenon is explained by the motion of the pendulum creating a force as it swings, which is passed through the common rest. The motion of the second pendulum is effected by this force and slightly changes its trajectory. Likewise the second pendulum exerts a force on the support that is felt by the first pendulum. This signaling causes changes in the motions of both pendulums and eventually leads to their synchronization. To define this phenomenon of synchronization, we can describe it as an adjustment towards a common behavior between coupled discrete dynamical systems [65]. Synchronization has become an important area of research, as it is ubiquitous in natural systems, including heart cells [66], neuronal networks [65, 67, 68], insects such as fireflies and crickets [58, 59, 69], pancreatic cells [70], and hormone release [71].

Art Winfree developed a model of weakly coupled limit cycle oscillators that helped explain synchronization by using the phase of the oscillators [72]. In this work, he showed that in weakly coupled systems variations of amplitude are negligible because changes to a trajectory due to small perturbations will converge quickly back to the limit cycle. With a negligible change in amplitude, the time evolution of the oscillators can be described by their phase. In Winfree's model, he demonstrated that a population of homogeneous oscillators with a distribution of phases or heterogeneous oscillators with a small distribution of periods would synchronize above a critical coupling strength. Later studies on the synchronization of heterogeneous populations of oscillators would show that as the natural period distribution increases, the larger the coupling strength would be to cause full synchronization or phase locking. If the period distribution was too large, oscillators at the extreme tails of the distribution may not synchronize with the mean group. Increasing the coupling strength to much to try and entrain these outliers may lead to the system becoming non-oscillatory or oscillator death.

1.7 Overview

The experimental and theoretical studies described in this work will utilize weakly coupled networks of chemical oscillators and in the computational models that describe them. In Chapter 2, we will discuss in detail the chemistry of the Belousov-Zhabotinsky (BZ) reaction. As well as the photochemistry observed in the ruthenium-catalyzed BZ reaction. Two different models that describe this reaction will be discussed. The first model is the modified 4-variable Oregonator, which accounts for both the photosensitive nature of the ruthenium catalyst and the subcritical Hopf bifurcation near the reduced catalyst side. The second model is the modified 3-variable ZBKE model that describes in more detail the chemistry of the resetting mechanism and can also describe the photosensitivity of the ruthenium catalyst. Novel modes of synchronization are the subject of Chapter 3 using BZ chemical oscillators and the ZBKE model. Here, we will discuss the chemistry and theoretical modeling of the formation of phase clusters in unconnected nodes of a heterogeneous star system. Finally, in Chapter 4 we will show computational results using two homogeneous coupled oscillators demonstrating extreme events. The mixed mode behavior in this system is credited to the subcritical Hopf bifurcation, which is observed in the modified 4-variable Oregonator.

References

1. D. K. Campbell, *Nature* **432**, 455 (2004).
2. C. L. Phillips, J. M. Parr, E. A. Riskin, *Signals, Systems, and Transforms* (Pearson, New York, New York, 2008).
3. B. J. Horst, *MIMO Signals and Systems* (Springer, New York, New York, 2005).
4. A. Oktay, *Signals and Systems: A MATLAB Integrated Approach.* (CRC Press, Boca Raton, Florida, 2014).
5. M. Nahvi, *Signals and Systems* (McGraw-Hill, New York, New York, 2014).
6. S. H. Strogatz, *Nonlinear Dynamics and Choas with Applications to Physics, Biology, Chemistry, and Engineering* (Westview Press, Philadelphia, Pa., 1994).
7. B. Ping, R. Shigui, *SIAM J. App. Dyn. Sys.* **12**, 1847 (2013).
8. D. Fan, H. Ling, *Comm. Non. Sim.* **15**, 1873 (2010).
9. A. F. Taylor, P. Kapetanopoulos, B. J. Whitaker, T. Toth, L. Bull, M. Tinsley, *Phys. Rev. Lett.* **100**, 214101–1 (2008).
10. M. F. Crowley, I. R. Epstein, *J. Phys. Chem.* **93**, 2496 (1989).
11. A. N. Pisarchik, *Phys. Rev. E.* **64**, 046203 (2001).
12. I. R. Epstien, K. Showalter, *J. Phys. Chem.* **100**, 13132 (1996).
13. G. B. Ermentrout, C. C. Chow, *Physiol. Behav.* **77**, 629 (2002).
14. A. M. Zhabotinsky, V. K. Vanag, *J. Chem. Phys.* **104**, 11566 (2000).
15. L. Györgyi, R. J. Field, *Nature* **355**, 808 (1992).
16. D. Zhang, L. Györgyi, *Chaos* **3**, 723 (1993).

17. R. J. Michael, *Signals and Systems: Analysis Using Transform Methods and MATLAB* (McGraw-Hill, New York, New York, 2018).
18. D. A. Skoog, J. F. Holler, S. R. Crouch, *Principles of Instrumental Analysis* (Cengage, Boston, Ma., 2007).
19. D. C. Harris, *Quantitative Chemical Analysis* (W.H. Freeman and Company, New York, New York, 2014).
20. H. Poincaré, *Acta Mathematica* **7**, 259 (1885).
21. H. Poincaré, *Celextial Mechanics* (American Institute of Physics, Woodbury, New York, 1993).
22. A. M. Zhabotinsky, *Chaos* **1**, 379 (1991).
23. A. M. Zhabotinsky, F. Buchholtz, A. B. Kiyatkin, I. R. Epstein, *J. Phys. Chem.* **97**, 7578 (1993).
24. I. R. Epstien, J. A. Pojman, *An Introduction to Nonlinear Chemical Dynamics: Oscillatoions, Waves, Patterns, and Chaos* (Oxford Univeristy Press, New York, New York, 1998).
25. A. Babloyantz, A. Destexhe, *Biol. Cybern.* **58**, 203 (1988).
26. U. Zwiener, D. Baue, B. Lüthke, B. Walter, K. Schmidt, S. Hallmeyer, B. Kratzsch, M. Eiselt, *Cardiovasc Res.* **31**, 455 (1996).
27. S. Guzzetti, M. G. Signorini, C. Coliati, S. Mezzetti, A. Porta, S. Cerutti, A. Mallian, *Cardiovasc Res.* **31**, 441 (1996).
28. M. N. Havenith, Y. Shan, J. Biederlack, C. Nan-Hui, W. Singer, D. Nikolić, *J. Neurosci.* **31**, 8570 (2011).
29. T. Chouzouris, A. Omelchenko, A. Zakharova, J. Hlinka, P. Jiruska, E. Schöll, *Chaos* **28**, 045112 (2018).
30. L. Glass, *Nature* **410**, 277 (2001).
31. S. Sakanoue, *Eco. Mod.* **205**, 159 (2007).
32. N. Meade, *Roy. Stat. Soc.* **151**, 491 (1988).

33. W. Jin, S. McCue, M. J. Simpson, *J. Theor. Biol.* **445**, 51 (2018).
34. Y. Furushima, M. Nagao, A. Suzuki, H. Yamamoto, T. Maruyama, *Mar. Technol. Soc. J.* **43**, 13 (2009).
35. S. E. Ingebritsen, S. A. Rojstaczer, *J. Geophys. Res. Solid Earth* **101**, 21891 (1996).
36. S. E. Ingebritsen, S. A. Rojstaczer, *Science* **262**, 889 (1993).
37. H. Schmidt, *Limit Cycle Computation of Oscillating Electric Circuits* (Birkhäuser, Basel, Switzerland, 1994).
38. R. W. Bunton, C. M. Denegri, *J. Aircr.* **37**, 916 (2012).
39. E. E. Sel'kov, *Eur. J. Bio. Chem.* **4**, 79 (1968).
40. S. Scott, *Oscillations, Waves, and Chaos in Chemical Kinetics* (Oxford University Press, Oxford, England, 1994).
41. F. Kaiser, *Biol. Cybernetics* **27**, 155 (1977).
42. P. Strizhak, M. Menzinger, *J. Chem. Educ.* **73**, 868 (1996).
43. M. Brøns, K. Bar-Eli, *J. Phys. Chem.* **95**, 8706 (1991).
44. S. Kádár, T. Amemiya, K. Showalter, *J. Phys. Chem. A* **101**, 8200 (1997).
45. K. Showalter, R. Noyes, K. Bar-Eli, *J. Chem. Phys.* **67**, 2514 (1978).
46. M. Rachwalska, A. Kawczynkis, *J. Phys. Chem. A* **103**, 3455 (1999).
47. M. Schell, F. N. Albahadily, *J. Chem. Phys.* **90**, 822 (1989).
48. M. K. Reddy, Z. Szlavik, Z. Hagy-Ungvarai, S. C. Müller, *J. Phys. Chem.* **99**, 15081 (1995).
49. G. Ansmann, R. Karnatask, K. Lehnertz, U. Feudel, *Phys. Rev. E* **88**, 052911 (2013).
50. A. Saha, U. Feudel, *Phys. Rev. E.* **95**, 062219 (2017).
51. A. Saha, U. Feudel, *Chaos* **28**, 033610 (2018).
52. E. Lorenz, *JAS* **20**, 130 (1963).
53. V. Petrov, V. Gáspár, J. Masere, K. Showalter, *Nature* **361**, 240 (1993).
54. Y. L. Klimontovich, *Turbulent Motion. The Structure of Chaos* (Springer, Dordrecht, 1991).

55. S. V. Buldyrev, A. L. Goldberger, S. Havlin, C. K. Peng, H. E. Stanley, *Fractals in Biology and Medicine: From DNA to the Heartbeat* (Springer, Berlin, Heidelberg, 1994).

56. L. Eduardo, A. Ruiz-Herrera, *J. Appl. Dynam. Sys.* **11**, 1200 (2012).

57. L. Dejian, *Comp. Stat. Dat. Ana.* **22**, 409 (1996).

58. J. Buck, E. Buck, *Science* **159**, 1319 (1968).

59. J. Buck, E. Buck, J. F. Case, F. E. Hanson, *J. Comp. Physiol.* **144**, 287 (1981).

60. Y. Yoshimura, E. M. Callaway, *Nat. Neurosci.* **8**, 1552 (2005).

61. Y. Yoshimura, L. M. Dantzker, E. M. Callaway, *Nature* **433**, 868 (2005).

62. M. Bartos, I. Vida, P. Jonas, *Nat. Rev. Neurosci.* **8**, 45 (2007).

63. E. Marder, D. Bucher, *Curr. Bio.* **11**, 249 (2001).

64. E. Klarreich, *SIAM News* **35**, 8 (2002).

65. G. Osipov, J. Kürths, C. Zhou, *Synchronization in Oscillatory Networks* (Springer, Berlin, 2010).

66. C. Peskin, *Courant Institute of Mathmatical Science Publication* **1**, 268 (1975).

67. A. Pikovsky, M. Rosenblum, J. Kürths, *Synchronization: A Universal Concept in Non-Linear Sciences* (Cambridge University Press, Cambridge, Mass., 2003).

68. F. Hoppensteadt, E. Izhikevich, *Weakly Connected Neural Networks* (Springer-Verlag, New York, New York, 1997).

69. T. Walker, *Science* **166**, 891 (1969).

70. C. Cherubini, S. Filipp, A. Gizzi, A. Loppini, *Phys. Rev. E* **92**, 042702 (2015).

71. R. Boyar, J. Finkelstien, H. Roffwarg, S. Kapen, E. Weitzman, L. Hellman, *N. Engl. J. Med.* **287**, 582 (1972).

72. A. Winfree, *J. Theor. Biol.* **16**, 15 (1967).

Chapter 2

The Belousov-Zhabotinsky Reaction

2.1 Introduction

The investigations carried out in this work are based on the chemistry of the Belousov-Zhabotinsky (BZ) reaction. The BZ reaction is described as the metal-catalyzed bromination and oxidation of an organic substrate in an acidic bromate solution and is a classic example of a nonlinear chemical oscillator [1–3]. The overall BZ reaction is described by Eq. (2.1).

$$3BrO_3^- + 5CH_2(COOH)_2 + 3H^+ \rightarrow 3BrCH(COOH)_2 + 4CO_2 + 2HCOOH + 5H_2O \quad (2.1)$$

This reaction proceeds far from equilibrium and is capable of producing relaxation-type oscillations [1–5], spatiotemporal patterns [6–8], and chaos [4, 9–12]. Experimentally, networks of discrete photosensitive BZ oscillators are created using real-time or time-delayed light based feedback [13–16]. In this chapter, we discuss the history and mechanism of the BZ reaction as well as the photosensitivity of a commonly used metal catalyst, tris(bipyridine)ruthenium(II) chloride. We will also discuss two of the computational models used to describe the BZ reaction, and their modification to account for the photosensitivity of the system when using a ruthenium catalyst. Finally, we will examine how to measure the response of an oscillator due to a perturbation from the light-based feedback by use of a phase response curve, PRC.

2.2 History of the Belousov-Zhabotinsky Reaction

The BZ reaction is one of the most well-known examples of a chemical oscillator. The reaction produces significant oscillations in the concentrations of bromide ions, bromous acid, and the oxidation state of the metal catalyst [1–3]. The reaction was discovered by Boris Belousov in 1951, while serving as the head of a laboratory of biophysics for the USSR Ministry of Health[3, 17–19]. Belousov was working on creating an experimental model for the Krebs cycle [18], the oxidation of acetyl-Co A into carbon dioxide and chemical energy in the form of adenosine triphosphate [20]. Belousov was experimenting with an acidic bromate solution containing citric acid and a cerium metal ion that began producing carbon dioxide bubbles. He observed that the solution underwent a periodic change between a colorless solution and a faint yellow color for well over an hour [3, 18]. However, when Belousov attempted to publish his discovery, the papers were rejected each time [3, 18, 19]. At this time, it was believed that chemical oscillations such as those described by Belousov were impossible, since the reaction would need to oscillate about the chemical equilibrium point, which would violate the second law of thermodynamics. Belousov was finally able to get an abbreviated abstract of his discovery published in a small booklet entitled *A Collection of Short Papers on Radiation Medicine* by his own institute [3, 17, 18]. The discovery would remain unknown for a decade, until it was assigned to a graduate student, Anatol M. Zhabotinsky, at Moscow State University in 1961. Zhabotinsky was able to reproduce Belousov's results and began to conduct new experiments with the system. Zhabotinsky made improvements to the recipe by replacing the citric acid with malonic acid and the cerium ion with ferrion [3]. Both of these changes improved the optical clarity of the oscillations. He was also able to show that the oscillations in the color were due to the oxidation/reduction of the metal catalyst and not the free bromine ion concentration that Belousov had hypothesized [3]. Zhabotinsky's most sigificant contribution may have been his ability to get the reaction published and out to the scientific community, although it would still be almost another decade before the first papers in English were published in 1967 [18].

2.3 Belousov-Zhabotinsky Reaction Mechanism

Given any closed homogeneous system at a constant temperature and pressure, a spontaneous chemical change must be accompanied by a decrease in the Gibbs free energy of the system. However, this condition does not prevent oscillations in chemical concentrations as long as the system does not pass through the chemical equilibrium. In 1972, Field, Körös, and Noyes proposed a mechanism that could explain the oscillations observed in the BZ reaction using a single autocatalytic step [1]. Field et al. used several experimental techniques, such as ion-selective electrodes and paper chromatography, to track the concentrations of reactants and to determine the kinetics of the elementary steps [1]. This would become known as the FKN mechanism and consists of ten elementary reactions, Eqs. (2.2)-(2.11) [1].

$$BrO_3^- + Br^- + 2H^+ \rightarrow HBrO_2 + HOBr \tag{2.2}$$

$$HBrO_2 + Br^- + H^+ \rightarrow 2HOBr \tag{2.3}$$

$$HOBr + Br^- + H^+ \rightleftharpoons Br_2 + H_2O \tag{2.4}$$

$$BrO_3^- + HBrO_2 + H^+ \rightleftharpoons 2BrO_2^\bullet + H_2O \tag{2.5}$$

$$BrO_2^\bullet + Ce^{3+} + H^+ \rightleftharpoons HBrO_2 + Ce^{4+} \tag{2.6}$$

$$2HBrO_2 \rightarrow BrO_3^- + HOBr + H^+ \tag{2.7}$$

$$BrO_2^\bullet + Ce^{4+} + H_2O \rightarrow BrO_3^- + Ce^{3+} + 2H^+ \tag{2.8}$$

$$Br_2 + CH_2(COOH)_2 \rightarrow BrCH(COOH)_2 + Br^- + H^+ \tag{2.9}$$

$$6Ce^{4+} + CH_2(COOH)_2 + H_2O \rightarrow 6Ce^{3+} + HCOOH + 2CO_2 + 6H^+ \tag{2.10}$$

$$4Ce^{4+} + BrCH(COOH)_2 + 2H_2O \rightarrow Br^- + 4Ce^{3+} + HCOOH + 2CO_2 + 5H^+ \tag{2.11}$$

This detailed mechanism can be summarized by grouping the essential equations and placing them into three processes, which we will call "Processes A, B, and C." It should be noted that all of these reactions are happening concurrently. However, as this oscillatory reaction proceeds one of the processes will dominate over the others as the concentrations of the primary reactants change in time. At the beginning of the reaction, when the concentration of the bromide ions are at, or near, their maximum, Process A is dominant. Process A can be described as the removal of bromide ions by bromate, hypobromous acid and bromous acid.

Process A (removal of bromide ions):

$$BrO_3^- + Br^- + 2H^+ \rightarrow HBrO_2 + HOBr \tag{2.2}$$

$$HBrO_2 + Br^- + H^+ \rightarrow 2HOBr \tag{2.3}$$

$$HOBr + Br^- + H^+ \rightleftharpoons Br_2 + H_2O \tag{2.4}$$

As the bromide ion concentration falls, it reaches a critical concentration and Process B begins to dominate the reaction. At this point, the bromous acid can outcompete the bromide ions and begins reacting with bromate, initiating the autocatalytic production of bromous acid and the oxidation of the metal catalyst cerium. In Eq. (2.5), the product of the reaction between bromous acid and bromate yields two radical species. Each of these radicals can oxidize the metal catalyst and produce bromous acid. It can be clearly seen from Eqs. (2.5) and (2.6) that for each bromous acid consumed, two bromous acids are formed. The concentration of bromous acid rapidly increases due to its autocatalytic production. The reaction between bromous acid and bromide ions, shown in Eq. (2.3), continues to proceed and the concentration of bromide ions is quickly reduced.

Process B (autocatalytic production of bromous acid):

$$BrO_3^- + HBrO_2 + H^+ \rightleftharpoons 2BrO_2^\bullet + H_2O \tag{2.5}$$

$$BrO_2^\bullet + Ce^{3+} + H^+ \rightleftharpoons HBrO_2 + Ce^{4+} \tag{2.6}$$

$$2HBrO_2 \rightarrow BrO_3^- + HOBr + H^+ \tag{2.7}$$

With the sudden increase in the oxidized form of the metal catalyst, Process C becomes dominant. This process acts as the resetting mechanism, as the metal catalyst is reduced and bromide ions are liberated from the organic substrate.

Process C (reduction of metal catalyst and liberation of bromide ions):

$$6Ce^{4+} + CH_2(COOH)_2 + H_2O \rightarrow 6Ce^{3+} + HCOOH + 2CO_2 + 6H^+ \tag{2.10}$$

$$4Ce^{4+} + BrCH(COOH)_2 + 2H_2O \rightarrow Br^- + 4Ce^{3+} + HCOOH + 2CO_2 + 5H^+ \tag{2.11}$$

As the concentration of bromide ions rises above the critical concentration, once again Process A becomes dominant and the cycle repeats. The critical concentration of bromide ions can be estimated by setting the rate equations of Eq. (2.3) and Eq. (2.5) equal to one another and rearranging to solve for [Br$^-$], yielding Eq. (2.12) [1].

$$[Br^-]_{crit} = \frac{k_{2.5}}{k_{2.3}}[BrO_3^-] \tag{2.12}$$

For the cerium system, the ratio of the rate constants $k_{2.5}/k_{2.3}$ is equal to 5×10^{-6}. Observations by Field et al. showed semiquantitative agreement with this equation [1]. As the other reactant concentrations are varied, bromate was held constant at 0.063 M. Through these experiments, the critical concentration of bromide ions was between 8.0×10^{-7} M and 1.0×10^{-6} M.

2.4 Photosensitive BZ Reaction

There have been other metal catalysts used in the BZ reaction since Belousov first used cerium [17] in his original work, such as ferrion [3, 6] and manganese [21, 22]. The main requirements needed of the metal catalyst are that it is capable of a one electron transfer, and the reduction/oxidation is reversible [23]. A formal reduction potential range is derived using the formal reduction potenials of cerium and ferrion, ∼1.1 V and ∼ 1.44 V, respectively [24]. Therefore, a potential catalyst candidate should have a reduction potential within this range. One such catalyst is tris(2-2'-bipyridine)ruthenium(II) chloride, Ru(bpy)$_3^{2+}$, which has become widely used due to the photosensitivity of the complex. In 1973, Demas and Diemente reported that Ru(bpy)$_3^{2+}$ is highly luminescent in aqueous solutions, emitting a bright orange glow when excited by UV light [23]. Additionally, work with the catalyst by Gáspár et al. demonstrated Ru(bpy)$_3^{2+}$ is excitable using blue light [25]. Additional studies reported that ruthenium catalyzed BZ solutions, exposed to 450 nm light pulses, experienced both photoinhibtion and photoinduction of oscillations [16, 25–27]. This result suggests that there are two channels for the photochemistry, one which is excitatory [28] and the other inhibitory [26]. The first step in the mechanisms of both channels involves the excitation of the ruthenium catalyst by a photon:

$$Ru(II) + hv \rightarrow Ru(II)^*. \tag{2.13}$$

In the excitatory channel, the excited catalyst then reacts with bromate producing the radical $BrO_2^{\bullet}$. This radical quickly reacts with the catalyst that is still in the ground state to produce the autocatalytic species $HBrO_2$, Eqs. (2.14) and (2.15) [26, 27, 29–32].

$$Ru(II)^* + BrO_3^- + 2H^+ \rightarrow BrO_2^{\bullet} + Ru(III) + H_2O \tag{2.14}$$

$$BrO_2^{\bullet} + Ru(II) + H^+ \rightarrow Ru(III) + HBrO_2 \tag{2.15}$$

The additional bromous acid will consume bromide ions, which causes the bromide ion concentration to fall below the critical concentration at a faster rate, Eq. (2.3), and the oscillator to fire earlier.

The inhibitory channel also begins with the excitation of the metal catalyst with a photon. The excited catalyst is oxidized by bromomalonic acid (BrMA) and produces free bromide ions, Eq. (2.16). The oxidized catalyst can then react with more bromomalonic acid and produce more free bromide ions, Eq. (2.17) [26, 33–35].

$$Ru(II)^* + BrMA \rightarrow Ru(III) + Br^- + products \tag{2.16}$$

$$Ru(III) + BrMA \rightarrow Ru(II) + Br^- + products \tag{2.17}$$

The liberated bromide ions increase the time it takes to reach the critical concentration and suppress the autocatalytic production of bromous acid. The initial concentrations of reactants directly affect the prominence of a channel. The excitatory channel is dominate at high levels of bromate and low levels of bromomalonic acid. The inhibitory channel is more prominent at low levels of bromate and high levels of bromomalonic acid. At intermediate levels of reactants, both channels may be involved [16].

2.5 Computational Models of BZ Reaction

Computational models have become a powerful tool in modern scientific studies across many fields. Models allow questions and hypotheses to be explored that can be difficult to explore experimentally and can be either simplistic or detailed representations of the system. Modeling a chemical mechanism, even complex schemes such as the BZ reaction, is accomplished by using the necessary rate equations and transport processes involved in the reaction. This method of modeling is justified as the state variables are normally the concentrations of the significant species in a chemical system [19]. A computational model based on the FKN was developed by Richard Field and Richard Noyes in 1974 at the University of Oregon, called the Oregonator [2]. The Oregonator consists of five coupled elementary steps and three variable species derived from simplifying the FKN model. There have been several variants developed since the publication of the original Oregonater [6, 34, 36–38]. These modified models help explore and understand observed behaviors in the BZ system. There are two different models that will be discussed in this section: first, a four-variable model developed by Kádár et al. [26] that includes a variable representing bromomalonic acid and photosensitive terms [26, 34], and second, a model developed by Zhabotinsky, Buchholtz, Kiyatkin, and Epstein used to describe the modes of oscillations and wave propagation in a system with a relatively high oxidized/reduced ratio, called the ZBKE model [6].

2.5.1 Four-Variable Oregonator

The original Oregonator model proposed by Richard Field and Richard Noyes in 1974 was a three-variable system that was able to describe the chemical dynamics of the BZ reaction [1]. The Oregonator consists of five irreversible steps, Eqs. (2.18)-(2.22):

$$A + Y \xrightarrow{k_1} X + P, \tag{2.18}$$

$$X + Y \xrightarrow{k_2} 2P, \tag{2.19}$$

$$A + X \xrightarrow{k_3} 2X + Z, \tag{2.20}$$

$$2X \xrightarrow{k_4} A + P, \tag{2.21}$$

$$Z \xrightarrow{k_5} fY, \tag{2.22}$$

where X $\equiv$ $HBrO_2$, Y $\equiv$ Br^-, and Z $\equiv$ oxidized metal catalyst are the variables. Bromate is considered to be in excess and its concentration constant, and therefore it is represented as a parameter A $\equiv$ BrO_3^-. The concentration of H^+ is contained within the rate constants and is not shown explicitly. The product P $\equiv$ HOBr, which is needed to brominate the organic substrate, is not included in the rate equations. The stoichiometric factor, *f*, is introduced to control the amount of bromide ions created during Process C [2, 4]. This model was an important development because it could generate limit-cycle oscillations, which are characterized by a constant period. Figure 2.1 shows oscillations in the variables X, Y, and Z through time and the limit cycles produced using the three-variable Oregonator.

The original Oregonator cannot account for the photochemical production of bromide ions or bromous acid when using a photosensitive catalyst. The production of bromide ions from bromomalonic acid acts as an inhibitory species delaying the firing of the oscillation. Production of bromous acid from bromate, the autocatalytic species in the BZ reaction, will cause the system to fire earlier than the natural period. To account for these processes, a modification to the Oregonator was developed. In 2000, building on the earlier work of Kádár et al. [26], Amemiya et al. showed how this could be accomplished with the addition of a fourth variable to the Oregonator, V, equivalent to BrMA. This allowed the photo-production of bromide ions and bromous acid to be explicitly included in the model Eqs. (2.23)-(2.26) [34] :

$$V \xrightarrow{k_6} Products, \tag{2.23}$$

$$G \underset{k_{-L0}}{\overset{k_{L0}}{\rightleftharpoons}} E, \tag{2.24}$$

$$E + V + H^+ \xrightarrow{k_{L1}} Y + Z, \tag{2.25}$$

$$E + A + 2H \xrightarrow{k_{L2}} X + 2Z, \tag{2.26}$$

where V $\equiv$ BrMA, G $\equiv$ Ru(bpy)$_3^{2+}$, and E $\equiv$ Ru(bpy)$_3^{2+*}$. At a constant light intensity, the excitation of Ru(bpy)$_3^{2+}$ is proportional to the light flux, Φ, and the reverse reaction is assumed to undergo a 1^{st} order quenching process Eq. (2.24). Therefore, the concentration of E is assumed to be constant [26, 34]. A steady state approximation of E can be made using Eqs. (2.24)-(2.26)

$$E \approx \frac{\Phi}{k_{L1}\frac{k_{-L0}}{k_{L1}} + HV + \frac{k_{L2}}{k_{L1}}H^2A}. \tag{2.27}$$

Using this approximation and substituting it into the rate equations for Eqs. (2.25) and (2.26)

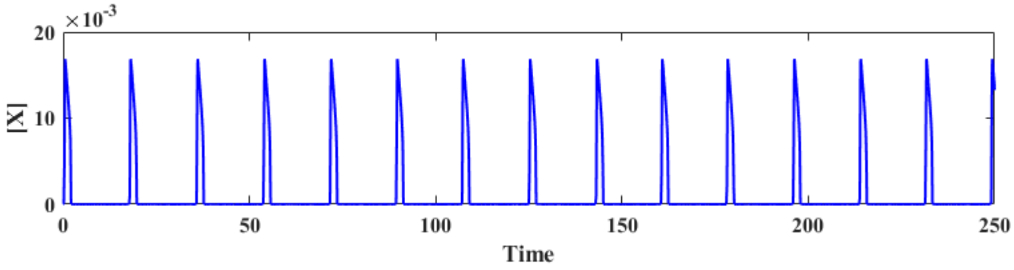

(a) Oscillations in the variable X

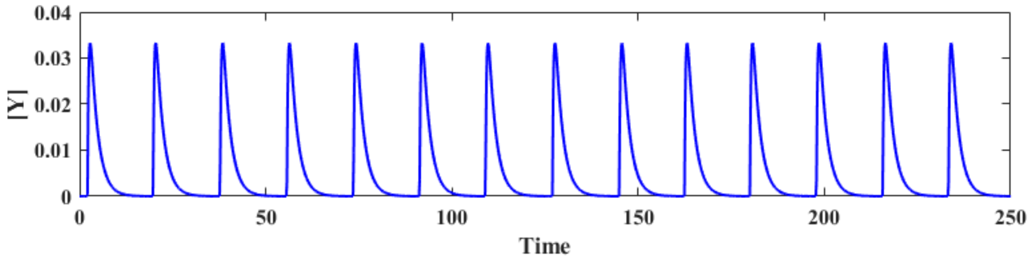

(b) Oscillations in the variable Y

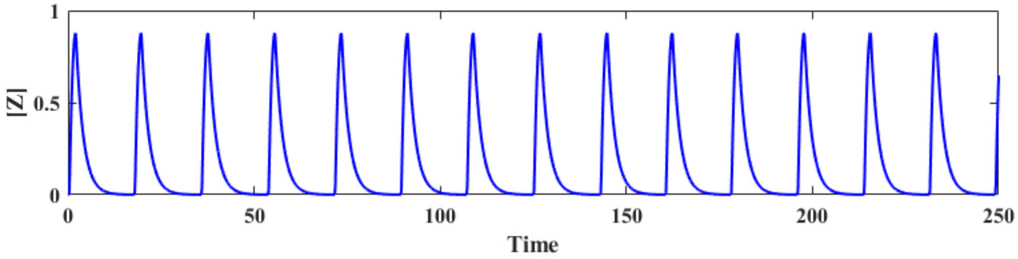

(c) Oscillations in the variable Z (Normalized)

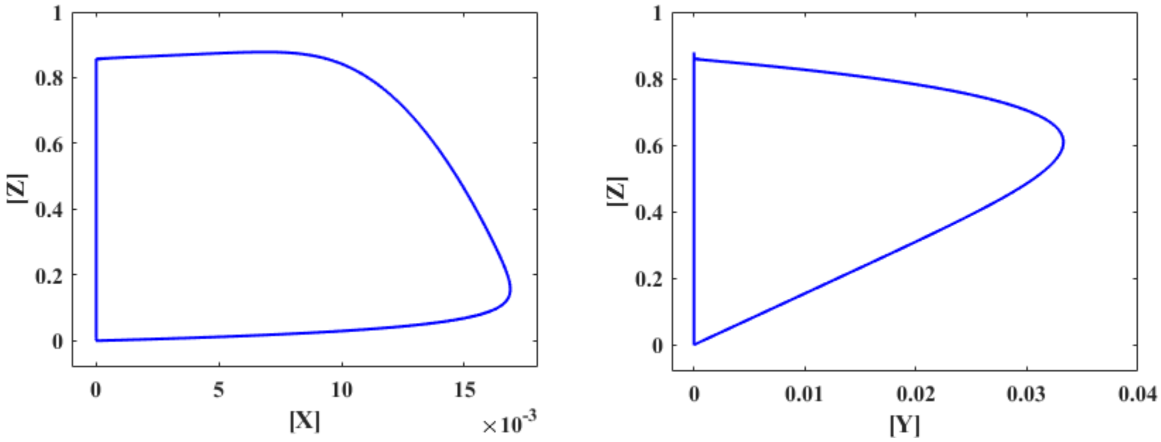

(d) Limit cycles of the variables Z vs. X

(e) Limit cycles of the variables Z vs. Y

Figure 2.1. (a) Time series of the autocatalytic species X, (b) the inhibitory species Y, and (c) the oxidized state of the catalyst Z using the 3-variable Oregonator. Figures (d) and (e) are showing limit cycles of the variables X vs. Z and Y vs. Z, respectively, and the typical concentrations of each variable with time.

yields:

$$r_{L1} = \frac{HV\Phi}{\frac{k_{-L0}}{k_{L1}} + HV + \frac{k_{L2}}{k_{L1}}H^2A} \equiv p_1(V)\Phi, \tag{2.28}$$

$$r_{L2} = \frac{\frac{k_{L2}}{k_{L2}}H^2A\Phi}{\frac{k_{-L0}}{k_{L1}} + HV + \frac{k_{L2}}{k_{L1}}H^2A} \equiv p_2(V)\Phi. \tag{2.29}$$

With the addition of these processes and approximations to the Oregonator, the differential equations for a photo-sensitive model can be written as follows, Eqs. (2.30)-(2.33):

$$\frac{dx}{dt} = k_1AY - k_2XY + k_3AX - 2k_4X^2 + p_2(V)\Phi, \tag{2.30}$$

$$\frac{dy}{dt} = -k_1AY - k_2XY + fk_3Z + p_1(V)\Phi, \tag{2.31}$$

$$\frac{dz}{dt} = 2k_3AX - k_5Z + (p_1(V) + 2p_2(V))\Phi, \tag{2.32}$$

$$\frac{dv}{dt} = k_1AY + 2k_2XY + k_4X^2 - k_6V - p_1(V)\Phi. \tag{2.33}$$

The model can not only reproduce limit-cycle oscillations generated in the original Oregonator, but photoinduced behaviors such as photoinhibiton, photoinduction, small amplitude oscillations, and mixed-mode behaviors, Fig. 2.2 [34]. Simulations produce good qualitatively agreement with experiments involving the ruthenium-catalyzed BZ system [31, 39].

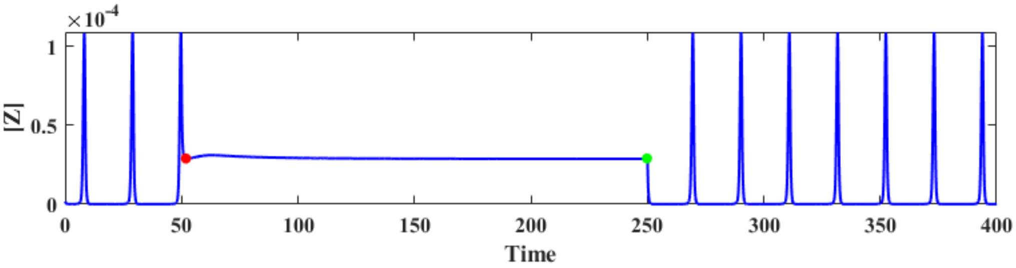

(a) Photoinhibition of oscillations

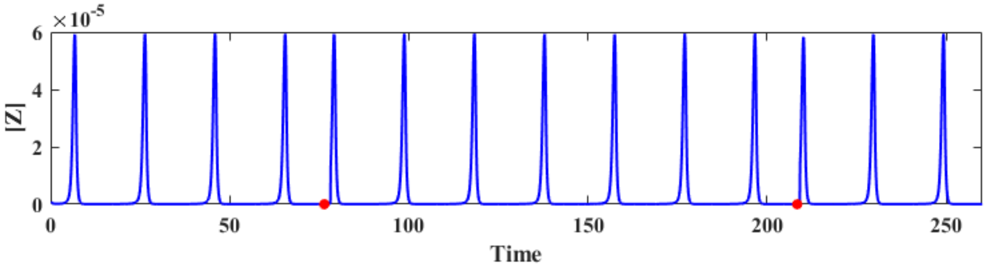

(b) Photoinduction of oscillations

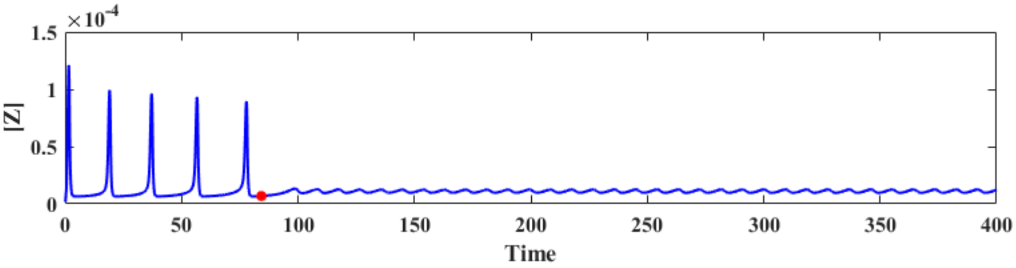

(c) Photoinduced small amplitude oscillations

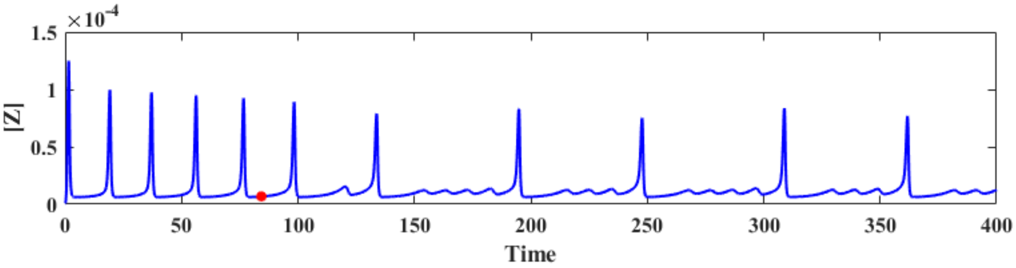

(d) Photoinduced mixed-mode oscillations

Figure 2.2. (a) Time series showing photoinhibition of oscillations at time 75. The parameter Φ was set to 1.0×10^{-5}, red dot, and was returned to zero at time 125, green dot. The system ceased oscillating and was put into a photo-induced steady state during the simulated light pulse. (b) Simulated photoinduction of bromous acid. A short simulated light pulse at times 75 and 210 for 2 seconds at a $\Phi = 1.3 \times 10^{-5}$ was applied. After each pulse the oscillator fired with a reduced period of 14 seconds compared to the natural period of 20 sec. (c) Photoinduced small amplitude oscillations, at time 48 the parameter Φ was set to 1.0×10^{-5} for the duration of the simulation. (d) Photoinduced mixed-mode oscillations, at time 52 the parameter Φ was set to 1.0×10^{-5} for the duration of the simulation.

2.5.2 The ZBKE Mechanism and Model

In 1993, Zhabotinsky, Buchholtz, Kiayatkin, and Epstein proposed a reaction scheme based on the FKN mechanism, known as the ZBKE model [6]. Zhabotinsky et al. noted that current mathematical models did not correctly describe the modes of oscillation when the oxidized form of the catalyst occupies a significant portion of the cycle [6]. This reaction mechanism includes a more detailed description in the chemistry of the organic species and HBrO_2^+, shown in Eqs. (R1)-(RA-2).

$$HOBr + Br^- + H^+ \rightleftharpoons Br_2 + H_2O \tag{R1}$$

$$HBrO_2 + Br^- + H^+ \rightleftharpoons 2HOBr \tag{R2}$$

$$HBrO_3 + Br^- + H^+ \rightleftharpoons HBrO_2 + HOBr \tag{R3}$$

$$2HBrO_2 \rightleftharpoons HBrO_3 + HOBr \tag{sR4a}$$

$$H^+ + HBrO_2 \rightleftharpoons H_2BrO_2^+ \tag{R4b}$$

$$HBrO_2 + H_2BrO_2^+ \rightleftharpoons HBrO_3 + HOBr + H^+ \tag{R4c}$$

$$H^+ + BrO_3^- \rightleftharpoons HBrO_3 \tag{R5a}$$

$$H^+ + HBrO_3 + HBrO_2 \rightleftharpoons HBrO_2^+ + BrO_2^\bullet + H_2O \tag{R5b}$$

$$H^+ + BrO_2^\bullet \rightleftharpoons HBrO_2^+ \tag{R5c}$$

$$M^n + HBrO_2^+ \rightleftharpoons M^{n+1} + HBrO_2 \tag{R6}$$

$$M^{n+1} + CHBr(COOH)_2 \rightleftharpoons M^n + CBr(COOH)_2^\bullet + H^+ \tag{R7}$$

$$H_2O + CBr(COOH)_2^\bullet \longrightarrow Br^- + H^+ + COH(COOH)_2^\bullet \tag{R8}$$

$$H_2O + CHBr(COOH)_2 \longrightarrow Br^- + H^+ + CHOH(COOH)_2 \tag{R9}$$

$$2COH(COOH)_2^\bullet \longrightarrow CHOH(COOH)_2 + CO(COOH)_2 \tag{R10}$$

$$COH(COOH)_2^\bullet + CBr(COOH)_2^\bullet \longrightarrow CHBr(COOH)_2 + CO(COOH)_2 \tag{R11}$$

$$HOBr + CHBr(COOH)_2 \longrightarrow CBr2(COOH)_2 + H_2O \tag{RA-1}$$

$$Br_2 + CHBr(COOH)_2 \longrightarrow CBr_2(COOH)_2 + H^+ + Br^- \tag{RA-2}$$

Here, M^n and M^{n+1} represent the reduced and oxidized states of the metal catalyst, respectively. We assume that the reactions shown in Eqs. (RA-1) and (RA-2) are fast enough that all other reactions of HOBr and Br_2 can be neglected and $CBr_2(COOH)_2$, $CHOH(COOH)_2$, and $CO(COOH)_2$ can be treated as final products [6].

The mathematical model of the ZBKE mechanism is written using the essential processes and key intermediates [6]:

$$\frac{dX}{dt} = -k_2h_0XY + k_3h_oXY - 2k_4^*X^2 - k_5h_0AX + k_{-5}U^2 + k_6U(C-Z) - k_{-6}XZ, \tag{2.34}$$

$$\frac{dY}{dt} = -k_2h_0XY - k_3hoAY + k_8^{'}R_1 + k_9B, \tag{2.35}$$

$$\frac{dU}{dt} = 2k_5h_0AX - 2k_{-5}U^2 - k_6U(C-Z) + k_{-6}XZ, \tag{2.36}$$

$$\frac{dZ}{dt} = k_6U(C-Z) - k_{-6}XZ - k_7BZ + k_{-7}h_0R_1(C-Z), \tag{2.37}$$

$$\frac{dR_1}{dt} = k_7BZ - k_{-7}h_0R_1(C-Z) - k_8^{'}R_1 - k_{11}R_1R_2, \tag{2.38}$$

$$\frac{dR_2}{dt} = k_8^{'}R_1 - 2k_{10}R_2^2 - k_{11}R_1R_2, \tag{2.39}$$

where $X \equiv [HBrO_2]$, $Y \equiv [Br^-]$, $U \equiv [HBrO_2{}^+]$, $Z \equiv [M^{n+1}]$, $R_1 \equiv [CBr(COOH)_2{}^\bullet]$, $R_2 \equiv [COH(COOH)_2{}^\bullet]$, $A \equiv [HBrO_3] \equiv h_0[NaBrO_3]_0/(0.2+h_0)$, $B \equiv [CHBr(COOH)_2]$, $C \equiv Z + [M^n]$, h_0 = Hammet acidity function, $k_4{}^* = k_4(1+0.87h_0)$, and k_{-5} is substituted for $(k_{-5b}k_{-5c})/(k_{5c}h_0)$. The reaction shown in Eq. (2.39) can be neglected, assuming very fast radical recombination of Eqs. (R10) and (R11). Using quasi-steady state approximation, the equation for R_1 can be rewritten as:

$$\frac{dR_1}{dt} = k_7BZ - k_{-7}h_oR_1(C-Z) - \frac{k_8^{'}R_1}{q(R_1}, \tag{2.40}$$

where

$$\frac{1}{q(R_1)} = 1 - \frac{k_{11}^2R_1}{4k_8^{'}k_{10}}\left(1 - \left(1 + \frac{8k_8^{'}k_{10}}{k_{11}^2R_1}\right)^{\frac{1}{2}}\right). \tag{2.41}$$

The parameter q is introduced to adjust the model to experimental observations based on reactions R10 and R11. When reaction R10 is much faster than R11, the product $q(R_1) = 1$. When R11 is much faster than R10, then the product $q(R_1) = 0.5$. To further simplify the parameter, q is used in place of q(R_1) and $k_8 = k'_8/q$ [6].

If we assume [CBr(COOH)$_2$] is a fast variable and treat $HBrO_2^+$ as a steady state variable, U_{SS}, a reduced system can be written using three-variables:

$$\frac{dX}{dt} = \frac{-k_2X + k_3A}{k_2X + k_3A}(qk_7k_8G_1 + k_9B) - 2k_4^*X^2 - k_5h_oAX + k_{-5}U_{ss}^2(C - Z) - k_{-6}XZ, \quad (2.42)$$

$$\frac{dY}{dt} = -k_2h_oXY - k_3h_oAY + qG_2 + k_9B, \quad (2.43)$$

$$\frac{dZ}{dt} = k_6U_{ss}(C - Z) - k_{-6}XZ - G_2, \quad (2.44)$$

where

$$U_{ss} = \frac{k_6(C - Z)}{4k_{-5}} + \sqrt{k_6^2(C - Z)^2 + (16K_5k_{-5}h_oAX + 8k_{-5}k_{-6}XZ)}, \quad (2.45)$$

$$G_1 = \frac{BZ}{k_8 + k_{-7}h_oR_1(C - Z)}, \quad (2.46)$$

and

$$G_2 = \frac{k_7k_8BZ}{k_8 + k_{-7}h_o(C - Z)}. \quad (2.47)$$

The concentrations of bromate, A, and sulfuric acid, h_o, are considered to be in large excess and treated as parameters with a constant value. By using appropriate scaling, a nondimensional ZBKE model of the ferrion catalyzed BZ reaction can yield qualitative comparisons with experiments [6, 13, 16, 40, 41] and is described by the differential Eqs. (2.48)-(2.50). The scaled variables and parameters are shown in Table 2.1.

$$\frac{dx}{d\tau} = \frac{1}{\varepsilon_1}\left(\varphi - x^2 + x + \varepsilon_2\gamma u_{ss}^2(1 - z) + \delta xz + \frac{\mu - x}{\mu - z}\left(\frac{q\alpha z}{\varepsilon_3 + 1 - z}\right) + \beta\right) \quad (2.48)$$

$$\frac{dy}{d\tau} = \frac{1}{\varepsilon_4}\left(-xy - \mu y + q\frac{\alpha z}{\varepsilon_3 + 1 - z} + \beta\right) \quad (2.49)$$

$$\frac{dz}{d\tau} = 2\varphi + u_{ss}(1 - z) - \delta xz - \frac{\alpha z}{\varepsilon_3 + 1 - z} \quad (2.50)$$

This model produces a significant distribution of natural periods by varying the parameter q in contrast to the Oregantor model, with lower values yielding faster periods. This is an important feature when investigating populations of oscillators with large heterogeneity. To account for

Table 2.1. Variable and Parameter Scaling for ZBKE Model [6, 13]

Parameter	Scaling	Variable	Scaling
ε_1	$k_5h_oA/2k_4C$	X	$k_5h_oAx/2k_4$
β	$2k_4k_9B/(k_5h_oA)^2$	Y	k_5Ay/k_2
ε_2	$(k_5h_oA)^2/2k_4k_6C$	Z	Cz
μ	$2k_3k_4B/k_2k_5h_o$	U	$(k_5h_oA)^2u/2k_4k_6C$
ε_3	$k_8/k_{-7}h_oC$	t	$2k_4C\tau/(k_5h_oA)^2$
γ	k_{-5}/k_6		
ε_4	k_5A/k_2C		
δ	$k_{-6}C/k_5h_oA$		
α	$2k_4k_7k_8B/k_4{}^2k_{-7}h_o{}^3A^2$		
k	$2k_4CK/(k_5h_oA)^2$		

the use of the $Ru(bpy)_3^{2+}$ catalyst, further modifications can be made to the model to include the photo-production of bromous acid and bromide ions [13, 26, 35]. The influence of these photo-chemical processes can be included in the dynamics of the ZBKE model by the addition of a parameter representing the light flux, ϕ, to Eqs. (2.48)-(2.50) [35].

$$\frac{dx}{d\tau} = \frac{1}{\varepsilon_1}\left(\phi - \varphi - x^2 + x + \varepsilon_2\gamma u_{ss}^2(1-z) + \delta xz + \frac{\mu - x}{\mu - z}\left(\frac{q\alpha z}{\varepsilon_3 + 1 - z}\right) + \beta\right) \tag{2.51}$$

$$\frac{dy}{d\tau} = \frac{1}{\varepsilon_4}\left(\phi - xy - \mu y + q\frac{\alpha z}{\varepsilon_3 + 1 - z} + \beta\right) \tag{2.52}$$

$$\frac{dz}{d\tau} = \phi + 2\varphi + u_{ss}(1-z) - \delta xz - \frac{\alpha z}{\varepsilon_3 + 1 - z} \tag{2.53}$$

For a purely excitatory system, ϕ will not appear in Eq. (2.51), while for a purely inhibitory system, ϕ will not appear in Eq. (2.53). However, this modification is limited to either a purely excitatory or inhibitory system, which cannot describe all the observed behaviors in experiments. The introduction of a tunable parameter, α_o, can account for the photo-chemical processes by specifying a weight to the excitatory and inhibitory channels of the $Ru(bpy)_3^{2+}$ catalyzed BZ reaction. The three-variable-photosensitive ZBKE model can now be written as:

$$\frac{dx}{d\tau} = \frac{1}{\varepsilon_1}\left(\alpha_o\phi - \varphi - x^2 + x + \varepsilon_2\gamma u_{ss}^2(1-z) + \delta xz + \frac{\mu - x}{\mu - z}\left(\frac{q\alpha z}{\varepsilon_3 + 1 - z}\right) + \beta\right), \tag{2.54}$$

$$\frac{dy}{d\tau} = \frac{1}{\varepsilon_4}\left((1-\alpha_o)\phi - xy - \mu y + q\frac{\alpha z}{\varepsilon_3 + 1 - z} + \beta\right), \tag{2.55}$$

$$\frac{dz}{d\tau} = (1+\alpha_o)\phi + 2\varphi + u_{ss}(1-z) - \delta xz - \frac{\alpha z}{\varepsilon_3 + 1 - z}. \tag{2.56}$$

Figure 2.3 shows the time series for the dimensionless variables x, y, and z, and limit cycles showing z vs. x and z vs. y for a simulation using the three-variable-photosensitive ZBKE model.

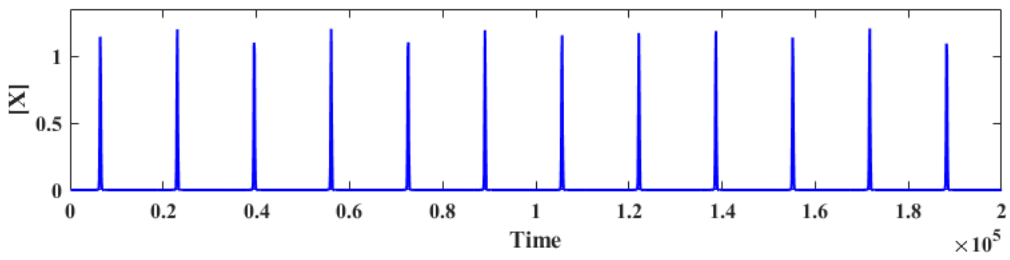

(a) Oscillations in the variable X

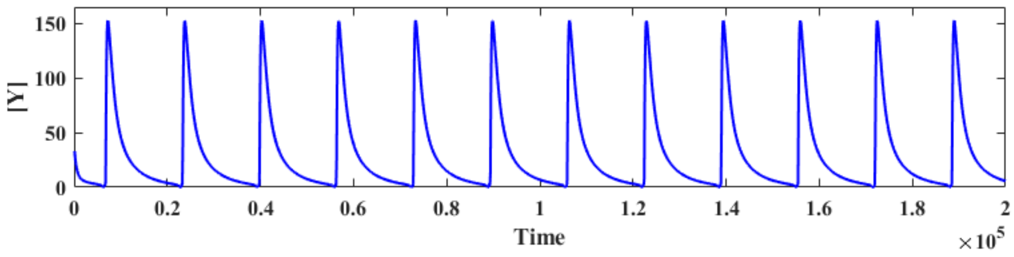

(b) Oscillations in the variable Y

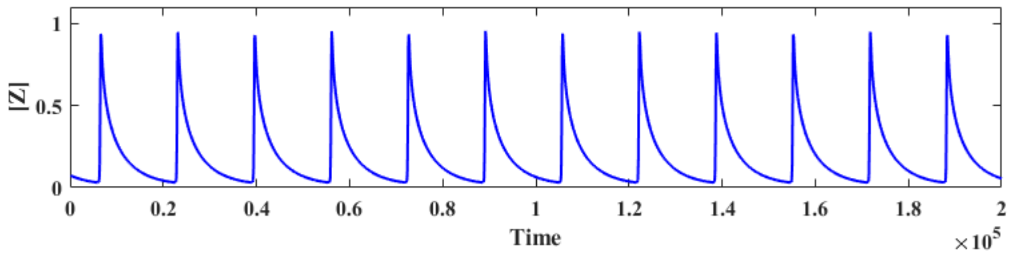

(c) Oscillations in the variable Z

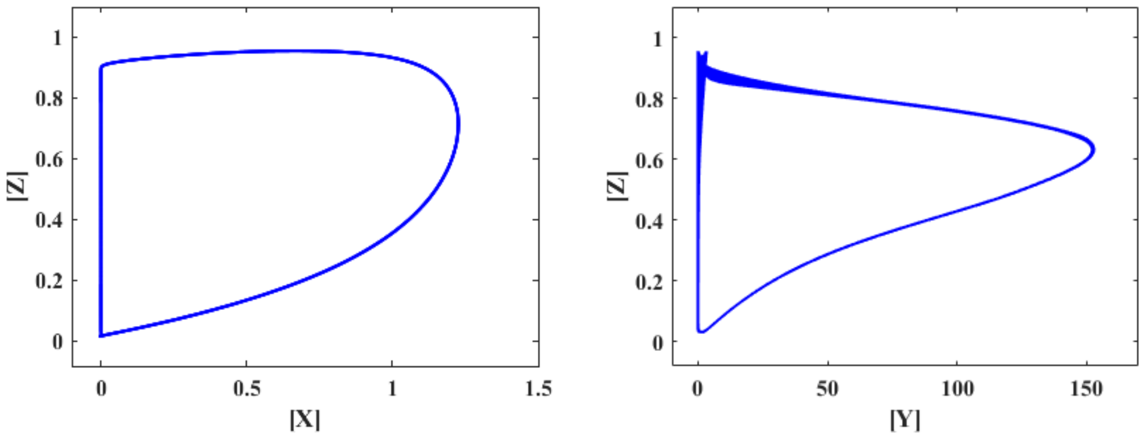

(d) Limit cycles of Z vs. X

(e) Limit cycles of Z vs. Y

Figure 2.3. (a) Time series of the autocatalytic species X, (b) the inhibitory species Y, and (c) the oxidized state of the catalyst Z using the 3-variable ZBKE model. Figures (d) and (e) are showing phase plots of the variables X vs. Z and Y vs. Z, respectively, illustrating the typical concentrations of each variable with time.

2.6 Phase Response Curves

The photo-sensitive Ru(bpy)$_3^{2+}$ catalyst, used in the BZ reaction, can be excited by exposure to 450 nm light. The use of brief light pulses to perturb an oscillator can either delay the phase of an oscillation, an inhibitory response, Fig. 2.4(a) [26, 33–35], advance the phase, an excitatory response, Fig. 2.4(b), of an oscillation [26, 27, 29–32], or have no effect on the oscillation. In Fig. 2.4(a), the oscillator was phase delayed as the natural period, T, equals 65 seconds, and after perturbation the perturbed period, T$^{'}$, is equal to 102 seconds. In Fig. 2.4(b), the oscillator has a natural period T of 109 seconds and after perturbation has a T$^{'}$ equal to 73 seconds, a phase advance. When studying networks of oscillators, a method of understanding and predicting how an oscillator responses to signals from coupled partner(s) is needed. This is done by construction of a phase response curve, PRC, which shows the change in the phase of an oscillator, $\Delta\gamma$, due to a perturbation at a particular phase, γ, in its cycle [16, 42, 43]. Phase response curves have been used to predict behaviors and stability in neural networks [44, 45] as well as networks of chemical oscillators [16, 43]. This powerful tool can be used to help understand an individual oscillator's dynamics in a network and that oscillator's influence on

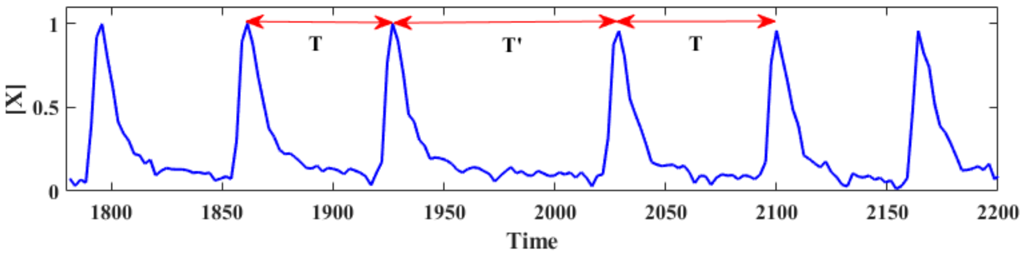

(a) Phase delay

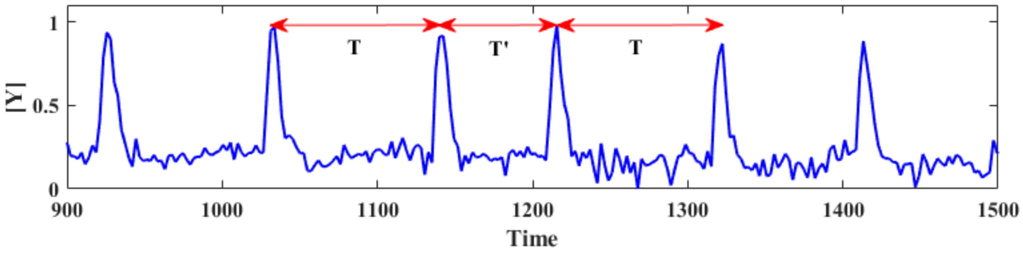

(b) Phase advancement

Figure 2.4. Time series of PRC experiments showing (a) phase delay, where T < T$^{'}$ and (b) phase advancement, where T > T$^{'}$. Here, T is the natural or unperturbed period and T$^{'}$ is the perturbed period.

the overall network. Both the initial conditions of the BZ solution and the magnitude of the perturbation are factors in the overall shape of the PRC [45]. Therefore, in this section we experimentally investigate the photo-chemical responses of discrete oscillators from short light pulses immersed in either an excitatory or inhibitory catalyst-free BZ solution [16]. In addition to this, computational methods will be used to explore the role of coupling strength in excitatory and inhibitory systems on the shape of a PRC using a three-variable ZBKE model.

2.6.1 Experimental Setup

Instrumentation

The experimental setup consists of a laser-diode projector modifed with a plano lens and a 440-460 nm band pass filter, a beam splitter, CCD video camera, computer, and reactor. Light from the modified projector is reflected down onto the reactor, which is then reflected back up to the CCD camera postioned directly above. Recorded images are processed and saved as a gray-scaled image by the computer. The computer processes the images and calculates the light intensity and pattern transmitted by the modified projector using a custom algorithm. In PRC experiments, the algorithm will perturb the oscillators with a single $1.2\,\mathrm{mW\,cm^{-2}}$ pulse for 1 second. The setup is illustrated in Fig. 2.5.

Tris(2-2'-bipyridine)Ruthenium(II) Chloride Loaded Beads

Individual chemical oscillators are produced by loading cation exchange beads (Dowex 50-100 mesh, radius 150-200 µm) with the photosensitive tris(2,2'-biyridine)ruthenium(II) chloride hexahydrate, $\mathrm{Ru(bpy)_3^{2+}}$. A $\mathrm{Ru(bpy)_3^{2+}}$ catalyst solution is made by dissolving enough complex to make a 15 mM solution using deionized water. Three grams of the ion exchange beads are placed in a beaker with a stir bar and 9 ml of deionized water. While being slowly stirred, the desired volume of the 15 mM catalyst solution is added dropwise to the beaker containing the beads and water, along with enough water to bring the total volume to 10 ml. The solution containing the beads is allowed to stir for 24 hours in a dark environment. Finally, the beads are filtered and washed with deionized water and air dried for at least 24 hours. The final concentration of catalyst loaded onto the cation exchange beads is either $2.5 \times 10^{-6}\,\mathrm{mol\,g^{-1}}$ or $5.0 \times 10^{-6}\,\mathrm{mol\,g^{-1}}$ resin, labeled as the peripheral and hub oscillators, respectively. This differ-

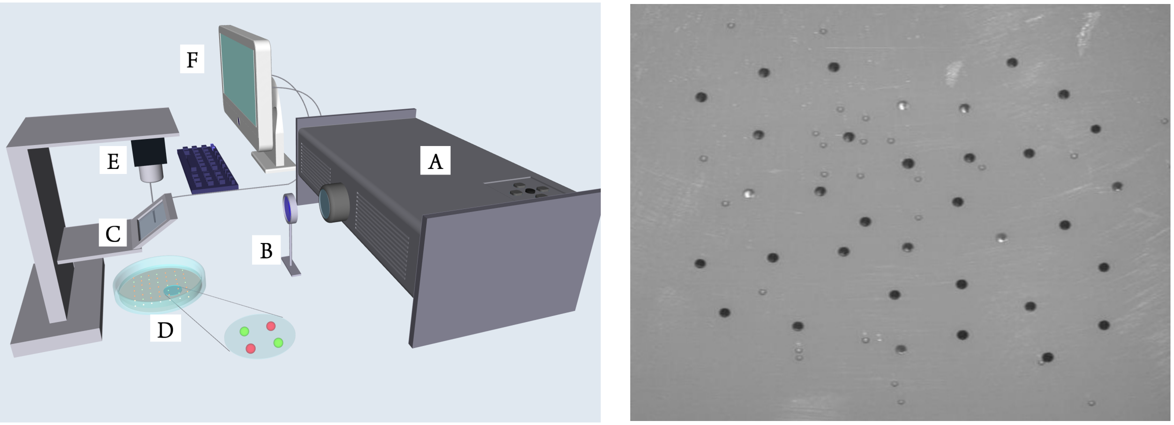

(a) Experimental setup

(b) Catalyst loaded beads

Figure 2.5. (a) Experimental setup used for all experiments. The projector (A) transmits collimated light through a 440-460 nm (blue) band bass filter (B) to the beam splitter (C). The light is reflected down to the reactor (D) and back up to the CCD camera (E) positioned above. The image is processed by the computer (F) and the proper feedback is calculated and applied by the modified projector. (b) Image of beads submerged in a catalyst-free BZ solution recorded by the CCD camera. The catalyst on the beads that appears dark is in the reduced state. The catalyst on the beads that appears bright is in the oxidized state, as they are transparent at 450 nm.

ence in the ruthenium concentrations produces a period variation between hub and peripheral oscillators of ∼30%. The peripheral oscillators have a natural period range of 80-100 seconds, while the hub oscillators have a natural period range of 50-70 seconds.

Catalyst-Free BZ Solutions for PRC Experiments

For the PRC experiments, two different catalyst-free BZ solutions are used, the excitatory formula and the inhibitory formula. Both solutions are made from stock solutions of 2.0 M sodium bromate, $NaBrO_3$, 2.0 M sodium bromide, NaBr, and 6.0 M sulfuric acid, H_2SO_4, obtained from Fisher Scientific. Malonic acid, MA, from Acros Organics is added to the excitatory and inhibitory solutions as a dry salt. The excitatory formula has initial concentrations of $[NaBrO_3] = 0.640$ M, $[H_2SO_2] = 0.780$ M, $[NaBr] = 0.060$ M and $[MA] = 0.096$. The inhibitory formula varies only by a change in the bromate concentration $[NaBrO_3] = 0.320$ M. The initial NaBr is consumed via an enol reaction that brominates the α-carbon of the malonic acid, yielding an effective bromomalonic acid concentration of 0.090 M for both solutions.

PRC Experimental Procedure

A catalyst-free BZ solution is prepared and 30 ml are transferred to the reactor containing catalyst loaded beads. The reactor is placed in the experimental setup and the beads are arranged to have at least two diameters space between them. This space ensures that no diffusive coupling is affecting the periods of the oscillators. The beads are allowed to oscillate at a constant background intensity of $0.52\,\mathrm{mW\,cm^{-2}}$. Images of the beads are recorded every three seconds for the length of the experiment. Before the first 1.0 s light pulse is applied the beads are allowed to oscillate for 7 minutes, which allows them to settle into their natural period before perturbation. Additional 1 second light pulses are applied at predetermined times after the oscillators have completed at least three cycles between each pulse.

2.6.2 Experimental and Computational Results

In the experimental system, a PRC is constructed by perturbing discreet oscillators with a 1.0 s light pulse at arbitrary phases and then recording the time of the next firing. The phase of the oscillator, γ, at any time is given by:

$$\gamma(t) = \frac{2\pi(t - t_{peak})}{T}, \tag{2.57}$$

where t is the current time and t_{peak} is the time of the previous peak. The change in the phase of an oscillator, $\Delta\gamma$, is calculated by comparing the natural period, T, to the period of the perturbed cycle, T', Eq. (2.58) [16, 46, 47].

$$\Delta\gamma = \frac{2\pi(T - T')}{T} \tag{2.58}$$

An interval of at least three periods between the perturbations is used, allowing the oscillations to relax back to their natural periods.

Using the excitatory solution, both the hub Fig. 2.6(a) and peripheral Fig. 2.6(c), oscillators have a phase advancing region in the latter half of their cycle. Preceding this is a small phase delaying region. Very early in the cycles of both systems, they are refractory, and therefore the perturbation has a minimal impact. When placed in an inhibitory solution, both hub Fig, 2.6(b) and peripheral oscillators, Fig. 2.6(d), oscillators show only a phase delay and refractory regime. These results show that varying the initial concentrations of the catalyst-free BZ solution changes the predominance of the photo-chemical channels. They also show that the difference in the catalyst concentration has a minimal affect on the phase response of the oscillator in a given solution.

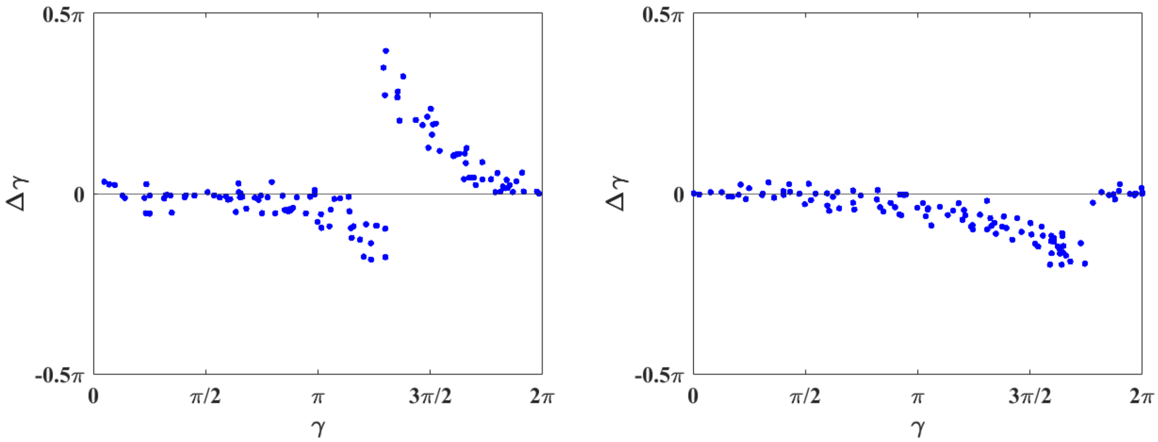

(a) Hub oscillators using excitatory solution (b) Hub oscillators using inhibitory solution

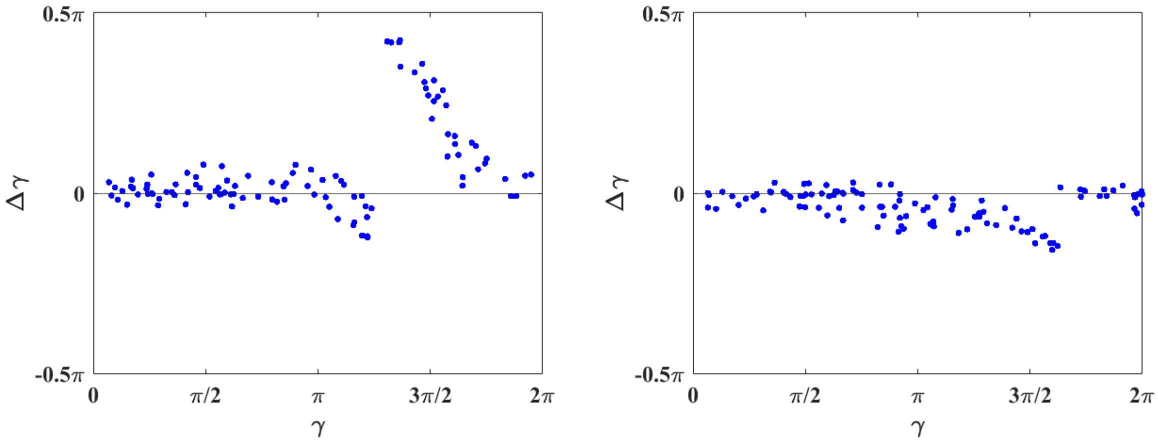

(c) Peripheral oscillators using excitatory solution (d) Peripheral oscillators using inhibitory solution

Figure 2.6. Experimentally constructed phase response curves using excitatory or inhibitory solutions for both hub and peripheral oscillators. (a) PRC for the hub oscillators in an excitatory catalyst-free solution showing both phase resetting and phase delaying regions. (b) PRC using inhibitory catalyst-free solution showing a phase delaying region for the hub oscillators. (c) PRC for the peripheral beads using excitatory catalyst-free solution and (d) inhibitory catalyst-free solution for the peripheral oscillators.

The PRCs for the model system are constructed in a similar manner to the experimental system using the three-variable photosensitive ZBKE mechanism. A given oscillator is briefly perturbed through a small change in the light intensity ϕ at a given phase and the impact on the time of the next firing is measured using Eq. (2.58). The resulting PRCs are for both the hub, Fig. 2.7 (a) and (b), and peripheral oscillators, Fig. 2.7 (c) and (d), for the cases of $\alpha = 1$ (a) and (b) and $\alpha = 0$ (c) and (d). The results are a good quantitative match to the experimental results. The excitatory pathway, $\alpha = 1$, showing a phase advancing region in the latter part of the oscillator's phase and a small inhibitory region preceded by a refractory region early in the phase, Fig. 2.7 (a) and (d). For $\alpha = 0$, the inhibitory pathway the oscillators only show a phase delaying region that is preceded by a large refractory region, Fig. 2.7(b) and (d). The variation in natural period of the oscillators had a minimal impact on the shape and slope of the PRCs, which is also in agreement with the experimental results.

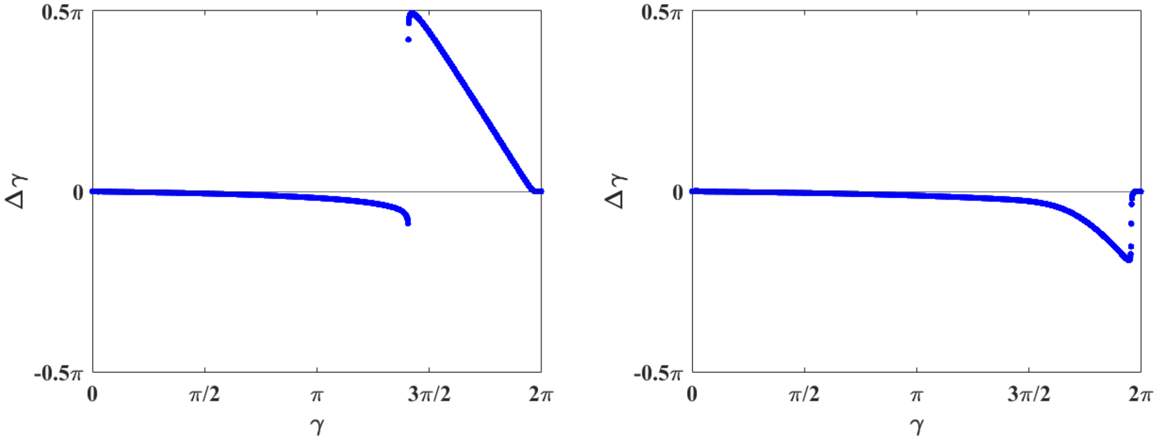

(a) Low q value in excitatory system

(b) Low q value in inhibitory system

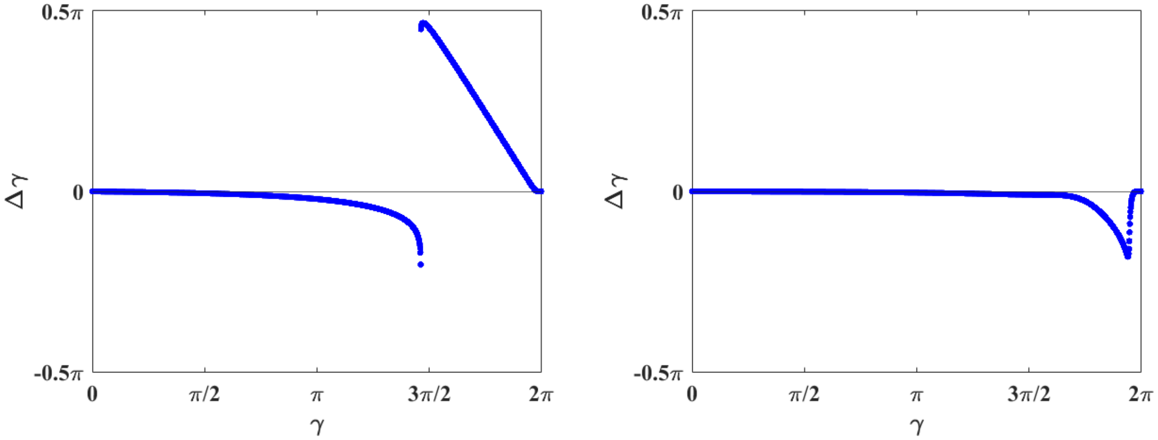

(c) High q value in excitatory system

(d) High q value in inhibitory system

Figure 2.7. Computational PRCs constructed using the three-variable-photosensitive ZBKE model. Figure 2.7(a) and (b) show the results for the hub oscillator using excitatory and inhibitory coupling, respectively. The peripheral oscillators are shown in (c) and (d), also using excitatory and inhibitory coupling, respectively.

The magnitude of the perturbation, P, also has an affect on the overall shape of the PRC by changing the slope and location of the response regions. This can be shown by constructing PRCs using the ZBKE model and varying the parameter P. In the inhibitory system, $\alpha = 0$, the magnitude of the perturbation P was varied from 0.18 to 0.88. In Fig. 2.8(a), the slope of the inhibitory regime becomes more negative. The refractory region earlier in the phase is also reduced in length. Therefore, as P is increased, the earlier in an oscillator's phase it can be delayed and to a greater extent. For the excitatory system, $\alpha = 1$, P was also varied from 0.18 to 0.88. Figure 2.8(b) shows as P was varied the slope of the excitatory region in the latter part phase does not change. However, it does extend to earlier phases down to π, at P $= 0.88$, in the cycle. The slope does not change because once the oscillator receives an excitatory signal it fires almost immediately and the phase is advanced to 2π. We can also see that the inhibitory region is reduced with minimal changes to the slope. These computational results demonstrate the impact of the magnitude of a perturbation on both systems.

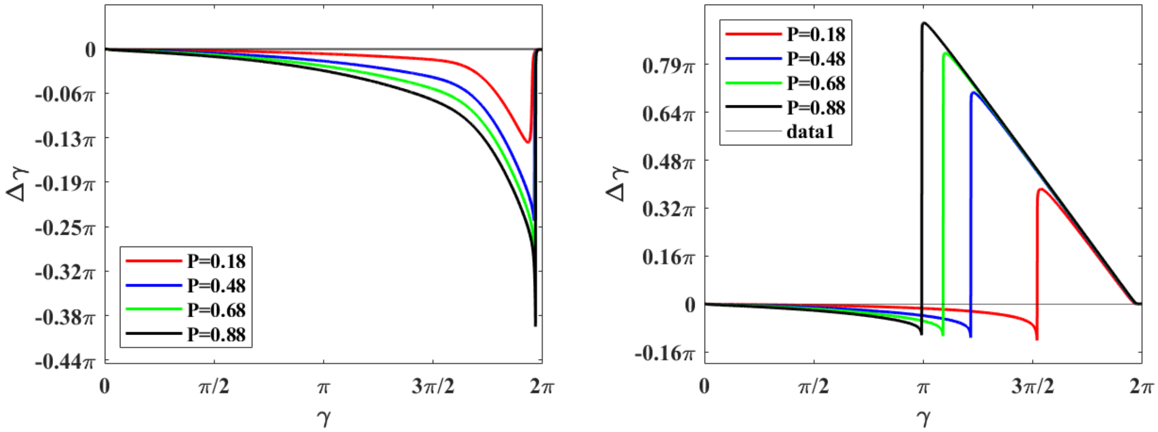

(a) Computational PRCs for the inhibitory system. (b) Computational PRCs for the excitatory system.

Figure 2.8. (a) Computational PRC of the inhibitory system and (b) excitatory system using the ZBKE model. The magnitudes of the perturbations was varied from 0.18 to 0.88.

References

1. R. J. Field, E. Körös, R. M. Noyes, *J. Amer. Chem. Soc.* **94**, 8649 (1972).
2. R. J. Field, R. M. Noyes, *J. Chem. Phys.* **60**, 1877 (1974).
3. A. M. Zhabotinsky, *Chaos* **1**, 379 (1991).
4. I. R. Epstien, K. Showalter, *J. Phys. Chem.* **100**, 13132 (1996).
5. I. R. Epstien, J. A. Pojman, *An Introduction to Nonlinear Chemical Dynamics: Oscillatoions, Waves, Patterns, and Chaos* (Oxford Univeristy Press, New York, New York, 1998).
6. A. M. Zhabotinsky, F. Buchholtz, A. B. Kiyatkin, I. R. Epstein, *J. Phys. Chem.* **97**, 7578 (1993).
7. J. Maselko, J. S. Reckley, K. Showalter, *J. Phys. Chem.* **93**, 2774 (1989).
8. A. N. Zaikin, A. M. Zhabotinsky, *Nature* **225**, 535 (1970).
9. R. A. Schmitz, K. R. Graziani, J. L. Hudson, *J. Chem. Phys.* **67**, 3040 (1977).
10. J. L. Hudson, J. C. Mankin, *J. Chem. Phys.* **74**, 6171 (1981).
11. F. Argoul, A. Arneodo, P. Richetti, J. C. Roux, H. L. Swinney, *Acc. Chem. Res.* **20**, 436 (1987).
12. V. Petrov, V. Gáspár, J. Masere, K. Showalter, *Nature* **361**, 240 (1993).
13. R. Toth, A. F. Taylor, M. R. Tinsley, *J. Phys. Chem. B* **110**, 10170 (2006).
14. S. Nkomo, M. R. Tinsley, K. Showalter, *Phys. Rev. Lett.* **110**, 244102 (2013).
15. S. Nkomo, M. R. Tinsley, K. Showalter, *Chaos* **26**, 094826 (2016).
16. D. Yengi, M. R. Tinsley, K. Showalter, *Chaos* **28**, 045114–1 (2018).

17. B. P. Belousov, presented at the Oscillations Traveling Waves Chemical Systems. Copyright (C) 2017 American Chemical Society (ACS). All Rights Reserved., p. 605.
18. A. T. Winfree, *J. Chem. Educ.* **61**, 661 (1984).
19. K. Showalter, I. R. Epstein, *Chaos* **25**, 097613 (2015).
20. R. K. Thauer, *Eur. J. of Biochem.* **176**, 497 (1988).
21. E. Kumpinsky, I. R. Epstein, *J. Phys. Chem.* **89**, 688 (1985).
22. N. B. Ganaie, G. M. Peerzada, *Int. J. Chem. Kinet.*, 343 (2013).
23. J. N. Demas, D. Diemente, *J. Chem. Educ.* **50**, 357 (1973).
24. G. F. Smith, F. P. Richter, *Phenanthroline and Substituted Phenanthroline Indicators* (The G. Fredrick Smith Chemical Co., Columbus, Ohio, 1944).
25. V. Gáspár, G. Bazsa, M. T. Beck, *Z. Phys. Chem. (Leipzig)* **264**, 43 (1993).
26. S. Kádár, T. Amemiya, K. Showalter, *J. Phys. Chem. A* **101**, 8200 (1997).
27. I. Hanazaki, Y. Mori, T. Sekiguchi, G. Rábai, *Physica D* **84**, 228 (1995).
28. H. J. Krug, L. Pohlmann, L. Kuhnert, *J. Phys. Chem.* **94**, 4862 (1990).
29. A. Kaminaga, I. Hanazaki, *J. Phys. Chem. A* **102**, 3307 (1998).
30. I. Hanazaki, *J. Phys. Chem.* **96**, 3307 (1992).
31. A. Kaminaga, Y. Mori, I. Hanazaki, *Chem. Phys. Lett.* **279**, 339 (1997).
32. Y. Mori, Y. Nakamichi, T. Sekiguchi, N. Okazaki, T. Matsumura, I. Hanazaki, *Chem. Phys. Lett.* **211**, 421 (1993).
33. T. Yamaguchi, Y. Shimamoto, T. Amemiya, M. Yoshimoto, T. Ohmori, *J. Phys. Chem. A* **104**, 219 (1996).
34. T. Amemiya, T. Ohmori, T. Yamaguchi, *J. Phys. Chem. A* **104**, 336 (2000).
35. V. K. Vanag, L. Yang, M. Dolnik, A. Zhabotinsky, I. R. Epstein, *Nature* **406**, 389 (2000).
36. K. Showalter, R. Noyes, K. Bar-Eli, *J. Chem. Phys.* **67**, 2514 (1978).
37. J. J. Tyson, *On Scaling the Oregonator Equations in Non-Linear Phenomena in Chemical Dynamics* (Springer, Verlag, Berlin, 1981), p. 222.

38. D. Garica-Selfa, A. P. Munuzuri, J. Perez-Mercader, D. Simakov, *J. Phys. Chem. A* **123**, 8083 (2019).

39. M. K. Reddy, Z. Szlavik, Z. Hagy-Ungvarai, S. C. Müller, *J. Phys. Chem.* **99**, 15081 (1995).

40. H. Ševčíková, I. Schreiber, M. Marek, *J. Phys. Chem.* **49**, 19153 (1996).

41. M. R. Tinsley, A. F. Taylor, Z. Huang, F. Wang, K. Showalter, *Phys. D (Amsterdam, Neth.)* **239**, 785 (2010).

42. T. Ko, G. B. Ermentrout, *Phys. Rev. E* **79**, 016211 (2009).

43. J. F. Totz, M. R. Tinsley, H. Engel, K. Showalter, *Sci. Rep.* **10**, 7821 (2020).

44. M. A. Schwemmer, T. J. Lewis, *Phase Response Curves in Neuroscience* (Springer, Berlin, 2012).

45. R. O. Dror, C. C. Canavier, R. J. Butera, J. W. Clark, J. H. Byrne, *Biol. Cybern.* **80**, 11 (1999).

46. A. F. Taylor, P. Kapetanopoulos, B. J. Whitaker, T. Toth, L. Bull, M. Tinsley, *Phys. Rev. Lett.* **100**, 214101–1 (2008).

47. M. R. Tinsley, A. F. Taylor, Z. Huang, K. Showalter, *Phys. Chem. Chem. Phys.* **13**, 17802 (2011).

Chapter 3

Novel Synchronization in Star Networks

3.1 Introduction

Complex biological, technological, and sociological networks can vary greatly in size and connectivity. Currently, there is interest in the relationship between the structure (connectivity) and the function (activity) in the dynamics of these complex networks. The structure-function relationship of biological networks, such as neurons or pancreatic beta cells, have some dependency on the topological structure of the network [1–4], and current neuroimaging techniques can show both structural and functional relationships in the brain. However, research reveals that there is commonly a mismatch between the two. This implies that the functional connectivity cannot be fully explained by considering only the structural connectivity of a network [5–7]. This leads to a hypothesis that the anatomic structure cannot fully explain the network dynamics [7]. Understanding the structure-function relationship is critical toward gaining insights into natural network design.

Investigating these complex networks can pose many challenges due to the large numbers of individual nodes and multiple degrees of connectivity. However, many of the complex networks that occur in nature share global statistical features [8–12], including small-world networks [8, 10–12] and scale-free networks [3, 9, 13–15]. Small world networks consist of a population of nodes that are not globally connected but will have a short path between any two nodes in the population [9, 11–13]. In many natural networks, a small number of nodes will have many more connections than the average node. These types of networks are termed as scale-free networks [9, 15, 16]. In scale-free networks the fraction of nodes having k edges (p(k)) decays as a power law, where $p(k) \sim k^{-\gamma}$ and γ is typically between 2 and 3 [13]. These reoccurring patterns, defined as network motifs, can greatly reduce the number of nodes needed in studies, as the dynamics of a complex network are thought to be governed by the smaller constituent networks or motifs [13, 17].

One means of investigating the dynamical properties of a network is to consider the link between elements with similar structural symmetries and the functional modules that arise within the network [18, 19]. In 2012, Bergner et al. presented a different approach to demonstrate how network dynamics can emerge through functional rather than structural connectivity [15]. Utilizing a star network of Stuart-Landau (SL) oscillators consisting of a central hub oscillator bidirectionally coupled to a number of peripheral oscillators, they reported a phenomenon termed "remote synchronization". This star network can be described as a minimal scale-free network, as it possess one highly connected oscillator and several peripheral oscillators with only a single connection [3, 9, 13, 14]. During experiments and computational studies, the indirectly connected peripheral oscillators would become phase synchronized but would not synchronize with the hub oscillator. The ability of the peripheral oscillators to synchronize was thought to depend on a memory of the amplitude of the hub oscillator. Several requirements were proposed to observe remote synchronization in a star network: (a) a large frequency difference between the hub oscillator and the peripheral oscillators, (b) an intermediate coupling strength that would not cause global synchronization of the system, and (c) a small degree of heterogeneity between the peripheral nodes, as the signal from the hub is considered weak. Finally it was originally hypothesized that the oscillators must be capable of amplitude modulations, as this is how the synchronizing signal was transmitted [15, 20]. This last condition would preclude the use of oscillators that do not display amplitude, such as the Kuramoto phase oscillators. This early work on remote synchronization has been reported in a variety of scale-free networks using both SL oscillators and Kuramoto oscillators [18, 21–23], suggesting that there may be more than one mechanism that can produce remote-synchronization-like behavior in networks comprising non-SL oscillators.

The dynamical properties of a network are not only dictated by structure-function relationships but also by the intrinsic properties of the individual oscillators and their response to perturbations [24–26]. The majority of the work into remote synchronization to date has used the sine-like SL oscillators, which are capable of large variations in their amplitude. However, many of the oscillators found in biological networks have relaxation-type dynamics and can respond to both activatory and inhibitory perturbations. Relaxation-type oscillators are also characterized by a portion of their cycle being refractory during which time they are unable to respond to a perturbation. The Belousov-Zhabotinsky (BZ) reaction has been used many times as a model for a variety biological systems due to the relaxation form of its oscillations, which was discussed in Chapter 2, Fig. 2.7 experimental, and Fig. 2.8 computational phase response curves (PRC) [27–30].

This chapter will provide details of experimental and computational results exploring a star network comprising photochemically coupled BZ micro-oscillators using excitatory or inhibitory coupling conditions. The experimental system consists of micro-oscillators constructed by loading the catalyst tris(bipyridine)ruthenium(II) chloride onto cation exchange beads, which are immersed into a catalyst-free BZ solution. Selection of the appropriate catalyst-free solution allows for the excitatory and inhibitory responses to the real-time light-based feedback used to couple the star networks. Computational results reported here were completed with a 3-variable-photosensitive ZBKE model using either excitatory or inhibitory conditions. Finally, we discuss a mapping approach used to give insights into the mechanism that produces the phase clustering, maximum heterogeneity, and grouping of the peripheral oscillators found during the study. This clustering behavior of the peripheral oscillators is a novel form of synchronization, as the mechanism does not depend on amplitude modulations seen in remote synchronization. The mapping approach shows that perturbations are transmitted through the hub via a change in the hub's phase. The hub then aligns the phases of the peripheral oscillators by a phase-delaying perturbation.

3.2 Experimental

The instrumental set-up and preparation of the catalyst-free BZ solutions used in this study are detailed in chapter two. To achieve the required significant difference in the natural periods of the oscillators, the amount of the ruthenium catalyst loaded onto the micro-oscillators is varied. The micro-oscillators are loaded with either $2.5 \times 10^{-6}\,\mathrm{mol\,g^{-1}}$ or $8.36 \times 10^{-6}\,\mathrm{mol\,g^{-1}}$ of ruthenium catalyst and labeled as the peripheral and hub oscillators, respectively. The natural period range of the peripheral oscillators is 80-100 s, while the hub oscillators have a range of 50-70 s. Small variations in the loading of the catalyst introduce a natural heterogeneity in both the peripheral and hub micro-oscillators. The creation of the individual chemical micro-oscillators is detailed in chapter two.

The micro-oscillators are illuminated with a constant light intensity ϕ_0 at 440 nm, using a spatial light modulator (SLM). During a chemical oscillation, the oxidation state of the ruthenium catalyst changes from +2 to +3. Since the catalyst is virtually transparent at 440 nm, this change in oxidation state changes the amount of light that is reflected into the CCD camera, which transmits the image as a gray scale to the computer. The photosensitive nature of the ruthenium catalyst allows for real-time coupling through changes in the illumination on a micro-oscillator based upon the current oxidation states of the micro-oscillators within the network.

The creation of a star network begins by monitoring both peripheral and hub oscillators submerged in the chosen catalyst-free BZ solution to determine the natural period of each micro-oscillator. The star network is created by choosing a hub that will produce an ~30% difference in natural periods between the hub and the fastest peripheral oscillator. The peripheral micro-oscillators selected are chosen to reduce the difference in their natural periods as much as possible, ~1-2%, Fig. 3.1. Coupling of the micro-oscillators into a star network, as illustrated in Fig. 3.1, is created by illuminating each oscillator j with a light intensity ϕ_j according to

$$\phi_j = \phi_0 + \frac{K}{d} \sum_{i=1}^{N+1} A\left(g_i - g_j\right), \tag{3.1}$$

where ϕ_j is the projected light intensity on oscillator j, ϕ_0 is the background light intensity, K is the coupling strength, d is the degree of each node, A is an adjacency matrix, and $\mathrm{g_i}$ and $\mathrm{g_j}$

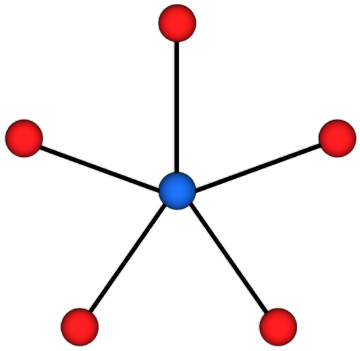

Figure 3.1. Five node star network consisting of five peripheral nodes (red) and a hub (blue). The peripheral nodes have a difference in their natural periods of ~1-2%. The hub oscillator will have a natural period $\sim 30\%$ faster than the faster peripheral node.

are the normalized gray levels of oscillators i and j. In this star network, $\mathrm{N} + 1 = 6$, for the five peripheral nodes and a single central hub. The response of a micro-oscillator due to changes in the light intensity is dependent upon the initial concentrations of the catalyst-free BZ solution used. The predicted responses for each solution are given by the experimental PRCs shown in Chapter 2, Fig. 2.7.

3.3 Experimental Results

Experiments are carried out by constructing star networks, Fig. 3.1, using hub and peripheral micro-oscillators submerged in either an excitatory or inhibitory catalyst-free BZ solution, with coupling according to Eq. (3.1). Remarkably, very similar results are seen in both excitatory and inhibitory coupled star networks, where two types of novel synchronization are observed. The first type is a single cluster state of phase-locked peripheral micro-oscillators (1-cluster synchronization). The second type involves two clusters of phase locked peripheral micro-oscillator (2-cluster synchronization), which are occupied as either a 4-1 or 3-2 cluster. The numbers correspond to the number of peripheral micro-oscillators occupying a cluster. In all cases, the hub micro-oscillator does not phase synchronize with the peripheral micro-oscillators. A visual representation of the behaviors is constructed by plotting the unwrapped phase of the micro-oscillators as a function of time, Fig. 3.2 (inhibitory) and Fig. 3.3 (excitatory). The single cluster state can be seen in Fig. 3.2(a) and Fig. 3.3(a), where the unwrapped phases of the peripheral micro-oscillators are parallel with each other indicating they are phase-locked. However, the hub (red) has a divergent phase from the peripheral micro-oscillator's phase lines. To discern the 1-cluster state shown in Figs. 3.2(a) and 3.3(a), a small section of time is plotted in Figs. 3.2(b) and 3.3(b). The phase lines for the peripheral micro-oscillators are parallel, implying they are phase-locked and also overlapping with nearly identical firing times, marked by squares indicating they are oscillating in phase. In Figs. 3.2(c), 3.2(d), 3.3(c), and 3.3(d), 2-cluster states are illustrated with the 4-1 state in (c) and the 3-2 state shown in (d). The phase lines of the peripheral micro-oscillators are still parallel with each other, indicating they are phase-locked. However, they are clearly separated by a constant phase, which when measured is $\sim \pi$. This result indicates the two clusters are firing approximately anti-phase to one another. The firing times for the micro-oscillators contained in a cluster are marked with a square or diamond.

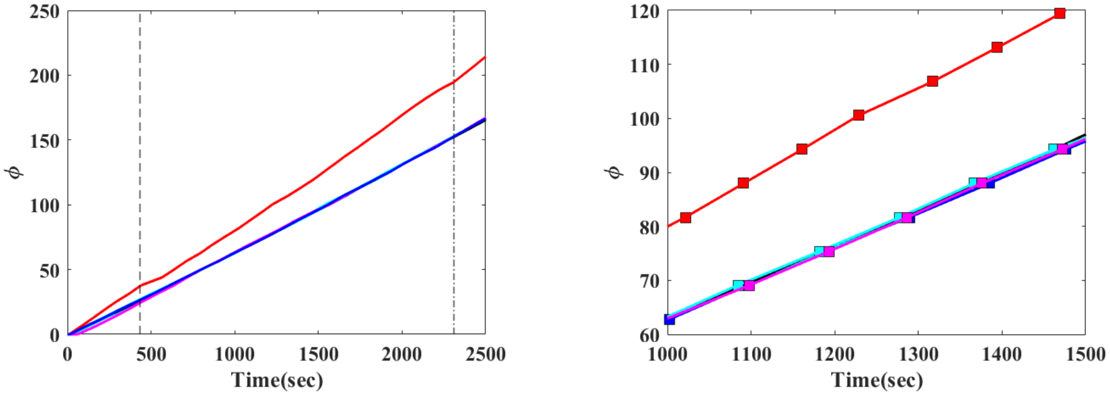

(a) Inhibitory 1-cluster state (long term) (b) Detail of (a) 1-cluster state

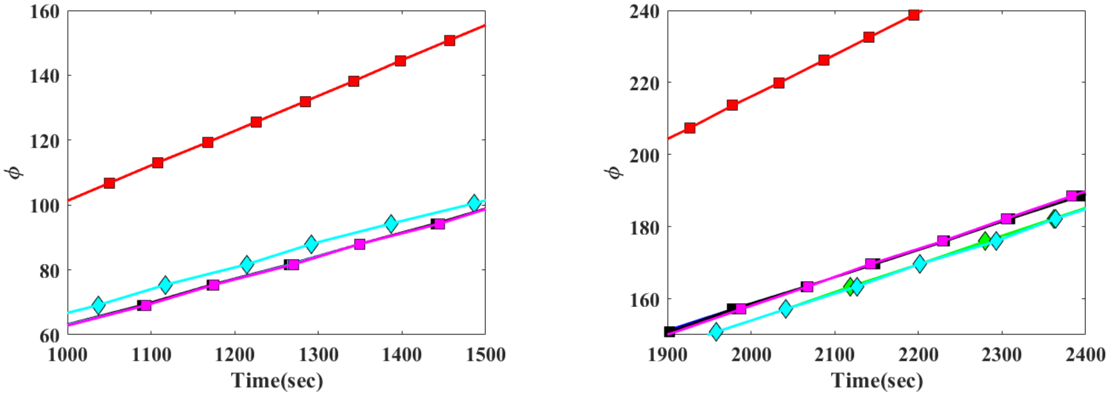

(c) Inhibitory 2-cluster state with 4-1 occupancy (d) Inhibitory 2-cluster state with 3-2 occupancy

Figure 3.2. The unwrapped phase of each oscillator as a function of time from experiments with inhibitory coupling. (a) A 1-cluster synchronization state with the peripheral oscillators forming a single phase-locked cluster. The dashed lines show when the coupling was switched on and switched off. (b) Detail of (a). (c) A 2-cluster synchronization state with a 4-1 occupancy. The firing times for the cluster of 4 are indicated with squares, and those of the single oscillator are indicated with diamonds. (d) A 2-cluster synchronization state with 3-2 occupancy. The firing times for the cluster of 3 are indicated with squares, and those of the cluster of 2 are indicated with diamonds. In each plot, green, cyan, magenta, or blue indicate peripheral oscillators and the red line indicates the hub oscillator. Initial concentrations of the catalyst-free BZ solution: $[\mathrm{BrO}_3^-] = 0.320$, $[\mathrm{MA}] = 0.096$, $[\mathrm{H}^+] = 0.780$, and $[\mathrm{Br}^-] = 0.0600$. The background light intensity was set to $\Phi_0 = 0.081$ mW cm^{-2}.

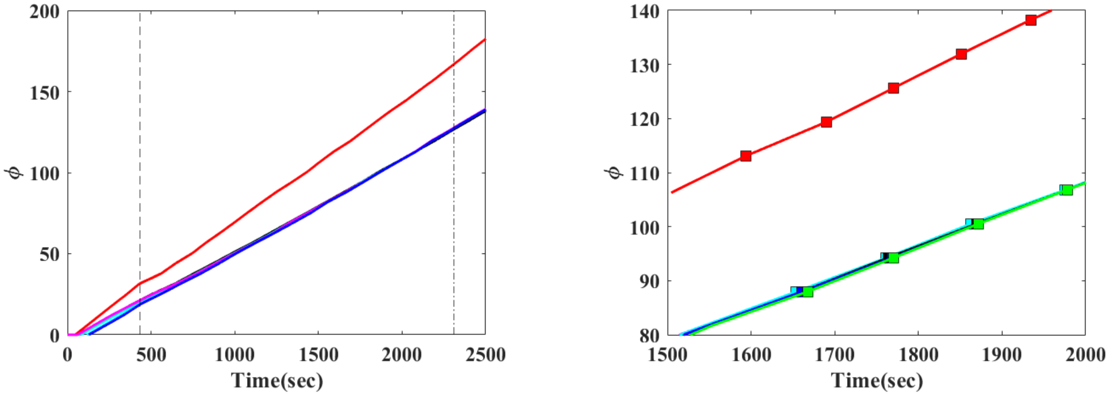

(a) Excitatory 1-cluster state (long term)

(b) Detail of (a) 1-cluster state

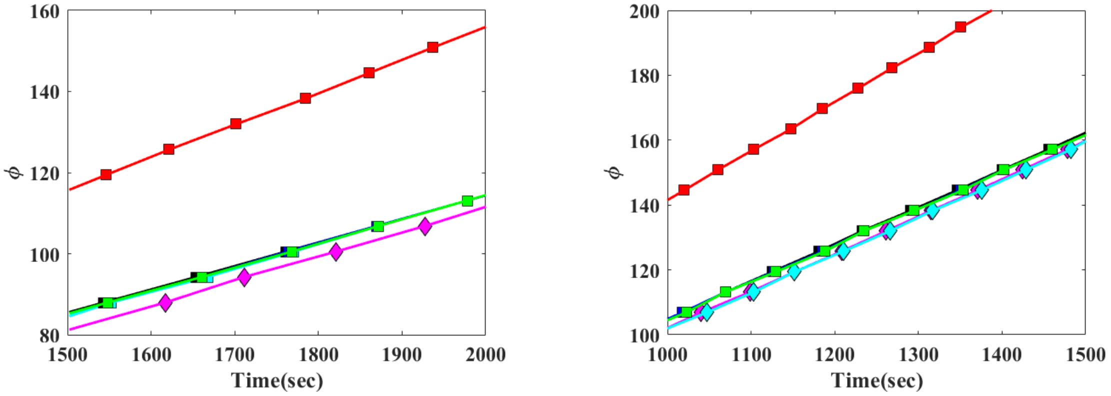

(c) Excitatory 2-cluster state with 4-1 occupancy

(d) Excitatory 2-cluster state with 3-2 occupancy

Figure 3.3. The unwrapped phase of each oscillator as a function of time from experiments with excitatory coupling. (a) A 1-cluster synchronization state with the peripheral oscillators forming a single phase-locked cluster. The dashed lines show when the coupling was switched on and switched off. (b) Detail of (a). (c) A 2-cluster synchronization state with a 4-1 occupancy. The firing times for the cluster of 4 are indicated with squares, and those of the single oscillator are indicated with diamonds. (d) A 2-cluster state with 3-2 occupancy. The firing times for the cluster of 3 are indicated with squares, and those of the cluster of 2 are indicated with diamonds. In each plot, green, cyan, magenta, or blue indicate peripheral oscillators and the red line indicates the hub oscillator. Initial concentrations of the catalyst-free BZ solution: $[BrO_3^-] = 0.640$, $[MA] = 0.096$, $[H^+] = 0.780$, and $[Br^-] = 0.0600$. The background light intensity was set to $\Phi_0 = 0.095$ mW cm^{-2}.

3.4 Computational Results

A modified three-variable ZBKE model was used in all computational studies of the star network in this study [31–34] to simulate each oscillator in the network. The model incorporates a parameter, α, that determines the response of the photosensitive catalyst to light [31]. A detailed description of the ZBKE mechanism and model is discussed in chapter 2.5.2. To simulate experimental results, α was set at either 1 or 0 during simulations. For $\alpha = 1$, an oscillator primarily responds via the excitatory pathway, in which bromous acid is the critical product following the photoexcitation of the ruthenium complex. In contrast, for $\alpha = 0$, an oscillator responds via the inhibitory channel, in which bromide is the critical product of the photoexcitation. Computational PRCs, based on the modified three-variable ZBKE model with either excitatory or inhibitory responses to light perturbations, Fig. 2.7, are in good agreement with the experimental PRCs, Fig. 2.6. Computational star networks of oscillators using either excitatory or inhibitory ZBKE oscillators exhibit essentially all of the behavior observed in the experiments. Figures 3.4(a) and 3.4(b) show 1-cluster synchronization states for the excitatory and inhibitory systems, respectively. Figures 3.4(c) and 3.4(d) show the 2-cluster synchronization states in inhibitory systems with 4-1 and 3-2 occupancies, respectively. In all cases, the hub oscillator is not synchronized with the peripheral oscillators.

Observations from the experimental system show that different occupancies of the 2-cluster states may occur for the same value of the coupling constant during different trials. This multistability is also seen in the ZBKE simulations. Targeting a particular cluster state at a given value of coupling strength can be achieved by the appropriate choice of the initial conditions. This is shown in Figs. 3.4(c) and 3.4(d), where using the same parameters as in 3.4(b), a 4-1 or 3-2 synchronized 2-cluster state can be produced. Multistability is also observed in the excitatory system, with the coexistence of the synchronized 1-cluster, 2-cluster 4-1 and 3-2 states.

Remote synchronization reported by Bergner et al. [15] occured at coupling strengths less than those required for global synchronization. The findings in star networks of BZ osillators are consistent with this result. Figures 3.5(a) and 3.5(b) show the dominant behaviors at different coupling strengths from simulations of excitatory and inhibitory oscillators, respectively. In the case of excitatory oscillators, clustering behavior is dominant at intermediate coupling strengths prior to the onset of global synchronization, Fig. 3.5(a). Global synchronization at large coupling strengths is also observed in the experimental system. In contrast, oscillators in a star network using inhibitory coupling exhibit oscillator death at higher coupling strengths, Fig 3.5(b). The strong signal provided by the hub oscillator sufficiently delays the peripheral oscillators such that they do not have time to fire before receiving the next signal. This is predicted to occur at high coupling strengths corresponding to light intensities beyond those available in the experiments. Examples of global synchronization and oscillator death in ZBKE simulations are shown in Figs. 3.5(c) and 3.5(d), respectively.

During the transition from low coupling strength to the synchronized region and from the synchronized region to global synchronization or oscillator death, regions of complex behavior are found. This investigation shows that this complexity takes the form of high-order periodicity or aperiodic dynamics.

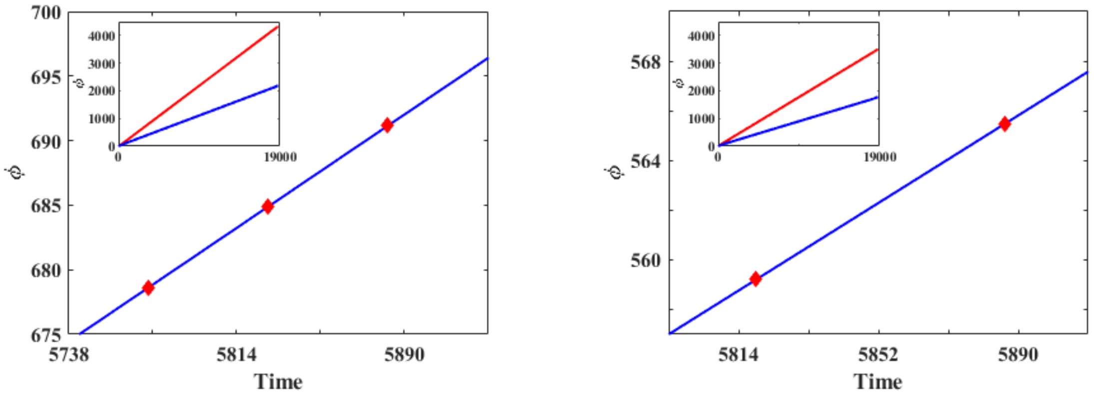

(a) Single cluster state in the excitatory system (b) Single cluster state in the inhibitory system

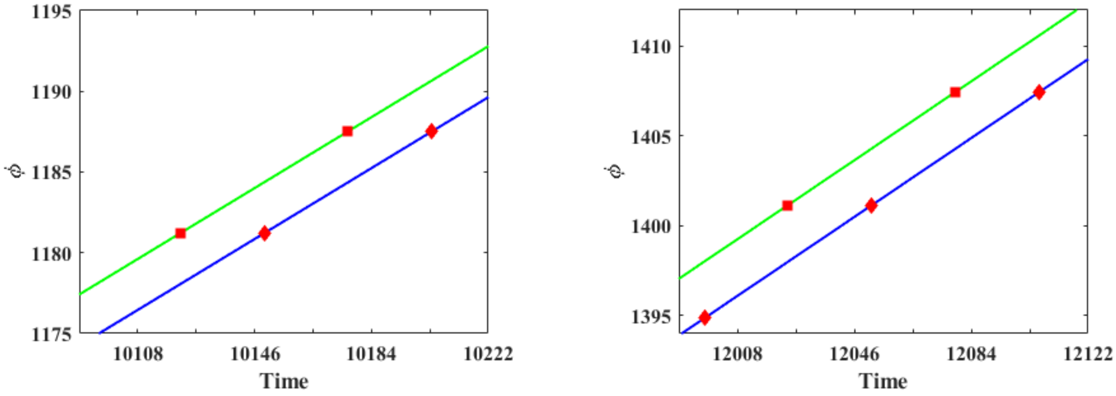

(c) 2-cluster state having a 4-1 occupancy (d) 2-cluster state having a 3-2 occupancy

Figure 3.4. Novel synchronization in star networks of coupled ZBKE oscillators in simulations. (a) Excitatory system and (b) inhibitory system (insets show the long-term behavior). (c) Inhibitory system with a 2-cluster synchronization state having a 4-1 occupancy. The firing times for the cluster of 4 are indicated with squares, and those of the single oscillator are indicated with diamonds. (d) Inhibitory system with a 2-cluster state having a 3-2 occupancy. The firing times for the cluster of 3 are indicated with squares, and those of the cluster of 2 are indicated by diamonds. The natural period of the hub oscillator is 29.72, while the natural period of the peripheral nodes are equally spaced in the range of 44.26-44.95. Caluclations are performed utilizing Euler's method with a dt = 0.0019. Time is dimensionless in all simulations (Chapter 2.5.2).

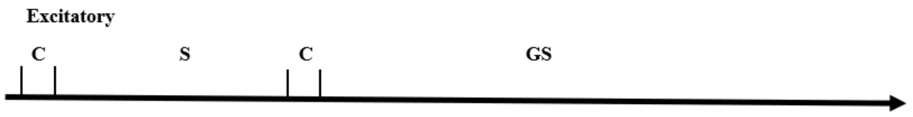

(a) Regions of behavior in excitatory system

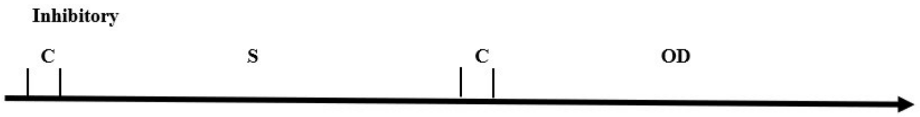

(b) Regions of behavior in inhibitory system

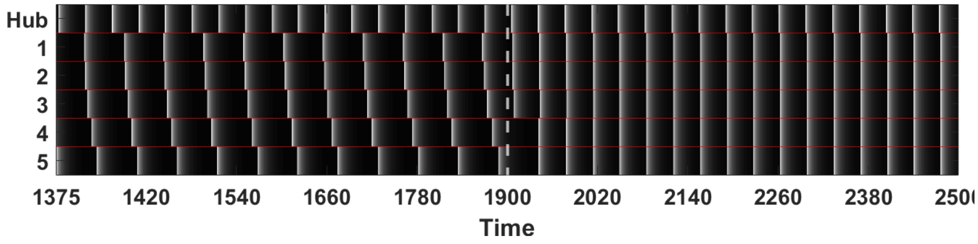

(c) Global synchronization at high coupling strength in excitatory system

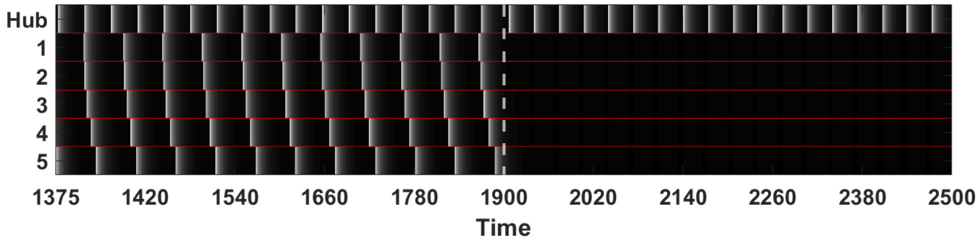

(d) Oscillator death at high coupling strength in inhibitory system

Figure 3.5. Regions of behavior with increasing coupling strength in simulations of the excitatory system (a) and the inhibitory system (b): complex behavior (c), synchronization (S), global synchronization (GS), and oscillator death (OD). Both 1-cluster and 2-cluster synchronization occur across the entire synchronization regions. (c) Global synchronization exhibited in increasing coupling strength from S region to GS region in (a). (d) Oscillator death exhibited on increasing coupling strength from S region to OD region in (b). Time is dimensionless in all simulations (Chapter 2.5.2).

3.5 Mapping Approach

Studies of remote synchronization in networks of Stuart-Landau oscillators by Bergner et al. [15] reported that the signal leading to remote synchronization is transmitted via modulation of the hub oscillator amplitude. In this study of novel synchronization using a star network comprising BZ oscillators, it was found that the coupling perturbation has little effect on the amplitude of the hub oscillation. It may, however, lead to significant changes in the timing of an oscillator firing, as illustrated by the PRCs shown in Fig. 2.6.

We now will focus on how the change in firing time leads to the 1-cluster and 2-cluster synchronization seen in this system. Figure 3.6(a) shows simulation results of a star network using excitatory photochemical oscillators. Coupling is initiated at 950 (dashed line), and following a short transient, a repeating firing sequence of the oscillators in a 1-cluster state is established. We can observe that the hub will fire twice within each cycle of the peripheral oscillators. The

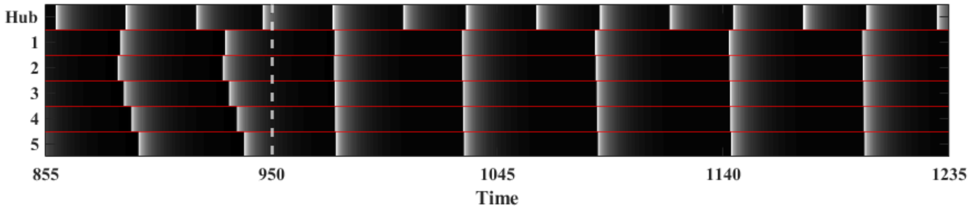

(a) Firing sequence of single cluster state with excitatory coupling

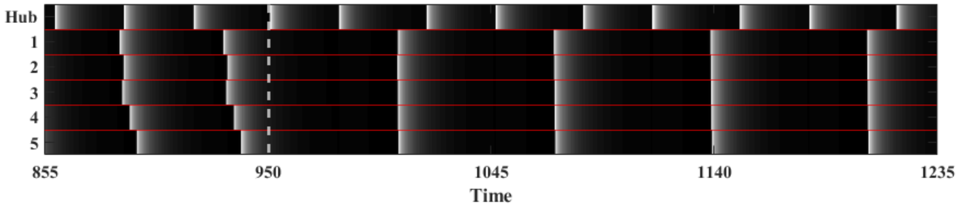

(b) Firing sequence of single cluster state with inhibitory coupling

Figure 3.6. (a) Firing sequence of single cluster state with excitatory coupling switched on at 950. The hub oscillator fires twice within the cycle of the peripheral oscillators, where the unperturbed cycle is the natural period of the hub. The perturbed cycle of the hub is shorter than the natural period due to the excitatory coupling. The peripheral oscillators 1-5 align in phase due to an inhibitory response to the perturbation from the hub. (b) Firing sequence of single cluster state with inhibitory coupling switched on at 950. The hub oscillator fires twice within the cycle of the peripheral oscillators, where the unperturbed cycle is the natural period of the hub. The perturbed cycle of the hub is longer than the natural period due to the inhibitory coupling. The peripheral oscillators 1-5 align in phase due to an inhibitory response to the perturbation from the hub. Time is dimensionless in all simulations.

first firing of the hub occurs early in the refractory region of its cycle, while the second firing occurs when the peripheral oscillators are in the inhibitory portion of their cycle and are therefore each phase delayed. When they fire, they do so almost at the same time, and the hub is phase advanced. The hub then completes an unperturbed cycle and the firing sequence repeats.

The simulation shown in Fig. 3.6(b) demonstrates 1-cluster synchronization with inhibitory coupling. After a short transient, the same repeating firing sequence is established as in the excitatory system. In both cases, with excitatory or inhibitory oscillators, it is an inhibitory signal from the hub that leads to the phase alignment of the peripheral oscillators. In both cases, the hub fires twice within the cycle of the peripheral oscillators, and in both cases the first signal has minimal impact because the peripheral oscillators are in their refractory period. The primary difference between the two systems is that the peripheral oscillators phase advance the hub in the excitatory system and phase delay the hub in the inhibitory system.

Changing initial conditions in a simulation can produce a different firing sequence and establish a 2-cluster state. A 2-cluster 4-1 state is shown in Fig. 3.7(a) for an inhibitory system, and a 2-cluster 3-2 state is shown in Fig. 3.7(b) for an excitatory system. During 2-cluster synchronization, the firing sequence is the following: the hub fires, and then the first cluster fires, the hub fires again, and the second cluster fires. When the peripheral oscillators fire in the inhibitory system the hub is delayed; however, when they fire in the excitatory system, the hub fires almost immediately and is phase advanced. The occupancy of the clusters is dependent on the initial conditions.

The 1-cluster state provides a well-defined sequence of firing times that can be used to develop a map representation of the sequential firings and perturbations of the oscillators. The map can then be used to understand the underlying dynamics that lead to the novel synchronization. We will use a minimal star network consisting of two peripheral oscillators and a hub oscillator to develop the map representation, Fig. 3.8. To construct the map representation, we will need to make two assumptions on how the peripheral nodes will respond to a perturbation at phase ϕ from the hub. First, we assume we can determine directly from the PRC the response of each oscillator. We will also assume that the first perturbation received by the peripheral oscillators from the hub, during a given cycle, occurs in the refractory region. Support for this assumption comes from the computational PRC's, Fig. 2.7, which show large refractory regimes early in the

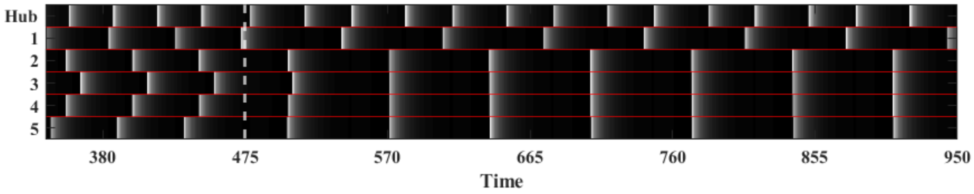

(a) 4-1 occupancy in inhibitory system

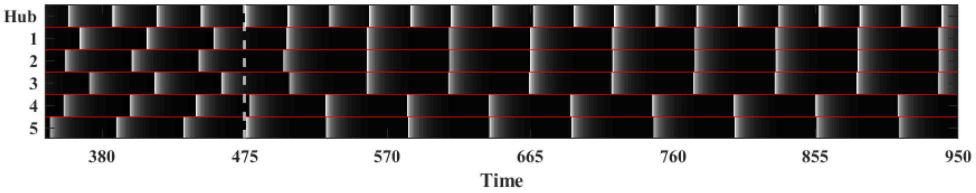

(b) 3-2 occupancy in excitatory system

Figure 3.7. Firing sequence of 2-cluster states with coupling switched on at 475. (a) A 4-1 state in an inhibitory system, and (b) a 3-2 state in an excitatory system. Time is dimensionless in all simulations.

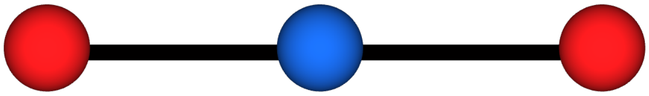

Figure 3.8. Minimal network consisting of two peripheral nodes (red) and a hub (blue). The peripheral nodes represent the fastest and slowest nodes in the five nodes system. The hub oscillator will have a natural period ~ 30% faster than the faster peripheral node.

phase of both exictatory and inhibitory oscillators. Therefore, the first perturbation by the hub is ignored in the analysis. The natural periods of oscillator 1, 2, and the hub are T_1, T_2, and T_h^{nat}, respectively. Oscillator 1, being the faster oscillator, fires first, and it therefore follows that it is receiving the perturbation from the hub at a phase ϕ_1^i later in its cycle than at phase ϕ_2^i, at which the oscillator 2 receives the perturbation. Using this we assume that $T_2 > T_1$ and $\phi_1 > \phi_2$. A schematic of the firing sequence of the inhibitory coupled 1-cluster state is shown in Fig. 3.9. In the inhibitory system, the period of the hub on the perturbed cycle T_h^i is larger than the natural period T_h^{nat}. In the excitatory system, the period T_h^i is less than T_h^{nat}. However, the mapping approach is valid for both as the sequence of firings are the same in both systems.

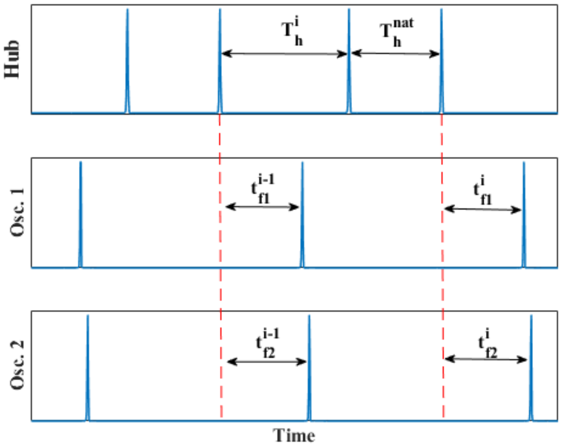

Figure 3.9. Map representation of the 1-cluster RS firing sequence. The hub oscillator fires twice for each cycle of the peripheral oscillators. The first firing of the hub is considered to have no effect on the peripheral oscillators. On the *i-th* cycle, oscillator 1 receives the perturbation from the hub at phase ϕ_1^i and oscillator 2 receives the perturbation at phase ϕ_2^i

We begin the mapping description by constructing a piece-wise linear approximation, black line Fig. 3.10, of the PRC (Z(ϕ)). The phase response is defined as zero between 0 and ϕ^*.

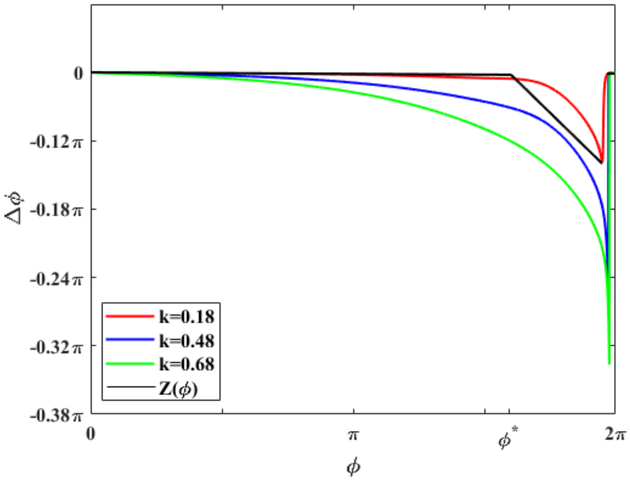

Figure 3.10. Three PRCs, red line, blue line and green line, produced using an increasing size, respectively, of perturbation. A larger perturbation corresponds to a larger coupling strength in the coupled oscillator system. Black line: piece-wise linear representation of the red line PRC. ϕ^* corresponds to $\frac{2\pi T_h^{nat}}{T_j}$ where T_j is the natural period of peripheral oscillator j. Examination of Fig. 3.6 shows that in the indicated firing sequence, a length of time of at least T_h^{nat} occurs before the peripheral oscillators are perturbed for the second time within their cycle. Therefore, for convenience the value of the PRC is set to 0 in the region, $0 \leq \phi \leq \phi^*$.

Z(ϕ) then decreases linearly to a minimum value at phase ϕ_{crit}. Between phase ϕ_{crit} and 2π, the PRC is again defined to be zero. The slope of the linearly decreasing region of the PRC will be defined as Z'. As discussed in Chapter 2.6.2, a larger perturbation will cause the PRC to have a more negative slope. This is also shown in Fig. 3.10 with the slope becoming more negative with larger perturbations. The approximation can be fit to any of the scenarios in Fig. 3.10 by shifting ϕ^* and changing Z' to fit the new curve. This piece-wise approximation of the real PRC is considered valid, as both are monotonically decreasing functions in the phase range of interest.

The difference in the firing times of the peripheral oscillators after a perturbation from the hub is related to their phase synchronization. The map g of the difference in firing acts on the previous difference in firing times such that t^i_{f2}-$t^i_{f1} = g(t^{i-1}_{f2}$-$t^{i-1}_{f1})$. We can obtain the time of firing for oscillator 1 on its i^{th} cycle after the perturbation directly from Fig. 3.9, such that

$$t^i_{f1} = \frac{T_1}{2\pi}\left(2\pi - \phi^i_1 - \Delta\phi^i_1\right), \tag{3.2}$$

with the change in phase, $\Delta\phi_1$, obtained from the PRC, where $\Delta\phi_1 = Z(\phi_1)$. The value of $Z(\phi_1)$ can be shown using the appropriate section of the piece-wise linear PRC as

$$Z(\phi) = Z'\left(\phi - 2\pi\frac{T_h^{nat}}{T_1}\right). \tag{3.3}$$

Substituting this value into Eq. (3.1) yields

$$t^i_{f1} = T_1 - \frac{T_1}{2\pi}\left(1 + Z'\right)\phi_1^{i-1} + Z'T_h^{nat}. \tag{3.4}$$

We can define the phase at which oscillator 1 is perturbed by

$$\phi^i_1 = \frac{2\pi}{T_1}\left(T^i_h + T^{nat}_h\right) - t^{i-1}_{f1}, \tag{3.5}$$

and substitute this into Eq. (3.3). The time that oscillator 1 will fire after perturbation can now be expressed in terms of its firing time on its previous cycle as

$$t^i_{f1} = T_1 - \left(1 + Z'\right)\left(\tau - t^{i-1}_{f1}\right) + Z'T^{nat}_h, \tag{3.6}$$

where τ = (T_h^i+T_h^{nat}). Likewise, an expression for t_{f2}^i is given by

$$t_{f2}^i = T_2 - \left(1 + Z^{'}\right)\left(\tau - t_{f2}^{i-1}\right) + Z^{'} T_h^{nat}. \tag{3.7}$$

By subtracting Eq. (3.5) from Eq. (3.6) the difference in firing times gives the expression for the map g

$$(t_{f2}^i - t^i)f1 = \Delta T + \left(1 + Z^{'}\right)\left(t_{f2}^{i-1} - t_{f1}^{i-1}\right), \tag{3.8}$$

where ΔT = T_2 - T_1. Solving for the fixed point at t_{f2}^i - t_{f1}^i = t_{f2}^{i-1} - t_{f1}^{i-1} of this map gives

$$t_{f2} - t_{f1} = \frac{\Delta T}{Z'}. \tag{3.9}$$

Stability analysis shows the fixed point is stable for -2 $<$ Z′ $<$ 0. Qualitatively, the relationship shown in Eq. (3.9) is described as a competition between two process, divergence and realignment. The difference in the natural periods, ΔT, of the peripheral nodes leads to a difference in their phase velocities, which creates a divergence in their phases. The perturbation from the hub counteracts this divergence by delaying the faster oscillator more than the slower oscillator, which realigns the phases. The faster peripheral oscillator is always perturbed later in its phase and receives a larger delay, as both the real and approximated PRCs are monotonically decreasing functions.

The result of these competing processes is a stable firing difference in the firing times of the peripheral oscillators, Eq. (3.9). The relationship in Eq. (3.9) also predicts that the difference in firing times will also increase as the difference in natural periods, ΔT, increases. Close examination of the computational results, Figs. 3.6 and 3.7, shows that the oscillators do not fire at exactly the same time and the difference in the firing times increases as ΔT increases. To further illustrate this relationship, ZBKE simulations using the simplified network, Fig. 3.8, were performed by holding the coupling strength constant and increasing the difference in the natural periods of the peripheral oscillators. The results from these simulations, Fig. 3.11, show the difference in firing times increase approximately linearly with an increasing ΔT, as predicted by Eq. (3.8).

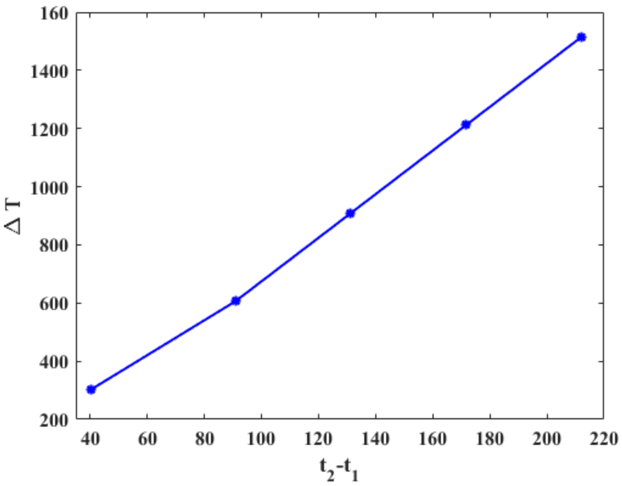

Figure 3.11. The difference in firing times, t_{f2} - t_{f1}, of the peripheral oscillators after receiving a perturbation from the hub as the difference in their natural periods increases at a constant coupling strength. The linear relationship is predicted by equation 3.8.

In ZBKE simulations of both the inhibitory and activatory coupled systems at a given coupling strength there is a maximum difference in the natural periods of the peripheral oscillators, ΔT_{max}, above which synchronization is no longer observed. In the inhibitory system, this maximum difference increases with increasing coupling strength. As discussed earlier in section 2.62, the larger the magnitude of the perturbation, the steeper and more negative the inhibitory slope of the PRC and the approximation Z'. We can define this maximum allowed heterogeneity in the natural periods (R_{max}) as a ratio

$$R_{max} = \frac{T_2 - T_1}{T_2}. \tag{3.10}$$

To develop a value for R_{max} we must consider a restriction on the system's ability to produce phase clusters. The divergence due to the ΔT in the peripheral oscillators is compensated for by delaying the faster oscillator more than the slower oscillator, which leads to the phase alignment. For this condition to be true, oscillator 1 must be perturbed at a later phase than oscillator 2, but before ϕ_{crit}, Fig. 3.10. If oscillator 1 receives the perturbation after ϕ_{crit}, the delay would be less than that of oscillator 2. Therefore, the value of ϕ_1 must be within the range

$$\phi_2 < \phi_1 \leq \phi_{crit}. \tag{3.11}$$

An approximate expression for the difference in the phases of perturbations for a given ΔT can be developed by first defining these phases directly from Fig. 3.9:

$$\phi_1 = \frac{2\pi}{T_1}\left(\tau - t_{f1}\right), \tag{3.12}$$

$$\phi_2 = \frac{2\pi}{T_2}\left(\tau - t_{f2}\right), \tag{3.13}$$

where t_{f1} and t_{f2} are the firing times at the fixed point of the map g. The differences in these phases are then given by Eq. (3.11),

$$\phi_1 - \phi_2 = \frac{2\pi}{T_1}\left(\tau - t_{f1}\right) - \frac{2\pi}{T_2}\left(\tau - t_{f2}\right). \tag{3.14}$$

By making the approximation of $T_1 = T_2$,

$$\phi_1 - \phi_2 = \frac{2\pi}{T_2}\left(t_{f2} - t_{f1}\right). \tag{3.15}$$

Then substituting in the fixed point value from Eq. (3.8),

$$\phi_1 - \phi_2 = \frac{\frac{2\pi\Delta T}{T_2}}{Z'}. \tag{3.16}$$

Using the upper limit from Eq. (3.9), $\phi_1 = \phi_{crit}$, the maximum allowed heterogeneity in the natural periods (R_{max}) is given by

$$\frac{\Delta T_{max}}{T_2} = R_{max} = -\frac{\left(\phi_{crit} - \phi_2\right) Z'}{2\pi}. \tag{3.17}$$

ZBKE simulations investigating the effect of coupling strength on R_{max} show agreement with Eq. (3.16), Fig. 3.12. The maximum heterogeneity increases with increasing coupling strength up to $\sim 4 \times 10^{-3}$. At this point the peripheral nodes are pushed into a non-oscillatory state due to the large delays as a result of perturbations received from the hub.

The value of ϕ_2 will have a dependence on the natural period T_h^{nat} and perturbed period T_h^i of the hub. Examining the period of the peripheral oscillators during synchronization at the R_{max} value using the ZBKE model shows that both oscillators are significantly delayed, Fig. 3.13. This result implies that ϕ_2 has a value close to ϕ_{crit}. The importance in the relationship between

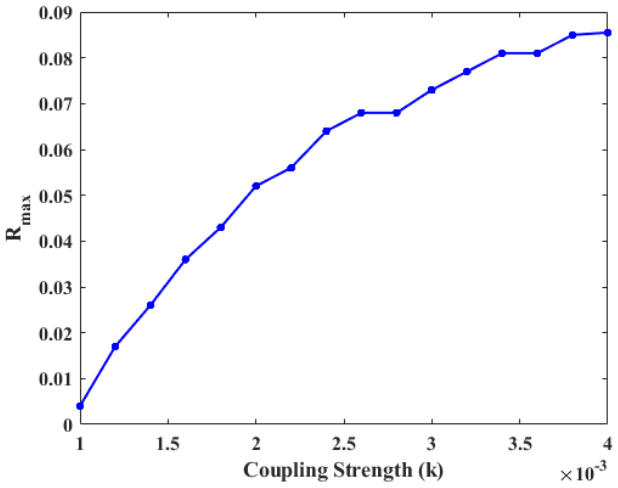

Figure 3.12. The maximum allowed heterogeneity ratio, R_{max}, observed in the inhibitory system as a function of the coupling strength (k).

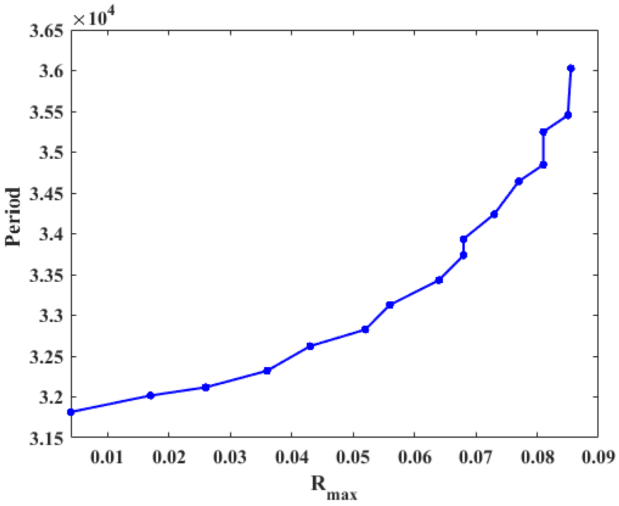

Figure 3.13. The period of the synchronized peripheral oscillators, observed in the inhibitory system as a function of the maximum allowed heterogeneity ratio, R_{max}.

realignment and heterogeneity is expressed in Eq. (3.16). A higher coupling strength will yield a larger and steeper Z', which implies a larger realignment role by the perturbation. This will allow for a larger heterogeneity in the peripheral oscillators natural periods. The derivation of expression Eq. (3.16) shows that the origin of the heterogeneity limit is associated with the maximum realignment/delay that the faster oscillator can experience due to the perturbation from the hub. We can also evaluate the heterogeneity in Eq. (3.16) at different values of ϕ_2 close to the value ϕ_{crit} using the linear approximations to the three real PRCs in Fig. 3.10. In Fig. 3.14 we can see that as the phase difference between ϕ_2 and ϕ_{crit} increases at the time of the perturbation, the allowed heterogeneity increases with coupling strength. The mapping approach does not allow for the explicit determination of ϕ_2. However, it clearly shows a relationship in $R_{\max}$ and the coupling strength in an inhibitory system.

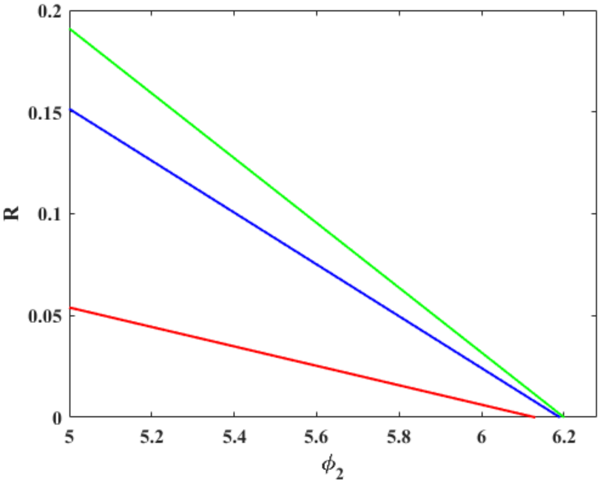

Figure 3.14. Mapping representation of $R_{\max}$ values for three different PRC's. The color scheme corresponds to the PRCs from Fig. 3.10.

This mapping approach was developed for the inhibitory system and an equivalent approach can be used to develop an understanding of the activatory system. The only difference in the firing sequence shown in Fig. 3.9 for the activatory system is that $T_h^i < T_h^{nat}$, which is due to a phase advancing perturbation from the peripheral oscillators. The underlying competition between divergence and realignment of the peripheral oscillators by a phase delaying perturbation from the hub remains identical.

The piece-wise linear approximation of the mapping approach can also be used to understand the clusters that are formed in the 5 node star system. Both experiments and computations produce the 1-cluster and 2-cluster (4-1 and 3-2) states only. The importance of the relationship between divergence and realignment has been discussed previously, Eq. (3.8). In Eq. (3.16), this relationship is reinforced as well as the role of the slope of the PRC (Z'). We have also referred to a restriction on the phase ϕ_1 of oscillator 1 that it must receive the perturbation from the hub before surpassing ϕ_{crit}, Eq. (3.10). The relationship shown in Eq. (3.8) shows that the difference in the firing times is inversely proportional to the slope of the PRC. Therefore, we can assume a restriction on the formation of a phase cluster, which is all oscillators that form a cluster must be between ϕ^* and ϕ_{crit} when they receive the perturbation from the hub. If an oscillator has a phase between 0 and ϕ^*, it is in the refractory regime of the PRC and the perturbation from the hub will not affect the phase of the oscillator. This is also true for the area of the PRC after ϕ_{crit} to 2π. We can see that the 1-cluster and 2-cluster (4-1 and 3-2) states are the only possible combinations that can form in this system.

3.6 Summary

This chapter describes the discovery and dynamics of a novel form of synchronization in a star network of photochemically coupled BZ chemical oscillators. Investigations into this system brings an important understanding of how functionality within network dynamics can arise through cooperative behavior of indirectly connected components. This understanding is significant and is in agreement with studies that revealed a mismatch between function and structure in natural networks [5–7]. The relaxation dynamics of chemical oscillators expand the possibility of novel synchronization occurring more broadly in natural networks composed of oscillators capable of similar dynamics. The novel synchronization seen in this chapter has many of the previously reported characteristics, such as requiring both intermediate coupling strengths and significant hub-peripheral node period mismatch. It differs, however, in both the relaxation nature of the oscillators and their dynamical response to coupling perturbations, as well as a predictable firing of both the hub and peripheral oscillators

Studies using star networks of SL oscillators have reported that the synchronizing signal leading to remote synchronization is transmitted via modulation of the amplitude of the hub oscillator. In contrast, the underlying mechanism for synchronization using BZ oscillators appears to be different from that previously reported. Examination of the firing patterns in simulations shows that the clustering of the peripheral oscillators arises via a delaying signal from the hub. This delaying signal can produce a significant change in the timing of an oscillator's firing time. Because of the monotonically decreasing PRC, this acts to slow the faster oscillators more than the slower oscillators and aligns the firing times of the oscillators, Eq. (3.9). A maximum allowed heterogeneity for the existence of synchronization is associated with the presence of the sharp transition in the PRC at ϕ_{crit}, Fig. 3.10. If the faster oscillator fires at a phase later than this, it is no longer delayed more than the slow oscillators and their phases diverge. At higher coupling strengths, we see larger heterogeneity allowed due to stronger realignment of the faster oscillators relative to the slower oscillators. The minimal piece-wise linear PRC used in our mapping approach satisfies the condition that the PRC is a monotonically decreasing function of phase in the region where the oscillators are perturbed. For this reason, the mapping approach is able to reproduce much of the behavior seen in the more complex BZ system.

References

1. G. B. Ermentrout, C. C. Chow, *Physiol. Behav.* **77**, 629 (2002).
2. H. Markram, Y. Toledo-Rodriguez M. Wang, A. Gupta, C. Silberberg G. Wu, *Nat. Rev. Neurosci.* **5**, 793 (2004).
3. S. Boccaletti, V. Latorab, Y. Morenod, M. Chavezf, D. U. Hwanga, *Phys. Rep.* **469**, 93 (2006).
4. A. Arenas, A. Daiz-Guilera, J. Kurths, Y. Moreno, C. Zhou, *Phys. Rep.* **469**, 93 (2008).
5. C. Vreeswijk, H. Sompolinsky, *Science* **274**, 1724 (1996).
6. E. Vega-Pons, S. Olivetti, P. Avesani, L. Dodero, A. Gozzi, A. Bifone, *Sci. Rep.* **7**, 1 (2017).
7. K. Batista-Garciá-Ramó, C. I. Fernández-Verdecia, *Behav. Sci.* **8**, 39 (2018).
8. D. Watts, S. Strogatz, *Nature* **393**, 440 (1998).
9. A. L. Barabási, R. Albert, *Science* **286**, 509 (1999).
10. B. Huberman, L. Adamic, *Nature* **401**, 131 (1999).
11. M. E. J. Newman, *J. Stat. Phys.* **101**, 819 (2000).
12. S. Strogatz, *Nature* **410**, 268 (2001).
13. R. Milo, S. Shen-Orr, S. Itzkovitz, N. Kastan, D. Chklovskii, U. Alon, *Science* **298**, 824 (2002).
14. R. Albert, A. L. Barabási, *Rev. Mod. Phys.* **74**, 47 (2002).
15. A. Bergner, M. Frasca, G. Sciuto, A. Buscarino, E. J. Ngamga, L. Fortuna, K. J., *Phys. Rev. E* **85**, 026208 (2012).
16. H. Jeong, B. Tombor, Z. N. Albert R. Oltvai, Barabási, *Nature* **407**, 651 (2000).

17. L. Stone, D. Simberloff, Y. Artzy-Randrup, *Comput. Biol.* **15**, 1 (2019).
18. V. Latora, V. Nicosia, M. Valencai, M. Chavez, D. Albert, *Phys. Rev. Lett.* **110**, 174102 (2013).
19. L. M. Pecora, F. Sorrentino, A. M. Hagerstrom, T. E. Murphy, R. Roy, *Nat. Commun.* **5**, 1 (2014).
20. L. V. Gambuzza, A. Cardillo, A. Fiasconaro, L. Fortuna, J. Gómez-Gardenñes, M. Frasca, *Chaos* **23**, 043103 (2013).
21. B. Karakaya, L. Minati, L. V. Gambuzza, M. Frasca, *Phys. Rev. E* **99**, 8200 (2019).
22. J. Lacerda, C. Freitas, E. Macau, *Appl. Math. Model.* **69**, 453 (2019).
23. V. Vlasov, A. Bifone, *Sci. Rep.* **7**, 1 (2017).
24. T. Chouzouris, A. Omelchenko, A. Zakharova, J. Hlinka, P. Jiruska, E. Schöll, *Chaos* **28**, 045112 (2018).
25. M. S. Santos, J. D. Szezech, F. S. Borges, K. C. Iarosz, I. L. Caldas, *Chaos. Sol. Fract.* **101**, 86 (2017).
26. C. Van Vreeswijk, H. Sompolinsky, *Science* **274**, 1724 (1996).
27. R. Toth, A. F. Taylor, M. R. Tinsley, *J. Phys. Chem. B* **110**, 10170 (2006).
28. M. R. Tinsley, A. F. Taylor, Z. Huang, K. Showalter, *Phys. Chem. Chem. Phys.* **13**, 17802 (2011).
29. S. Nkomo, M. R. Tinsley, K. Showalter, *Phys. Rev. Lett.* **110**, 244102 (2013).
30. S. Nkomo, M. R. Tinsley, K. Showalter, *Chaos* **26**, 094826 (2016).
31. D. Yengi, M. R. Tinsley, K. Showalter, *Chaos* **28**, 045114–1 (2018).
32. M. R. Tinsley, S. Nkomo, K. Showalter, *Nat. Phys.* **8**, 662 (2012).
33. A. F. Taylor, P. Kapetanopoulos, B. J. Whitaker, T. Toth, L. Bull, M. Tinsley, *Phys. Rev. Lett.* **100**, 214101–1 (2008).
34. A. M. Zhabotinsky, F. Buchholtz, A. B. Kiyatkin, I. R. Epstein, *J. Phys. Chem.* **97**, 7578 (1993).

Chapter 4

Extreme Events in Coupled Chemical Oscillators

4.1 Introduction

This chapter will discuss and describe the occurrence of extreme events (EE) in an excitable system using the 4-variable Oregonator model. Many biological, natural, social, and financial systems are capable of generating large intermittent deviations from their normal dynamics [1, 2]. Natural events such as earthquakes, tsunamis, rouge waves, algal blooms, or extreme weather events can all cause large scale damage [1, 3–5]. Sudden bursts of electrical activity in the brain, known as epileptic seizures, can be devastating to people who suffer from them [6]. Other examples of these events include large-scale failures in the power grid [7], stock market crashes [8], social unrest [9], and wars [10]. Recent literature has provided a framework to define what qualifies as extreme events [11–14]. The events are described as rare, aperiodic in occurrence, and have significant consequences on the system. The aperiodic nature of these events makes predictions and interventions difficult or nearly impossible. This makes the development of models and experimental methods to study these events important to understanding the underlying mechanisms.

Previous investigations have modeled excitable-oscillatory networks of FitzHugh-Nagumo (FHN) oscillators to demonstrate the emergence of extreme events in a coupled system [11–14]. FitzHugh-Nagumo (FHN) oscillators are a widely studied excitable system, which qualitatively captures the dynamics of neuronal firing using the following differential equations [15, 16].

$$\frac{dx_i}{dt} = x_i(a_i - x_i)(x_i - 1) - y_i \tag{4.1}$$

$$\frac{dy_i}{dt} = b_i x_i - c_i y_i \tag{4.2}$$

Here the activation variable x_i represents the membrane voltage, which is diminished over time by the recovery variable y_i with a_i, b_i, and c_i as internal parameters. Integrating these equations produces a spike train of relaxation oscillations with a constant period, Fig. 4.1.

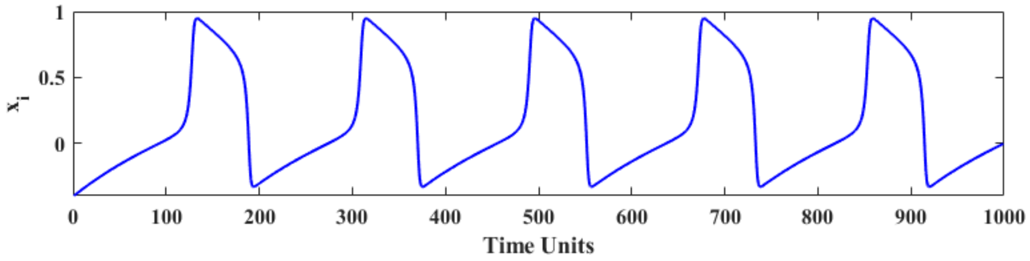

(a) Oscillations in the variable X

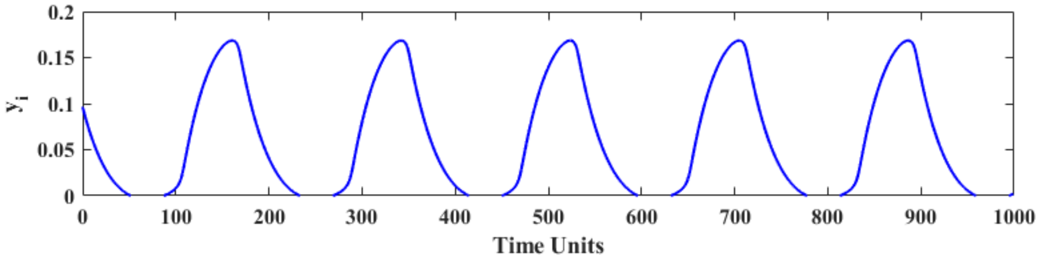

(b) Oscillations in the variable Y

Figure 4.1. (a) Time series in the activator variable X, (b) the recover variable Y, illustrating the relaxation oscillations and constant period of each variable with time. For this simulation, the parameters are set to a_i = -0.0265, b_i = 0.0065, and c_i = 0.02. Time is dimensionless in this simulation.

An investigation completed by Ansmann et al. showed the emergence of extreme events in coupled FHN systems [11]. The coupled system is comprised of two homogeneous FHN oscillators x_i and x_j. The predominant behavior in the coupled system, for both oscillators, are irregular small amplitude oscillations that have maximum and minimum $x(t)$ values between 0.34 and -0.2, respectively. However, the system will exhibit large deviations from the normal dynamics with large amplitude oscillations that are roughly six times larger than the maxima of the small oscillations, Fig. 4.2(a). The authors concluded that in the 2 oscillator system

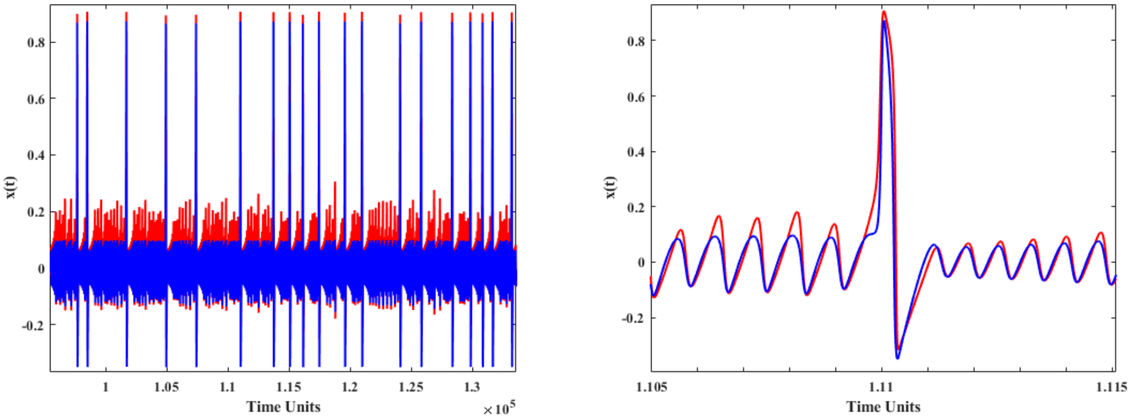

(a) Temporal oscillations in FHN oscillators (b) Enlargement from (a)

Figure 4.2. (a)Temporal oscillations in $x(t)$ exhibiting aperiodic large deviations from normal dynamics. (b) An enlargement of a large amplitude oscillation in (a).

when one of the oscillators becomes excited into a large excursion it recruits the other oscillator and generates an extreme event. This recruitment behavior is shown in Fig. 4.2(b). The red oscillator begins a large excursion at 1.109×10^{-5}, which is followed by the blue oscillator. The behavior was only reported in the two oscillator system for a single coupling value of 1.28×10^{-3}. For coupling less than 1.28×10^{-3}, only small amplitude oscillations are observed, and for coupling above 1.28×10^{-3}, periodic mixed-mode oscillations are the dominate behavior. The aperiodic behavior was reported to be due to a saddle focus at the origin. At a coupling value of 1.28×10^{-3}, a small channel-like structure exists in state space such that the trajectory can escape and undergo a large excursion before returning to the origin. The authors noted the apparent chaotic behavior of the system was due to the width of this channel-like structure. The width of this channel is dependent on the systems parameters and at coupling above 1.28×10^{-3} extreme events will no longer be observed.

Further investigation into this system was conducted by Saha et al. using time-delayed coupling between two FHN oscillators [12]. This study focused on the effects of single and multiple time-delayed signals on the emergence of extreme events. For a single time delay, the authors report only periodic mixed-mode oscillations and no extreme events are observed. The authors did observe a change in the limit cycles by varying the time delay, and that change was attributed to a change in the stability of the attractor. In a three-dimensional representation of the trajectories of coupled oscillators, the invariant synchronization manifold is defined where

$x_1 = x_2$ at y_1. This creates a plane of synchronization where both oscillators are in-phase with each other while on the manifold. At constant coupling strength and a delay equal to 80, the limit cycle on the manifold was found to be attracting and contains the only attractor in the system. For this case, all nearby trajectories will converge to the limit cycle and execute several small amplitude oscillations before being ejected into a single large excursion. Both the small and large amplitude oscillations are on the manifold and therefore the oscillators are in-phase, Fig. 4.3. However, they are not considered extreme events due to the periodic pattern they produce. When the delay is decreased to 70, the limit cycle on the manifold becomes unstable.

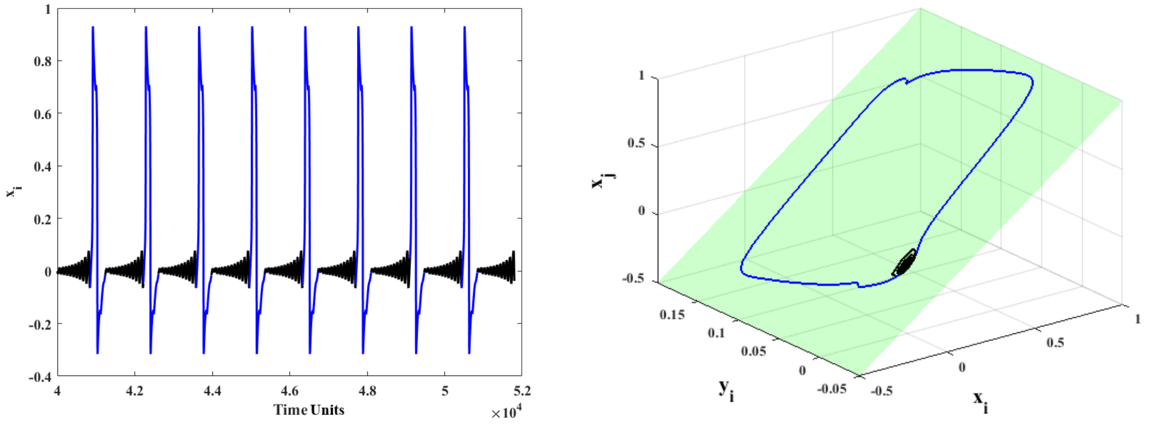

(a) Mixed-mode in-phase oscillations

(b) 3D trajectory

Figure 4.3. (a) Mixed-mode in-phase oscillations in $x(t)$ exhibiting periodic large deviations from normal dynamics. (b) 3D representation of trajectory. The light green plane is the invariant synchronization manifold. The black line is the small amplitude oscillations and the blue line is the large amplitude oscillations.

A new limit cycle gains stability that is located off the manifold, Fig. 4.4. Trajectories starting off the manifold will spiral toward the manifold along the new limit cycle until they are ejected off into a large excursion. Trajectories that start on the manifold stay on the manifold and will perform only small amplitude oscillations on the manifold. However, the small amplitude limit cycle is unstable, as any perturbations will cause the trajectories to converge to the stable limit cycle off the manifold. Here again, the large excursions are not considered extreme events due to the periodic nature of the events. The stability of the attractors was reported to play a role in the type of large oscillation. If the limit cycle on the manifold is stable, then only in-phase oscillations are observed. When the limit cycle on the manifold is unstable, trajectories starting off the manifold only produce out-of-phase events. The authors did not report the emergence of extreme events using a single time delay.

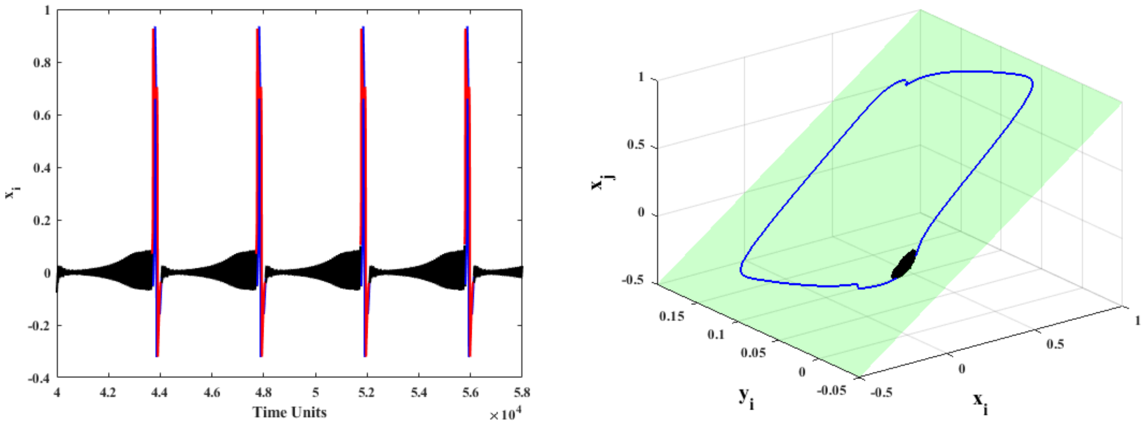

(a) Out-of-phase mixed-mode oscillations (b) 3D trajectory

Figure 4.4. (a) Out-of-phase mixed-mode oscillations in $x(t)$ exhibiting periodic large deviations from normal dynamics. (b) 3D representation of trajectory. The light green plane is the invariant synchronization manifold. The black line is the small amplitude oscillations and the red line is the large amplitude oscillations.

To further investigate the dynamics of this system, Saha et al. added a second coupling term with a unique delay time. This two-delay system will combine the in-phase and out-of-phase delay times. The authors set the coupling strength for the in-phase delay to be constant at 0.005 and varied the coupling strength for the out-of-phase delay. When the second coupling strength is above 0.0058, the attractor on the manifold is unstable and the trajectories are similar to the single time-delay system with a delay of 70 with out-of-phase dynamics. At coupling strengths less than 0.0048, the system is qualitatively the single time-delay system with a delay of 80 producing in-phase events. However, when the coupling strength is between 0.0048 and 0.0058, the authors report several changes to the system. The unstable limit cycle on the manifold gains transverse stability, and remains unstable in the direction of the manifold, creating a saddle point. This attractor becomes chaotic via a period-adding cascade. Since the manifold is now transversely stable, trajectories starting off the manifold are attracted to it. As a trajectory approaches the saddle point, it executes small amplitude oscillations until it is ejected away in an out-of-phase event. Trajectories may also be ejected along the manifold as an in-phase event. Because the attractor is unstable along the manifold, the trajectory will leave the manifold as it again approaches the saddle point along the stable direction. This mixed behavior of in-phase and out-of-phase events can be seen in Fig. 4.5. Finally, Saha et al. demonstrated that there

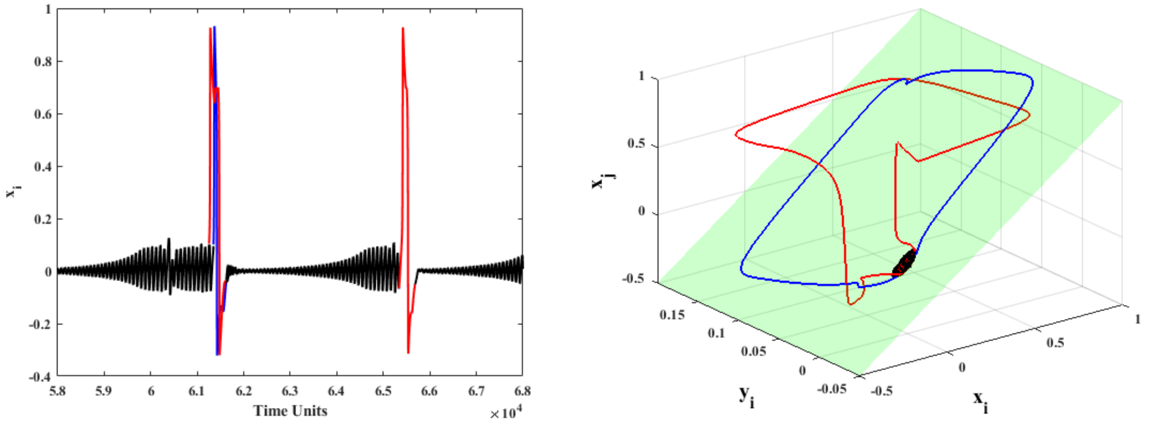

(a) In-phase and out-of-phase oscillations

(b) 3D trajectory

Figure 4.5. (a) In-phase and out-of-phase mixed-mode oscillations in $x(t)$ due to changes in stability in the system. (b) 3D representation of trajectory. The light green plane is the invariant synchronization manifold. The black line is the small amplitude oscillations and blue and red lines are large amplitude in-phase and out-of-phase oscillations, respectively.

is a fraction of parameter space where the timing of the events become irregularly spaced, Fig. 4.6(a). The aperiodic emergence of the events follow a Poisson-like distribution, Fig 4.6(b). Therefore, the events can be considered extreme events because of the rarity of their emergence. The reported rate of events found by Saha et al. was 1.15×10^{-4} events per time unit.

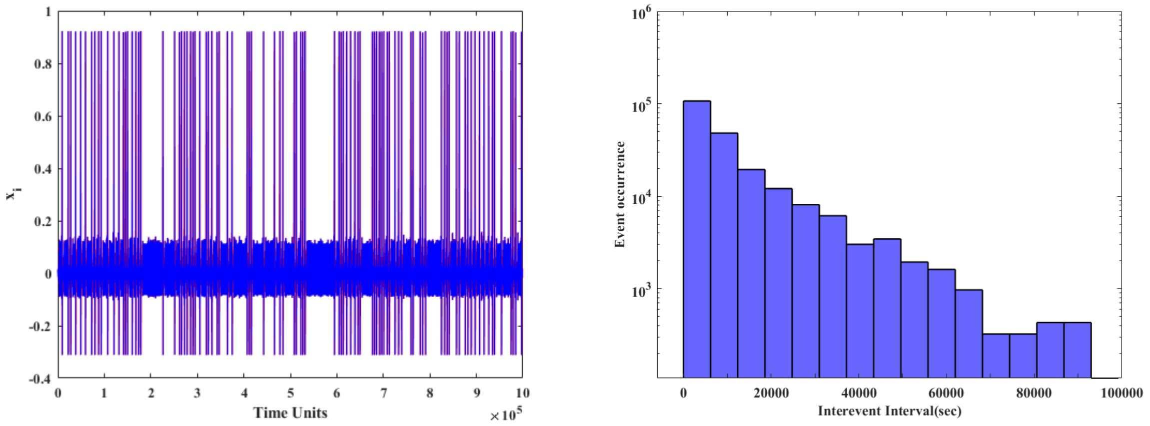

(a) Time series showing extreme events

(b) Possion-like Distribution

Figure 4.6. (a) Partial time series of two FHN oscillators using 2 time-delayed signals exhibiting extreme events. (b) Histogram showing Poisson-like distribution for the full time series in (a).

4.2 Extreme Events using the Oregonator Model

One shortcoming of the FHN system is the lack of an equivalent experimental system to observe the emergence of extreme events in a real-world system. To address this, we use the four-variable modified Oregonator to explore extreme events, which is a model based on the Belousov-Zhabotinsky (BZ) reaction.

Both FHN and BZ oscillators are relaxation oscillators that demonstrate similar dynamics. Both the FHN [11–13, 17] and the Oregonator [18–20] are capable of displaying mixed-mode oscillations. A time series showing these mixed-mode oscillations in the Oregonator model were shown in Chapter 2, Fig. 2.2(d). The mixed-mode oscillations in the Oregonator are due to the presence of a subcritical-Hopf bifurcation in the vicinity of the reduced steady state. Shown in Fig. 4.7(a), the sub-Hopf bifurcation is characterized by a stable steady state (SSS), solid line, that acts as a focus, where small amplitude oscillations can occur. As the trajectory moves to the left, the steady state becomes unstable (USS), shown as a broken line. The trajectories will begin unwinding as the oscillations grow until a large amplitude oscillation occurs. This unwinding behavior is shown in the limit cycle of an oscillation in Fig. 4.7(b). Since the 4-variable Oregonator model is based on the kinetics of the BZ reaction and possess similar dynamics to the FHN, it makes an ideal candidate to explore extreme events. The investigation

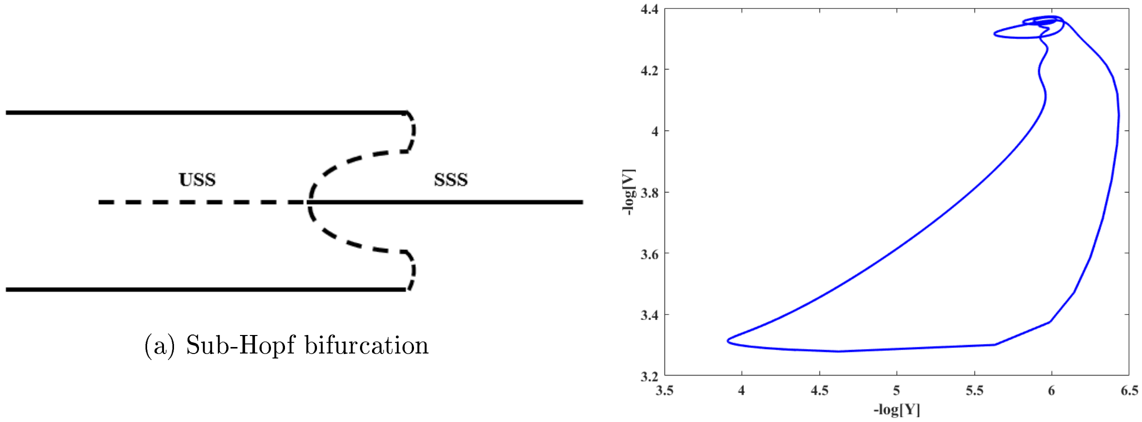

(a) Sub-Hopf bifurcation

(b) Limit cycle in the Y and V variable

Figure 4.7. (a) Sub-Hopf bifurcation showing a stable steady state, which can support small amplitude oscillations, and an unstable steady state where full amplitude oscillations are observed. A limit cycle of the variable V (bromous acid) and Y (bromide) that shows the unwinding behavior as the trajectory moves from the stable to unstable steady state.

discussed in this chapter will consider three different systems. All three systems will consist of two bidirectionally coupled oscillators coupled using a coupling term omega. The first system will not use time delays in the coupling terms. The second system will use a single time-delayed signal and the final system will contain double time-delayed signals. Since the FHN oscillators used by Saha et al. show an inhibitory response to a perturbation, Eqs. (2.30)-(2.33), will be modified to account for this inhibitory response, Eqs. (4.3)-(4.7). The parameters values and rate constants used in all simulations are listed in Table 4.1.

$$\frac{dx_i}{dt} = k_1AY_i - k_2X_iY_i + k_3AX_i - 2k_4X_i^2 - k_f(X_i - X_{sur}), \tag{4.3}$$

$$\frac{dy_i}{dt} = -k_1AY_i - k_2X_iY_i + f_ik_3Z_i - k_f(Y_i - Y_{sur}) + p_1(V_i)\Phi + \Omega, \tag{4.4}$$

$$\frac{dz_i}{dt} = 2k_3AX_i - k_5Z_i + (p_1(V_i) + \Omega, \tag{4.5}$$

$$\frac{dv_i}{dt} = k_1AY_i + 2k_2X_iY_i + k_4X_i^2 - k_6V_i - k_f(V_i - V_{sur}) - p_1(V_i)\Phi - \Omega. \tag{4.6}$$

Here, k_f is used to represent the exchange between the oscillator and the surrounding solution. The coupling term Ω is

$$\Omega_i = M_1(Z_j(t - \tau_1) - Z_i(t)) + M_2(Z_j(t - \tau_2) - Z_i(t)), \tag{4.7}$$

where M_1 and M_2 are the coupling strengths, Z represent the oxidized catalyst of oscillator i and j, and τ_1 and τ_2 are the time delays.

Table 4.1. Parameter Values for Oregonator Model [19, 20]

Parameter	Value	Variable	Value
A	6.0×10^{-2}	k_1	$2H^2$
H	4.0×10^{-1}	k_2	3.0×10^6 H
Φ	4.66×10^{-5}	k_3	42H
k_f	2.0×10^{-2}	k_4	3.0×10^3
f	0.70	k_5	2.013×10^{-1}
X_{sur}	1.0×10^{-6}	$\frac{k_{-L0}}{k_{L1}}$	3.3
Y_{sur}	3.0×10^{-5}		
V_{sur}	1.0×10^{-6}	$\frac{k_{L2}}{k_{L1}}$	5.54

4.3 Instantaneous Coupling

In this section we explore the computational results of two coupled oscillators that exhibit small amplitude oscillations with an average amplitude of 3.9×10^{-6}. Since there are no time delays in this system, Eq. (4.7) is simplified to

$$\Omega_i = M(Z_j(t) - Z_i(t)). \tag{4.8}$$

To investigate the dynamics of this system, we will vary the coupling strength from 0.05 to 14.9 using Eq. (4.8). Below 0.05 the coupling is too weak to have any noticeable effects on the oscillators, and above 14.9 the system becomes non-oscillatory. First, two homogeneous oscillators with identical initial conditions are coupled according to Eq. (4.8). For this range of coupling strengths, the trajectories are observed to converge to a small amplitude limit cycle. This limit cycle (black line) can be observed using a 3D representation of the trajectories in the Z_i, Z_j and Y_i terms, Fig. 4.8. However, when the initial conditions are such that the oscillators do not start in phase, the dynamics of the system vary greatly. Applying a coupling strength from 0.05 to 8.1, again the small amplitude limit cycle seen in Fig. 4.8 is the only attractor in the system and all trajectories will eventually converge to it. At a coupling strength of 8.2, this limit cycle loses it stability and trajectories will no longer converge to it. Another limit

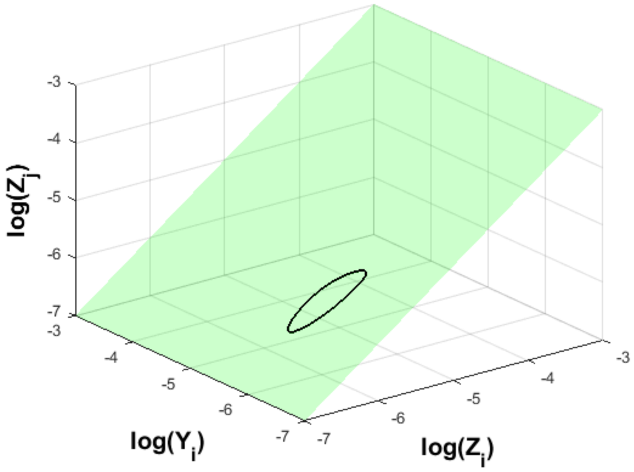

Figure 4.8. A 3D representation of Z_i, Z_j and Y_i for a pair of identical coupled oscillators with the same initial conditions. The limit cycle, black line, is on the synchronization manifold. Trajectories will converge to this limit cycle for all identical initial conditions.

cycle off the manifold gains stability and is the only stable attractor in the system, which can be seen in Fig. 4.9 as a red line. As we increase coupling beyond 8.1 the system goes through a period-doubling cascade leading to chaotic behavior in the amplitude of the oscillators at a coupling strength of 9.2, Fig. 4.10(a). To demonstrate the behavior is chaotic, we can produce a next return map, which plots the next peak amplitude of an oscillators Z_{n+1} verses the current peak amplitude Z_n, Fig 4.10(b). If the behavior was periodic we would expect to observe clusters form, but we can clearly see no clusters are formed. As we continue to increase coupling to 11, the system begins to display large amplitude oscillations. These large oscillations have amplitude from 3.8×10^{-4} to 4.0×10^{-4}, and are roughly 100 times larger than the smaller oscillations observed in the system, Fig 4.11(a). The 3D projection of the trajectories show that both small and large oscillations are out-of-phase, Fig. 4.11(b) These large oscillations represent large deviations from normal dynamics, which is one part of our definition of an extreme event. To determine if the criteria of rare and irregular is satisfied, we measure the time between large events referred to as the interevent interval. When the interevent intervals are plotted in a histogram, they fit a Poisson-like distribution, which will allow for the calculation of a rate of appearance, Fig. 4.12. The rate at which the large events occur was calculated to be 3.24×10^{-5} events per time unit. With this low rate of occurrence and aperiodic emergence,

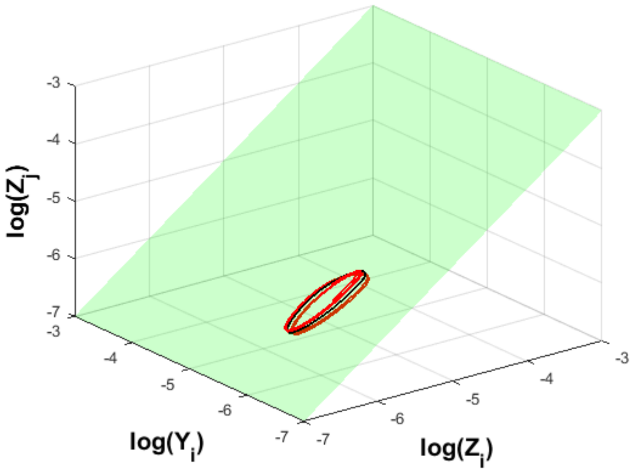

Figure 4.9. A 3D representation of Z_i, Z_j and Y_i for a pair of identical coupled oscillators with different initial conditions. The unstable limit cycle, black line, is on the synchronization manifold. The out-of-phase trajectories will now converge to the new attractor in the system, which is shown by the red lines.

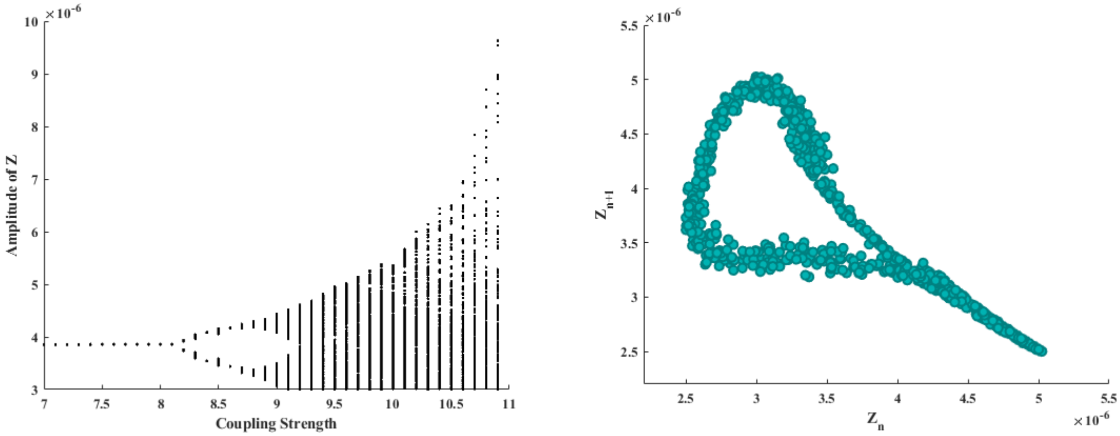

(a) Bifurcation diagram

(b) Next return map

Figure 4.10. (a) Bifurcation diagram showing the period-doubling cascade with increasing coupling strength leading to chaotic behavior. (b) Next return map for a single oscillator showing the lack of grouping that periodic behavior would display.

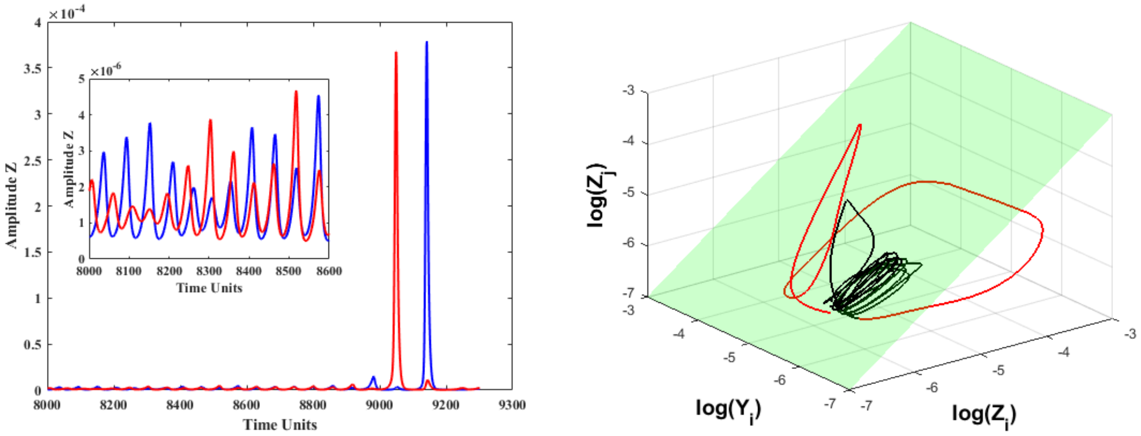

(a) Time series

(b) 3D projection

Figure 4.11. A time series showing the emergence of large amplitude oscillations in the system with a coupling strength of 11. The inset shows a close-up of the small amplitude oscillations of a single oscillator. (b) 3D representation of the trajectories for two coupled oscillators. The light green plane is the invariant synchronization manifold. The black line represents the small out-of-phase oscillations, and the red line is the out-of-phase large amplitude oscillations.

the system meets the criteria of extreme events. As we increase the coupling strength to 11.1, the interevent intervals still fit a Poisson-like distribution; however, the rate of occurrence has risen to 2.91×10^{-4}, Fig. 4.13(a). As the coupling is increased again to 11.2 and 11.3, the rates increase slightly to 3.91×10^{-4} and 3.80×10^{-4}, respectively, Fig 4.13(b) and 4.13(c). This is a significant increase in the rate, but the systems still meets all three requirements for extreme events. Increasing the coupling to 11.4 changes the nature of the attractor, as it is no longer

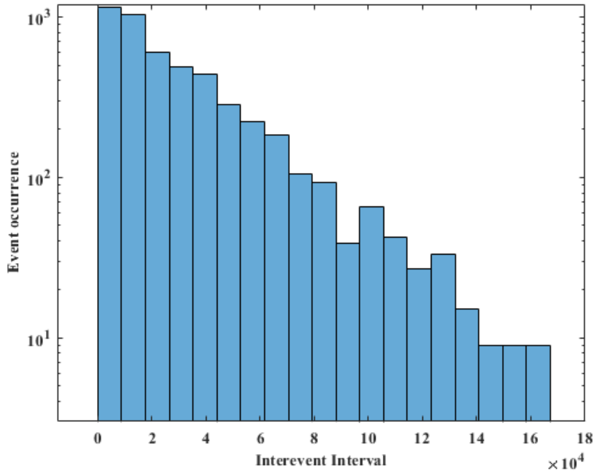

Figure 4.12. A Poisson-like distribution for two coupled oscillators using a coupling strength of 11. There are 4864 total events over a 150 million time units simulation, which yields a rate of 3.24×10^{-5} events per time unit.

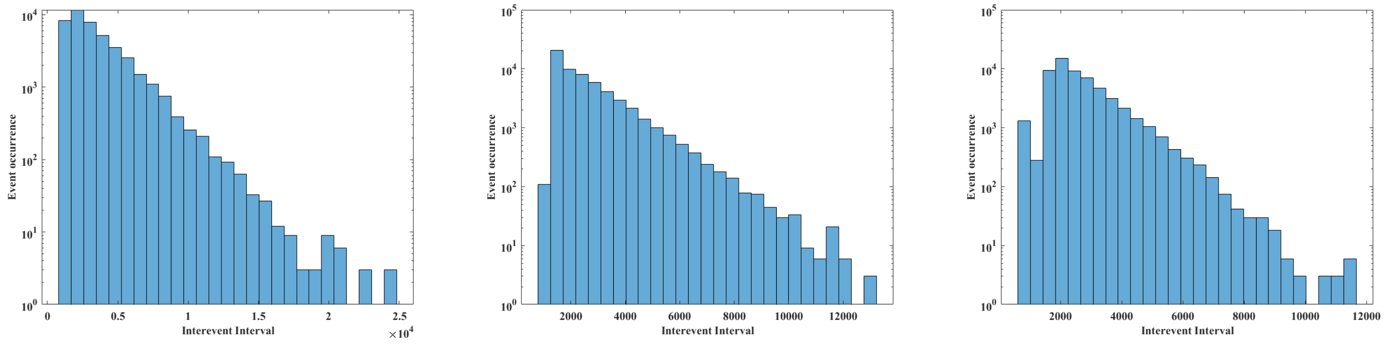

(a) Coupling 11.1

(b) Coupling 11.2

(c) Coupling 11.3

Figure 4.13. (a) Poisson distribution for a coupling strength of 11.1. The total number events was 43650 with a rate of 2.91×10^{-4}. (b) A coupling strength of 11.2 produced 58662 total events with a rate of 3.91×10^{-4}. Using a coupling strength of 11.3 produces 56934 events at a rate of 3.81×10^{-4}. All three simulations where completed over a length of 150 million time units.

chaotic and the systems settles into periodic mixed-mode oscillations, Fig. 4.14. This behavior continues until a coupling strength of 14.9 is reached and the system becomes non-oscillatory. The lack of aperiodicity in the system excludes the large oscillations from being defined as extreme events.

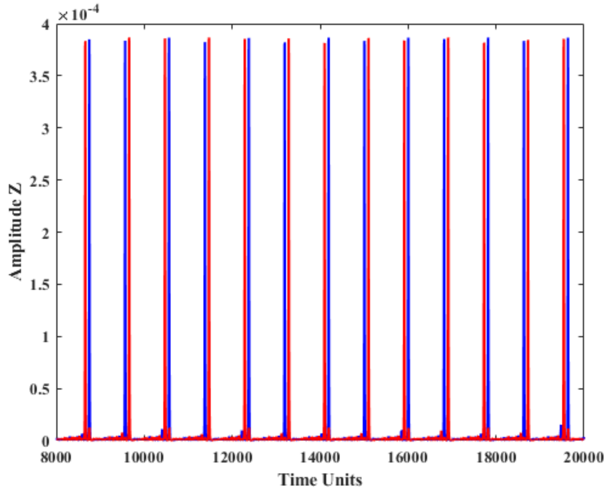

Figure 4.14. Mixed-mode oscillations at a coupling strength of 11.4. The large oscillations are periodic in occurrence.

4.4 Single Time Delay Coupling

We now explore the computational results of two coupled oscillators with a time delay in the coupling term, Eq. (4.9).

$$\Omega_i = M(Z_j(t-\tau) - Z_i(t)). \tag{4.9}$$

Simulations used the same parameters as the no-delay system from Table 4.1. For all simulations, the coupling strength will be held constant at a value of 10, where a chaotic attractor was found in the no-delay system. The delay will be varied from 1 to 58 to observe the effect of delay on the system. As discussed earlier, using a coupling strength of 10 with no time delay results in the system producing chaotic small-amplitude oscillations, Fig. 4.9. When a time delay between 1 and 9 is used, periodic out-of-phase oscillations are now observed, Fig 4.15. The introduction of the time delay has resulted in a change in the nature of the attractor. The new limit cycle contains large amplitude oscillations and is not chaotic. As we increase the time delay to 10, another change occurs in this mixed-mode attractor. The oscillations are now in-phase for both large and small oscillations, Fig. 4.16. The mixed-mode attractor is now on the synchronization manifold for all points. This in-phase behavior continues until a delay of 14 is used. Here the limit cycle becomes complex in that it contains both out-of-phase, Fig 4.17 (red line), and approximately in-phase oscillations, Fig 4.17 (blue line). The occurrence of the large amplitude

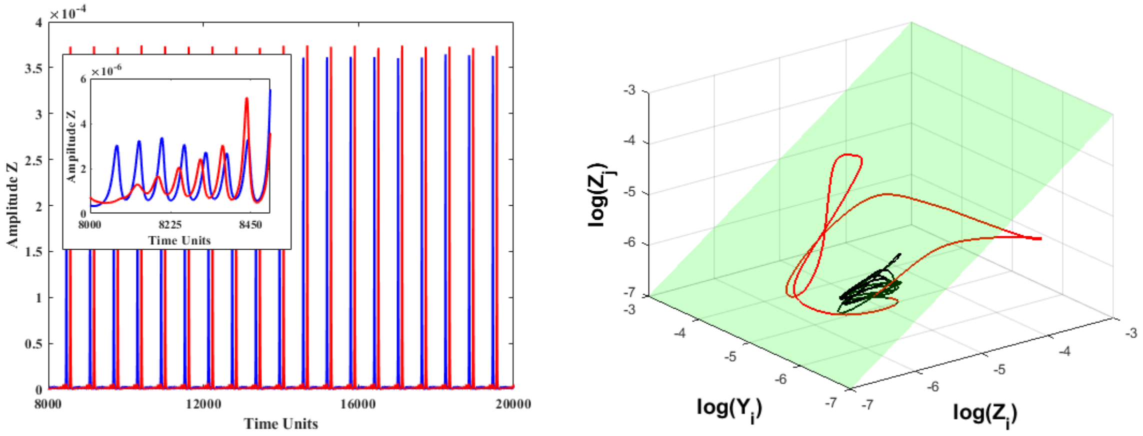

(a) Out-of-phase mixed-mode oscillations

(b) 3D trajectory

Figure 4.15. (a) Out-of-phase mixed-mode oscillations exhibiting periodic large deviations from normal dynamics. (b) 3D representation of trajectory. The light green plane is the invariant synchronization manifold. The black line is the small amplitude oscillations and the red line is the large amplitude oscillations.

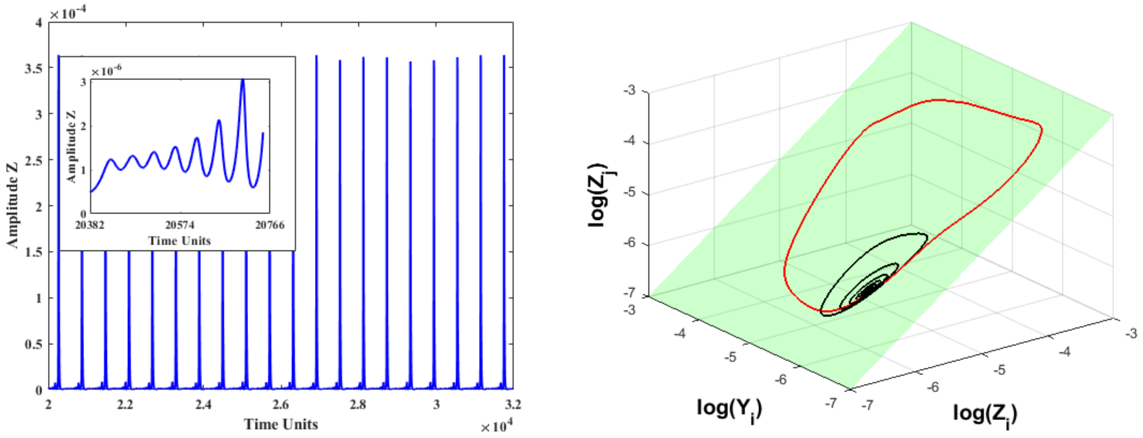

(a) In-phase mixed-mode oscillations

(b) 3D trajectory

Figure 4.16. (a) In-phase mixed-mode oscillations exhibiting periodic large deviations from normal dynamics. (b) 3D representation of trajectory. The light green plane is the invariant synchronization manifold. The black line is the small amplitude oscillations and the red line is the large amplitude oscillations.

oscillations are fairly regular in occurrence; however, the pattern of out-of-phase to in-phase excursions is irregular. When the time delay reaches 20 the limit cycle again changes in form to a single small oscillation followed by a large oscillation. When oscillator i is producing a large amplitude oscillation, oscillator j is producing a small amplitude oscillation. When the next firing occurs , oscillator j will produce a large oscillation as oscillator i produces a small oscillation, Fig. 4.18. This behavior continues until a delay time of 58. We do not continue to

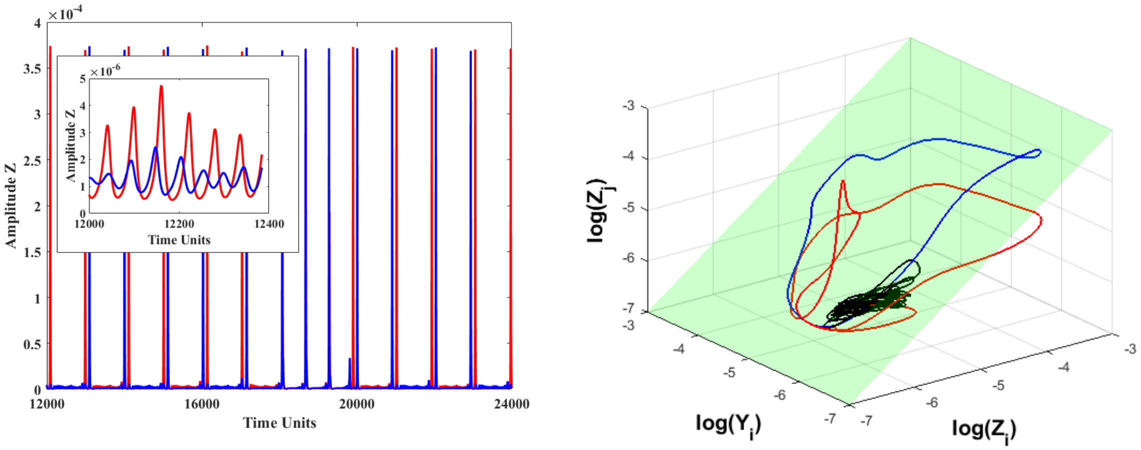

(a) Out-of-phase and in-phase mixed-mode oscillations

(b) 3D trajectory

Figure 4.17. (a) Out-of-phase and in-phase mixed-mode oscillations exhibiting regular large deviations from normal dynamics. (b) 3D representation of trajectory. The light green plane is the invariant synchronization manifold. The black line is the small amplitude oscillations and the red line is the large amplitude out-of-phase oscillations. The blue line corresponds to the in-phase large amplitude oscillations.

increase the delay past 58 because this is the natural period of the oscillators. The addition of a

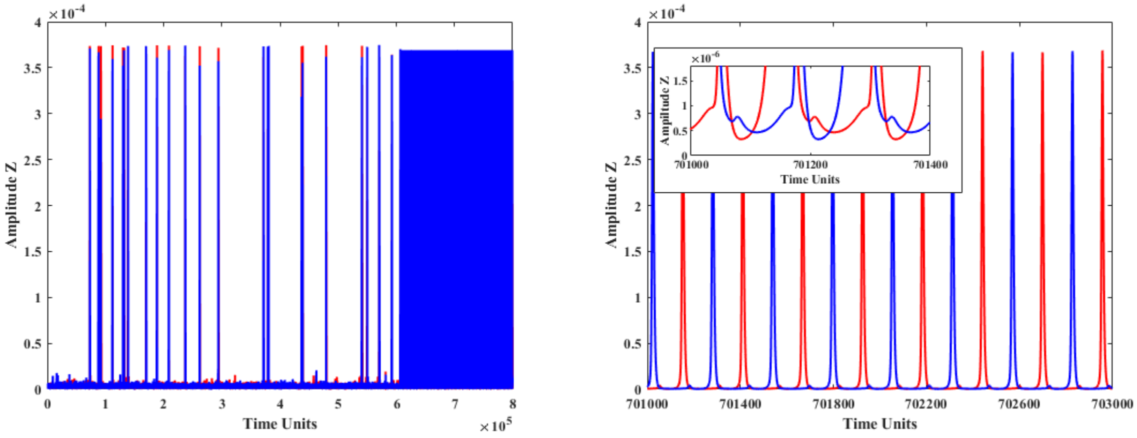

(a) Time series of single large and small oscillation

(b) Enlargement of (a)

Figure 4.18. (a) Mixed-mode oscillations with a time-delay of 21. A short transient followed by periodic alternating large oscillations. (b) A close up of (a) showing the periodic behavior. The inset shows the small oscillation that appear between large excursions.

time delay to the system has changed the attractor from a small amplitude chaotic attractor to a mixed-mode periodic one. This periodicity excludes all of the observed behaviors from being defined as extreme events. However, at a time delay of 21, there is a transient behavior that appears to be aperiodic in nature, Fig. 4.18(a).

4.5 Double Time-Delay Coupling

A second time delay was added to the system using Eq (4.7) in an effort to take advantage of the aperiodic dynamics found in the single time-delay system at $\tau = 25$. Again using the same parameters from the previous two systems, Table 4.1. In previous work by Saha et al., the coupling strength used in the single time-delay system was split between the two delays. We will also use this strategy in our system. The first delay, $\tau_1 = 21$, will be given a coupling strength of $\mathrm{M}_1 = 7.4$. The second delay chosen, $\tau_2 = 11$, corresponds to a delay that produces only in-phase oscillations. The coupling strength for this delay is $\mathrm{M}_2 = 2.3$. Therefore, $\mathrm{M}_1 + \mathrm{M}_2 = 9.7$, approximately the value of the coupling value used in the signal delay value of 10. A simulation was completed using these values for a length of 400 million time steps. A small fraction of the time series is shown to illustrate the aperiodic apperance of the large oscillations, Fig. 4.18(a). A close up of this time series reveals that this system is producing both in-phase and out-of-phase events, unlike the single time-delay system that only produced out-of-phase events. To further illustrate the in-phase and out-of-phase behavior, a 3D projection of the time series shown in Fig. 4.18(b) can be created, Fig. 4.19. To find the rate of occurrence for the large oscillations, the interevent intervals are calculated and fitted with a Poisson-like distribution. The occurrence rate was calculated to be 1.12×10^{-4}events per time unit. This

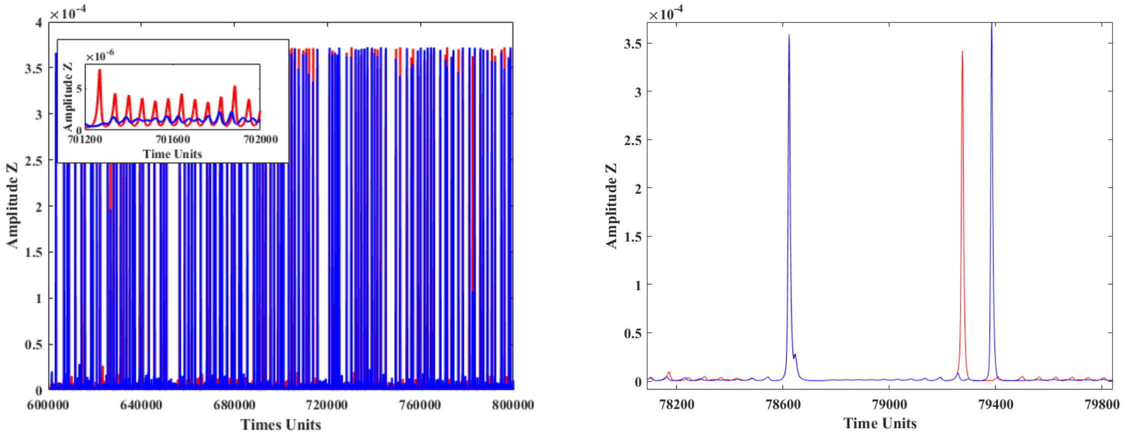

(a) Time series extreme events

(b) Enlargement of (a)

Figure 4.19. (a) Section of a time series for the two delay system. The aperiodic behavior of the large oscillations can be observed, meeting one requirement of extreme events. The inset shows the small amplitude oscillations that are considered the normal behavior. (b) A close up of (a) showing the large amplitude oscillations occur as both in-phase and out-of-phase oscillations.

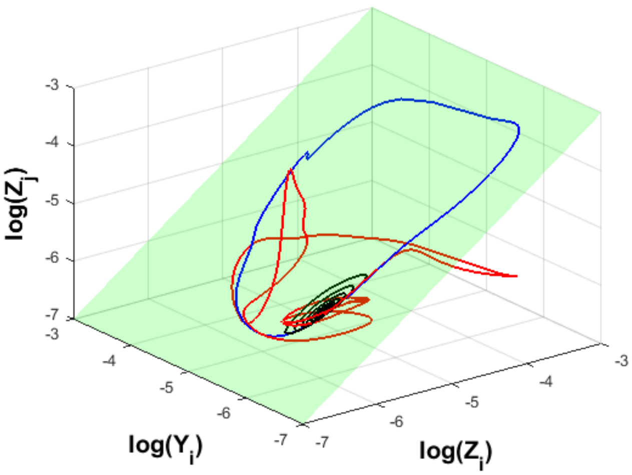

Figure 4.20. A 3d projection of the time series in Fig. 4.18(a). The black line shows the small amplitude oscillations close to the origin. The blue line depicts the large in-phase oscillation. The red line is the large out-of-phase oscillation and the small oscillations as it spirals back toward the origin.

small rate of occurrence satisfies the final requirement that the large deviations are rare.

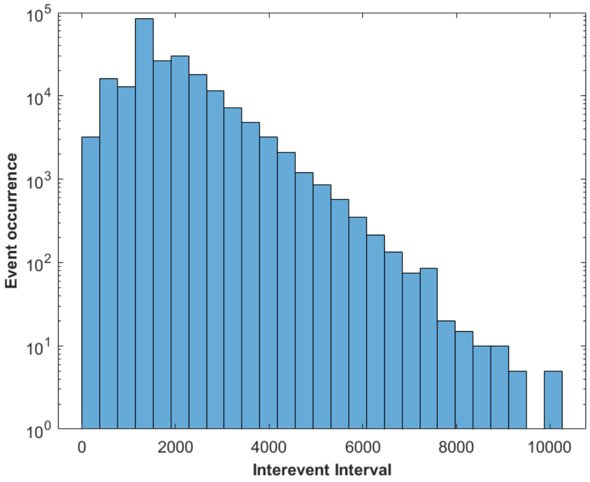

Figure 4.21. Poisson distribution for the two delay system. The simulation produced 44672 large events over 400 million time units yielding a rate of 1.12×10^{-4} events per time unit.

4.6 Summary

We have observed extreme events in both the instantaneous and the two delay system. In the case of the instantaneous system, the coupling strength was varied. At low coupling strength, the stable attractor in the system was an in-phase small amplitude limit cycle. As the coupling strength was increased, this limit cycle became unstable and a new small amplitude out-of-phase limit cycle gained stability. On increasing the coupling strength, the limit cycle underwent a cascade of period doubling bifurcations, which is seen in Fig. 4.10(a). When the coupling was increased to 9.2, the attractor became chaotic. This chaotic behavior is characterized using a next return map, Fig. 4.10(b). At this value of delay, the amplitude of the oscillations are aperiodic and do not exceed 5.0×10^{-6}. When a coupling strength of 11 is reached, large oscillations with an average amplitude of 3.65×10^{-4} are observed. These large oscillations are roughly 100 times the size of the small amplitude oscillations, which are considered the normal dynamics of the system. By increasing the coupling strength, the limit cycle now has these large trajectories available. Producing large deviations from normal dynamics is the first criteria for extreme events. The next criteria is that the large deviations are irregular. This is also satisfied since the attractor is chaotic and spends more time close to the origin undergoing small oscillations. It is much more likely that the oscillator will stay close to the origin and complete only small oscillations. However, due to the chaotic behavior, the oscillator is intermittently ejected onto a large trajectory and completes a large oscillation. The final criteria is the events must be rare and this can be shown with a Poisson distribution, Fig 4.12. The rate of occurrence was calculated to be 3.24×10^{-5}, satisfying the final requirement. The system continued to produce extreme events as coupling was increased to 11.3, Fig. 4.13. When the coupling strength reached 11.4, the chaotic attractor loses its stability and a mixed-mode limit cycle gains stability. This new mixed-mode attractor is periodic and no longer satisfies the definition of an extreme event.

In the single time-delay system, a coupling strength of M = 10 was used that would have produced a small amplitude chaotic attractor in the instantaneous system. However, the introduction of a time delay was sufficient to produce mixed-mode oscillations. Depending on the time delay used, several different behaviors were observed. Each behavior was discussed previously, but the two behaviors of interest are the in-phase mixed mode at $10 \geq \tau \leq 13$ and the switching between small and large oscillations at $20 \geq \tau \leq 58$. During the in-phase mixed mode behavior at $\tau = 11$, the limit cycle on the synchronization manifold is the only stable attractor in the system, and the trajectories are in-phase for all time. The next time delay of interest is $\tau = 25$, but not for the dominate behavior, but for the transient aperiodic behavior.

The transient behavior produces aperiodic small and large oscillations but is not stable. Due to the short lived nature of this behavior, we do not consider it is an example of extreme events by itself. Therefore, in the parameter space explored here no extreme events are observed.

When two time delays are used, as described earlier, we can observe extreme events in the system. The delay of $\tau = 11$ produces an attractor located on the manifold. Nearby is another attractor produced by the delay $\tau = 25$, located just off the manifold. The Oregonator model is an example of an excitable system. For small perturbations away from the limit cycle, the return is monotonic. However, when a perturbation is large enough, the trajectory can get close enough to another attractor and undergo different dynamics. To understand how this two delay system is producing extreme events, we will examine a section of the time series. In Fig. 4.22, we can observe both in-phase and out-of-phase events occurring. When we examine an in-phase event in more detail, we can explain the behavior produced. Figure 4.23 shows the large in-phase event around time 5000 and the small amplitude oscillations just before and after the large event. We can observe that the two oscillators are clearly out-of-phase at time 4600. They begin to approach the stable limit cycle present on the manifold. Approximately at time 5000, the trajectory reaches this limit cycle and the oscillators are now in-phase. As expected, they perform a large in-phase excursion. In the single time-delay system, we would predict that the system would now stay on this attractor. As we can see at approximately time 5650, the

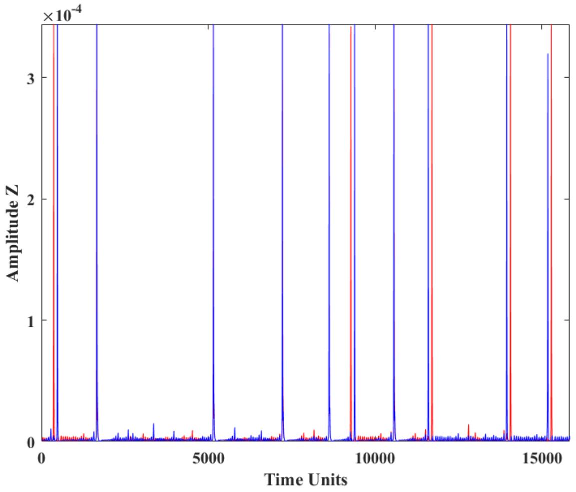

Figure 4.22. Section of a time series showing both in-phase and out-of-phase extreme events. The in-phase events appear as blue lines without being paired with a red line. This is due to the overlap of the trajectories where the red oscillation can not be observed.

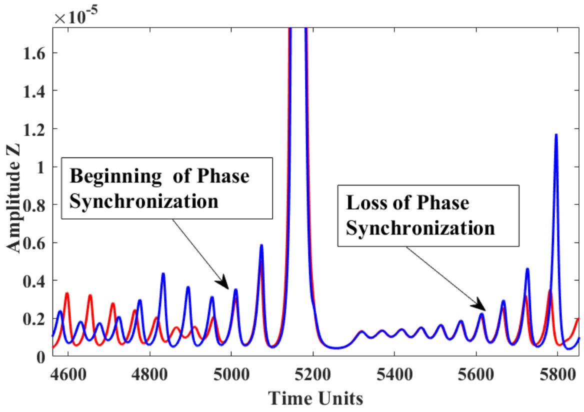

Figure 4.23. Section of a time series showing an in-phase extreme event. We observe the oscillations moving to synchrony before being ejected into a large in-phase event. After the event, the trajectories again perform small amplitude in-phase oscillations, but they soon lose phase sychrony due to a perturbation from the delay at $\tau = 25$.

oscillators lose phase synchrony. This is likely due to a perturbation occurring via the other time delay at $\tau = 25$. This perturbation is sufficient in magnitude to push the trajectory off the manifold. Next, we examine the out-of-phase events in more detail to observe how they are produced. In Fig. 4.24, we can observe two out-of-phase events and the small amplitude oscillations that precede and follow them. At time 24000, the two oscillators are out-of-phase

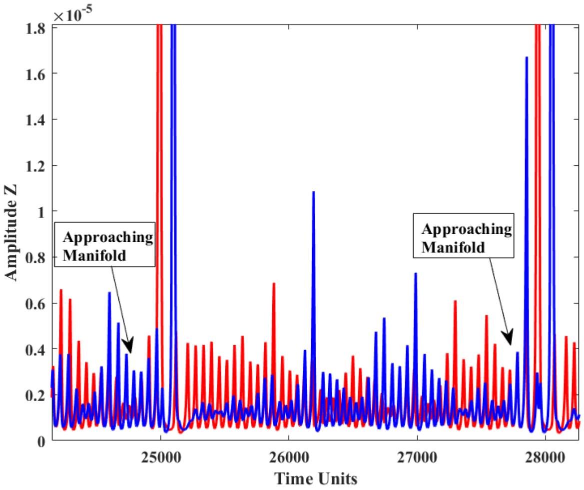

Figure 4.24. Section of a time series showing two out-of-phase extreme events. We can observe the oscillations moving to synchrony just before the large events. In both cases, a perturbation is able to push the trajectories close to the unstable attractor and the oscillators are ejected into a large out-of-phase event. After the large event, the trajectories spiral back toward the stable attractor on the manifold.

with each other. As before in the in-phase example, the trajectory is spiraling toward the limit cycle on the manifold. However, in this case before the trajectory reaches the manifold, a perturbation pushes them off the manifold and sufficiently close to the attractor produced by the delay $\tau = 25$. The oscillators are then ejected into large out-of-phase excursions at time 25000. We can observe this same behavior in the next large oscillation just before time 28000.

The presence of an attractor due to the time delay of 11 on the manifold, and a second attractor created by the second time delay of 25 just off the manifold allows the two delay system to undergo extreme events. All trajectories are attracted to the stable limit cycle on the manifold. If the trajectory can avoid getting to close to the second limit cycle, the trajectory will be ejected into a large in-phase amplitude event. Perturbations caused by the time delay of 25 can cause the oscillators to lose phase synchrony, as the trajectories complete small amplitude oscillations. If the perturbation is of sufficient magnitude, the trajectories can get close enough to the second limit cycle to be ejected in an out-of-phase event.

The findings of this computational study share some similarities to those found in previous studies [11, 12]. Extreme events are found in the instantaneous coupling and two delay system. However, the mechanism for the extreme events using the Oregonator is different [11, 12]. For the single time-delay case, the extreme events are due to the presence of a chaotic mixed-mode attractor. Ansmann et al. discussed the events as a loss of phase sychrony between oscillators. In the double time-delay system, the extreme events are produced by the existence of two limit cycles formed by the two different delays. The interplay between the two perturbations keeps the trajectories from settling on one of the limit cycles. Saha et al. contributed the extreme events in a two delay system to a chaotic saddle. We also did not find extreme events in the single time-delay system as in earlier work [12]; however, only a small section of parameter space was explored.

References

1. S. Albeverio, V. Jentsch, H. Kantz, *Extreme Events in Nature and Society* (Springer, Berlin, 2006).
2. D. Sornette, *Critical Phenomena in Natural Sciences* (Springer, Berlin, 2003).
3. A. Pleshachevsky, S. Lehner, W. Rosenthal, *Ocean Dynam.* **62**, 1335 (2012).
4. C. Kharif, E. Pelinovsky, *Eur. J. Mech. B-Fluid* **22**, 1335 (2003).
5. D. Solli, C. Ropers, P. Koonath, G. Jalali, *Nature* **450**, 1054 (2007).
6. K. Lehnertz, *Extreme Events in Nature and Society* (Springer, Berlin, 2006).
7. I. Dobson, A. Carreras, V. E. Lynch, D. E. Newman, *Chaos* **17**, 2007 (2007).
8. J. A. Feigenbaum, *Quan. Fin.* **1**, 346 (2001).
9. D. Helbing, *Rev. Mod. Phys.* **73**, 1067 (2001).
10. E. Hobsbawm, *The Age of Extremes: 1914-1991* (Abacus, London, 1994).
11. G. Ansmann, R. Karnatask, K. Lehnertz, U. Feudel, *Phys. Rev. E* **88**, 052911 (2013).
12. A. Saha, U. Feudel, *Phys. Rev. E.* **95**, 062219 (2017).
13. A. Saha, U. Feudel, *Chaos* **28**, 033610 (2018).
14. V. Varshney, S. Kumatasamy, A. Mishra, B. Biswal, A. Prasad, *Chaos* **31**, 093136 (2021).
15. R. Fitzhugh, *Biophys. J.* **1**, 445 (1961).
16. J. Nagumo, S. Arimoto, S. Yoshizawa, *Proc. IRE* **50**, 2061 (1962).
17. D. Simpson, R. Kuske, *Physcia D: Nonlinear Phenomena* **240**, 1189 (2011).
18. K. Showalter, R. Noyes, K. Bar-Eli, *J. Chem. Phys.* **67**, 2514 (1978).

19. T. Amemiya, T. Ohmori, T. Yamaguchi, *J. Phys. Chem. A* **104**, 336 (2000).

20. S. Kádár, T. Amemiya, K. Showalter, *J. Phys. Chem. A* **101**, 8200 (1997).